Particle subgrid scale modeling in large-eddy simulation of particle-laden turbulence

PARTICLE SUBGRID SCALE MODELING IN LARGE-EDDY SIMULATION OF PARTICLE-LADEN TURBULENCE

BY

MATTHEW CERNICK, B.Eng.Mgt.

A THESIS

SUBMITTED TO THE DEPARTMENT OF MECHANICAL ENGINEERING

AND THE SCHOOL OF GRADUATE STUDIES

OF MCMASTER UNIVERSITY

IN PARTIAL FULFILMENT OF THE REQUIREMENTS

FOR THE DEGREE OF

MASTER OF APPLIED SCIENCE

Master of Applied Science (2013) McMaster University

(Mechanical Engineering) Hamilton, Ontario, Canada

TITLE:	Particle subgrid scale modeling in large-eddy simulation of particle-laden turbulence
AUTHOR:	Matthew Cernick B.Eng.Mgt., (Mechanical Engineering and Management) McMaster University, Hamilton, Canada
SUPERVISORS:	Dr. S. Tullis Dr. M. Lightstone
NUMBER OF PAGES:	xix, 152

Abstract

This thesis is concerned with particle subgrid scale (SGS) modeling in large-eddy simulation (LES) of particle-laden turbulence. Although most particle-laden LES studies have neglected the effect of the subgrid scales on the particles, several particle SGS models have been proposed in the literature. In this research, the approximate deconvolution method (ADM), and the stochastic models of Fukagata *et al.* (2004), Shotorban and Mashayek (2006) and Berrouk *et al.* (2007) are analyzed. The particle SGS models are assessed by conducting both *a priori* and *a posteriori* tests of a periodic box of decaying, homogeneous and isotropic turbulence with an initial Reynolds number of $\mathrm{Re}_\lambda = 74$. The model results are compared with particle statistics from a direct numerical simulation (DNS). Particles with a large range of Stokes numbers are tested using various filter sizes and stochastic model constant values. Simulations with and without gravity are performed to evaluate the ability of the models to account for the crossing trajectory and continuity effects. The results show that ADM improves results but is only capable of recovering a portion of the SGS turbulent kinetic energy. Conversely, the stochastic models are able to recover sufficient energy, but show a large range of results dependent on Stokes number and filter size. The stochastic models generally perform best at small Stokes numbers. Due to the random component, the stochastic models are unable to predict preferential concentration.

Acknowledgements

First and foremost, I would like to thank my supervisors Dr. Lightstone and Dr. Tullis for their support and guidance throughout my graduate studies. I am also thankful for the financial support of the Natural Sciences and Engineering Research Council of Canada, the Ontario Graduate Scholarship program, and the Queen Elizabeth II Graduate Scholarships in Science and Technology program. Finally, this work was made possible by the computing facilities of the Shared Hierarchical Academic Research Computing Network.

Contents

List of Figures

List of Tables

Nomenclature

English characters

b_i	Csanady correction factor
B_{ij}	anisotropic tensor of fluid motion
C_0	Langevin model constant
C_0^*	modified diffusion term constant
C_ϵ	LES dissipation coefficient
C_D	drag coefficient
C_L	lift coefficient
C_s	Smagorinsky constant
d_p	particle diameter
d_{pc}	fractal dimension
D_p	particle turbulent diffusivity
$E(\kappa)$	turbulent kinetic energy spectrum function
f	ratio of drag coefficient to Stokes drag
F_{sgs}	SGS Brownian force
g	gravitational acceleration
G	filter kernel
G^{-1}	inverse filter kernel
$g(r_i)$	radial distribution function (RDF)
h	computational grid spacing
$\widetilde{k}$	filtered/resolved turbulent kinetic energy
k_f	total fluid turbulent kinetic energy
$\widetilde{k}_{f@p}$	filtered fluid turbulent kinetic energy at the particle's position
k_p	particle turbulent kinetic energy

k_s	turbulent kinetic energy of the fluid seen by the particles
k_{sgs}	SGS turbulent kinetic energy
$\widehat{k}_{sgs}$	modified SGS kinetic energy
$L_{E,f}$	Eulerian fluid integral length scale
L_i	direction cosine
L_{ii}	longitudinal integral length scale
m	Van Cittert series truncation level
m_f	fluid mass
m_p	particle mass
N_p	number of computational particles
p	pressure
P	pressure normalized by the fluid density
$\widetilde{p}^*$	modified filtered pressure
$\widetilde{P}^*$	modified filtered pressure normalized by the fluid density
r_i	particle pair separation distance
R_{Lp}	particle Lagrangian velocity autocorrelation coefficient
R_{Lu_s}	Lagrangian autocorrelation coefficient of seen fluid velocity
Re_p	particle Reynolds number
Re_L	fluid integral length scale Reynolds number
Re_λ	Taylor-scale Reynolds number
S_{ij}	rate of strain tensor
S_u	skewness of the streamwise velocity derivative
St	Stokes number
t	time
t_0	start time at which particle statistics are examined
t^*	time when particles become independent of their initial conditions
$T_{E,f}$	Eulerian fluid integral timescale
$T_{E,sgs}$	Eulerian fluid SGS timescale
$T_{L,sgs}$	Lagrangian fluid SGS timescale
$T^*_{L,sgs}$	SGS fluid Lagrangian timescale along an inertial particle's path
u_d	particle drift velocity

u_f	fluid velocity
u_p	particle velocity
$\left\langle u_{p,rel}^2 \right\rangle$	mean squared relative velocity
u_r	slip velocity between the particle and the fluid
u_s	fluid velocity seen by the particle
V	domain volume
W_i	Wiener process
x_i	direction i
x_p	particle position
$\left\langle x_p^2 \right\rangle$	particle mean square dispersion

Greek characters

β	ratio of the Lagrangian and Eulerian fluid SGS timescales
δ_{ij}	Kronecker delta
Δ	filter width
Δt	timestep
ϵ	total fluid dissipation rate
ϵ_{sgs}	SGS fluid dissipation rate
η_K	Kolmogorov length scale
κ	wavenumber
λ	Taylor microscale
μ	dynamic viscosity
ν	kinematic viscosity
ν_t	turbulent viscosity
ρ_f	fluid density
ρ_p	particle density
τ_{ij}	SGS stress tensor
τ_{ij}^r	anisotropic SGS stress tensor
τ_K	Kolmogorov timescale
$\tau_{L,p}$	particle Lagrangian integral timescale
τ_p	particle relaxation time

ξ	Gaussian random number with zero mean and unit variance

Accents

$\overline{(\,)}$	time averaged variable
$\widetilde{(\,)}$	filtered variable
$\vec{(\,)}$	vector

Brackets

$\langle\,\rangle$	ensemble average

Subscripts

$(\,)_{@p}$	at particle's position
$(\,)_{DNS}$	direct numerical simulation
$(\,)_{FDNS}$	filtered direct numerical simulation
$(\,)_{f}$	fluid phase
$(\,)_{fp}$	fluid particle
$(\,)_{LES}$	large-eddy simulation
$(\,)_{p}$	particle
$(\,)_{sgs}$	subgrid scale component
$(\,)_{\parallel}$	direction of mean drift
$(\,)_{\perp}$	transverse direction

Superscripts

$(\,)'$	turbulent component
$(\,)''$	SGS component

Chapter 1

Introduction

1.1 Background

Particle-laden turbulent flows are encountered in many engineering applications. Some of the most common examples include the delivery of aerosol medications, liquid droplets of fuel in combustion systems, aerosol sprays, and atmospheric flows, such as pollutant dispersion from a chimney. Therefore, engineers and scientists require mathematical models that predict the motion of particulates in turbulent flows.

Modeling of particle-laden turbulent flows first requires calculation of the flow field, followed by the particle phase. Often, the turbulent velocity field is obtained using Reynolds-averaged Navier-Stokes equations (RANS). This is by far the most commonly used methodology in industry due to its relatively low computational expense. In RANS the entire range of turbulent scales are modeled, and thus additional modeling is required to account for the effect of the turbulence on the particles.

Alternatively, direct numerical simulation (DNS) can be used to solve for the turbulent flow field without any modeling. In DNS the governing equations are solved

directly and the entire range of turbulent scales are fully resolved. Consequently, the computational expense is extremely high, and as such DNS is impractical for flows of industrial interest. However, DNS can be a valuable research tool since it yields very accurate results that do not contain any errors due to modeling.

The focus of this thesis is modeling of particle-laden turbulence using large-eddy simulation (LES) to solve for the turbulent velocity field. LES is a compromise between RANS and DNS. In LES, the large turbulent structures are resolved, and only the small turbulent motions, which are named the subgid scales (SGS), are modeled. Compared to RANS, LES with particles would be expected to yield superior results, including the ability to account for the interactions between particles and turbulent structures. Furthermore, due to the lower computational expense, LES can be used to simulate some flows of industrial interest for which DNS is infeasible. For many particle LES simulations, the effect of the small turbulent motions on the particles must be accounted for using particle SGS modeling. In this investigation, several particle SGS models are analyzed and tested using numerical simulations.

1.2 Objective and scope

Several models that account for the influence of the subgrid scales on the particles have been proposed in the literature. However, existing particle SGS models have not been extensively tested. For the most part, particle SGS models have only been tested in a limited capacity by those researchers who developed them, and the models have not been thoroughly compared to one another. The objective of this thesis is to evaluate and compare a few of the particle SGS models that have been proposed in the literature. The models that are examined in this work are the approximate

deconvolution method (ADM), and the stochastic models of Fukagata *et al.* (2004), Shotorban and Mashayek (2006) and Berrouk *et al.* (2007).

The particle SGS models are tested using numerical simulations of particles in a periodic box of decaying, homogeneous and isotropic turbulence. In addition to being compared to one another, the model results are evaluated against DNS particle results, and results of particles tracked in a LES flow field without any particle SGS model. Both *a priori* and *a posteriori* testing methodologies are used. For the *a posteriori* tests particles are tracked in a LES flow field, but the in the *a priori* tests the particles are tracked in a flow field that does not contain any LES fluid modeling errors. Particles with various amounts of inertia are considered with and without gravity, and a range of LES filter sizes and stochastic model constant values are used. Based on the results, conclusions and recommendations are made that will assist in the development of superior particle SGS models in the future.

This research is limited to dilute particle-fluid flows consisting of small spherical particles with densities much greater than that of the fluid.

1.3 Thesis outline

This thesis consists of five chapters. Chapter 2 presents a literature review of turbulence modeling, modeling of the particle phase including important phenomena, and particle SGS modeling. Chapter 3 describes the methodologies used to test the models, calculate the fluid phase, calculate the particle phase, and implement the particle SGS models. The results and discussion of the numerical simulations using the different particle SGS models are given in Chapter 4. Finally, Chapter 5 presents the conclusions from the research, as well as recommendations for future work.

Chapter 2

Background and Literature Review

This chapter presents a background on particle behaviour in turbulence, and modeling of subgrid scale (SGS) effects on particles in a large-eddy simulation (LES). A solution to the fluid field must be obtained before particle trajectories can be calculated. Three approaches to turbulence modeling are reviewed: direct numerical simulation (DNS), Reynolds-averaged Navier-Stokes equations (RANS) and large-eddy simulation (LES). These different methods are characterized by the amount of description they provide, the level of modeling and the relative computational expense. Next, calculation of the particle phase is reviewed, including Taylor's theorem for particle dispersion and important particle phenomena. Lastly, a literature review of particle SGS modeling is presented. Particular attention is paid to models that are examined in this thesis.

2.1 Fluid phase

2.1.1 Governing equations

Fluid motion is governed by conservation equations for mass and momentum (Navier-Stokes equations). For an incompressible fluid with constant viscosity these equations can be expressed as

$$\frac{\partial u_{f,i}}{\partial x_i} = 0 \tag{2.1}$$

$$\frac{\partial u_{f,i}}{\partial t} + u_{f,j}\frac{\partial u_{f,i}}{\partial x_j} = -\frac{1}{\rho_f}\frac{\partial p}{\partial x_i} + \nu\frac{\partial^2 u_{f,i}}{\partial x_j \partial x_j} \tag{2.2}$$

where $u_{f,i}$ is the fluid velocity in the direction x_i, ρ_f is the fluid density and ν is the kinematic viscosity of the fluid.

Numerous methodologies exist to obtain a solution to the Navier-Stokes equations. Direct Numerical Simulation yields an exact instantaneous solution by numerically solving the conservation equations without any modeling. A computationally less expensive method is solving Reynolds-averaged Navier-Stokes equations, which involve modeling all of the turbulence and solving for the time averaged flow field. A compromise between DNS and RANS is large-eddy simulation. In LES the larger turbulent motions are resolved by solving for the instantaneous volume averaged velocity field, and only the smaller turbulent structures are modeled.

2.1.2 Direct numerical simulation (DNS)

Direct numerical simulation consists of solving equations (2.1) and (2.2) by discretizing and numerically solving for the time dependent velocity and pressure fields for given initial and boundary conditions. This method provides a complete solution to

the Navier-Stokes equations without any modeling which makes it the most accurate method. However, the computational cost of DNS is extremely high since all turbulent scales must be resolved. In order to resolve the smallest scales of the flow (Kolmogorov scales) the grid spacing and time step must be sufficiently small. As the Reynolds number increases the Kolmogorov scales become smaller which substantially increases the required number of nodes. The computational cost of a DNS is proportional to Re_L^3 (Pope, 2000), where Re_L is the Reynolds number based on the integral length scale. Therefore, DNS is limited to low Reynolds number flows of simple geometry, and cannot generally be used to simulate flows of practical interest.

2.1.3 Reynolds-averaged Navier-Stokes equations (RANS)

The most common approach to turbulence modeling is to average the Navier-Stokes equations over time. Reynolds-averaging consists of decomposing the velocity and pressure into mean and fluctuating components:

$$u_{f,i} = \overline{u_{f,i}} + u'_{f,i} \tag{2.3}$$

$$p = \overline{p} + p' \tag{2.4}$$

Substituting these relationships into the Navier-Stokes equations and time-averaging each term yields the Reynolds-averaged Navier-Stokes equations:

$$\frac{\partial \overline{u_{f,i}}}{\partial x_i} = 0 \tag{2.5}$$

$$\frac{\partial \overline{u_{f,i}}}{\partial t} + \overline{u_{f,j}} \frac{\partial \overline{u_{f,i}}}{\partial x_j} = -\frac{1}{\rho_f} \frac{\partial \overline{p}}{\partial x_i} + \nu \frac{\partial^2 \overline{u_{f,i}}}{\partial x_j \partial x_j} - \frac{\partial \overline{u'_{f,i} u'_{f,j}}}{\partial x_j} \tag{2.6}$$

The RANS and Navier-Stokes equations differ due to the addition of the Reynolds stress term $\overline{u'_{f,i}u'_{f,j}}$. This additional term leads to a closure problem and therefore the Reynolds stresses must be modeled. The classic approach to modeling the Reynolds stresses is to relate them to the mean strain using a turbulent eddy viscosity. Compared to other approaches, RANS simulations have relatively low computational cost which allows for industrial flows with high Reynolds numbers and complex geometries to be simulated.

2.1.4 Large-eddy simulation (LES)

In large-eddy simulation the Navier-Stokes equations are averaged in space by decomposing the velocity into filtered (spatially averaged) and residual components:

$$u_{f,i} = \widetilde{u_{f,i}} + u''_{f,i} \tag{2.7}$$

where the tilde represents a filtered variable, and u''_f is the subgrid scale (SGS) fluid velocity which is associated with the residual field. The filtered Navier-Stokes equations are obtained by substituting (2.7) into the conservation equations (2.1) and (2.2), and applying the filtering operation to each term.

$$\frac{\partial \widetilde{u_{f,i}}}{\partial x_i} = 0 \tag{2.8}$$

$$\frac{\partial \widetilde{u_{f,i}}}{\partial t} + \widetilde{u_{f,j}}\frac{\partial \widetilde{u_{f,i}}}{\partial x_j} = -\frac{1}{\rho_f}\frac{\partial \widetilde{p}}{\partial x_i} + \nu\frac{\partial^2 \widetilde{u_{f,i}}}{\partial x_j \partial x_j} - \frac{\partial \tau_{ij}}{\partial x_i} \tag{2.9}$$

τ_{ij} is the subgrid stress tensor and represents the effects of the unresolved scales.

$$\tau_{ij} = \widetilde{u_{f,i}u_{f,j}} - \widetilde{u_{f,i}}\widetilde{u_{f,j}} \tag{2.10}$$

To close the equations the SGS stress term must be modeled. The Smagorinsky model (Smagorinsky, 1963) is one of the simplest and most commonly used fluid SGS models. It uses an eddy viscosity assumption to model the anisotropic SGS stress tensor τ_{ij}^r.

$$\tau_{ij} = \tau_{ij}^r + \frac{2}{3}k_{sgs}\delta_{ij} \tag{2.11}$$

$$\tau_{ij}^r = -2\nu_t\widetilde{S_{ij}} \tag{2.12}$$

k_{sgs} is the fluid SGS turbulent kinetic energy, ν_t is the turbulent or eddy viscosity and $\widetilde{S_{ij}}$ is the filtered rate of strain tensor. The SGS turbulent kinetic energy is included in the pressure term using a modified filtered pressure $\widetilde{p}^*$:

$$\widetilde{p}^* = \widetilde{p} + \frac{2}{3}\rho_f k_{sgs} \tag{2.13}$$

The filtered pressure ($\widetilde{p}$) in equation (2.9) is replaced by the modified filtered pressure ($\widetilde{p}^*$). A mixing length assumption is used to model the turbulent viscosity as

$$\nu_t = (C_s\Delta)^2|\widetilde{S}| \tag{2.14}$$

where C_s is the Smagorinsky constant and Δ is the filter size. In the standard Smagorinsky model the constant is usually taken to be 0.17 (Pope, 2000) based on isotropic turbulence in the inertial subrange. The dynamic version of the model proposed by Germano *et al.* (1991) improves upon the standard Smagorinsky model

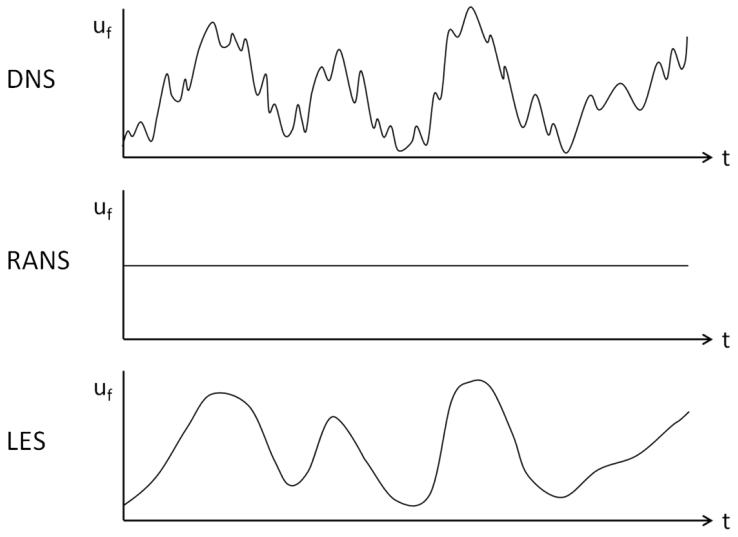

Figure 2.1: Example of a fluid velocity time trace at a point in space in DNS, RANS and LES simulations.

by dynamically calculating the local constant based on the smallest resolved scales.

LES lies between DNS and RANS in terms of the level of description, amount of modeling and computational cost. The differences between the three methodologies are well demonstrated in Figure 2.1. The time trace from the DNS shows all turbulent velocity fluctuations since the entire flow field is resolved. In RANS only the time averaged velocity is determined and all of the scales of turbulence are modeled. Consequently, the time trace is equal to the mean velocity and does not change in time. The LES time trace looks like a smoothed version of the DNS. In LES the large turbulent structures are explicitly represented so the low frequency fluctuations are still present in the time trace. However, the high frequency fluctuations have been removed since the small scale structures are modeled.

The motivation for LES is that in DNS almost all of the computational effort arises from the resolution of the smallest scales. However, it is the large scales that

contain the majority of the turbulent kinetic energy and are generally of more interest than then the small scales. The large scales are responsible for motion, are affected by geometry and can be anisotropic. In contrast, the small scales are more universal, contain little energy and are only important for viscous dissipation. The small scales are also better suited to modeling since assumptions of isotropy are more valid for the small scale motions than they are for large turbulent structures.

2.2 Particle phase

2.2.1 Particle equation of motion

The trajectory of an individual spherical particle is governed by the particle equation of motion (Maxey and Riley, 1983):

$$\begin{aligned} m_p \frac{du_{p,i}}{dt} =& \frac{1}{8}\pi C_D \rho_f d_p^2 |\vec{u_f} - \vec{u_p}|(u_{f,i} - u_{p,i}) + m_p g_i - m_f g_i \\ &+ m_f \frac{Du_{f,i}}{Dt} + \frac{1}{2} m_f (\frac{Du_{f,i}}{Dt} - \frac{du_{p,i}}{dt}) \\ &+ \frac{3}{2} d_p^2 \sqrt{\pi \rho_f \mu} \int_0^t \frac{\frac{d}{dt}(u_{f,i} - u_{p,i})}{\sqrt{t - t'}} dt' + \frac{3}{4} m_f C_L L_i |\vec{u_f} - \vec{u_p}|^2 \end{aligned} \tag{2.15}$$

where u_p is the particle velocity, m is the mass, C_D is the drag coefficient, d_p is the particle diameter, g_i is gravitational acceleration, μ is the dynamic viscosity, C_L is the lift coefficient and L_i is the direction cosine. The forces on the right hand side of (2.15), from left to right, are the drag, gravity, buoyancy, fluid acceleration, virtual mass, Basset and Saffman lift forces.

Dividing (2.15) by m_p reveals that some of the forces can be neglected when the particle density is much greater than that of the fluid ($\rho_p >> \rho_f$). In this case only the

drag and gravity forces are important since the term ρ_p/ρ_f appears in the denominator of all other forces. Numerical experiments have confirmed that these other forces are negligible when the density ratio is very large, such as $\rho_p/\rho_f \sim O(1000)$ (Elghobashi and Truesdell, 1992) (Armenio and Fiorotto, 2001). For very large density ratios the particle equation of motion simplifies to

$$\frac{du_{p,i}}{dt} = \frac{3}{4}\frac{\rho_f}{\rho_p}\frac{1}{d_p}C_D|\vec{u_f} - \vec{u_p}|(u_{f,i} - u_{p,i}) + g_i \tag{2.16}$$

For small particles, the particle Reynolds numbers remains sufficiently low such that the drag coefficient can be expressed as Stokes drag with a modification factor f (Clift *et al.*, 1978).

$$C_D = \frac{24}{\mathrm{Re}_p} f \tag{2.17}$$

where the modification factor is

$$f = 1 + 0.15\mathrm{Re}_p^{0.687} \quad \text{for} \quad \mathrm{Re}_p < 800 \tag{2.18}$$

and the particle Reynolds number is defined as

$$\mathrm{Re}_p = \frac{d_p|\vec{u_f} - \vec{u_p}|}{\nu} \tag{2.19}$$

Substitution of these relationships into (2.16) and simplifying gives

$$\frac{du_{p,i}}{dt} = \frac{f}{\tau_p}(u_{f,i} - u_{p,i}) + g_i \tag{2.20}$$

where τ_p is the particle relaxation time and is defined as

$$\tau_p = \frac{\rho_p}{\rho_f} \frac{d_p^2}{18\nu} \tag{2.21}$$

The particle relaxation time is a measure of how long a particle takes to adjust to a change in the fluid velocity.

2.2.2 Taylor's theorem

The mathematical basis of particle dispersion in turbulent flow is well described by the classic work of Taylor (1921). Taylor considered the dispersion of fluid particles in statistically stationary, homogeneous turbulence released from a point source. Figure 2.2 illustrates the trajectory of a single particle released at $t = 0$ in a turbulent flow, and its position at some later time $t = t'$. The final result of Taylor's work is

$$\frac{d\langle x_{fp}^2 \rangle}{dt} = 2\langle u_f'^2 \rangle \int_0^t R_{L,fp}(\tau) d\tau \tag{2.22}$$

where $\langle\ \rangle$ brackets denote an ensemble average over all particles and x_{fp} is the position of a fluid particle. $R_{L,fp}(\tau)$ is the fluid particle Lagrangian velocity autocorrelation coefficient and for stationary turbulence is defined as

$$R_{L,fp}(\tau) = \frac{\langle u_f'(t) u_f'(t+\tau) \rangle}{\langle u_f'^2 \rangle} \tag{2.23}$$

Considering the asymptotes of Taylor's final result can provide insight into particle dispersion. For very short times the autocorrelation coefficient is unity and (2.22)

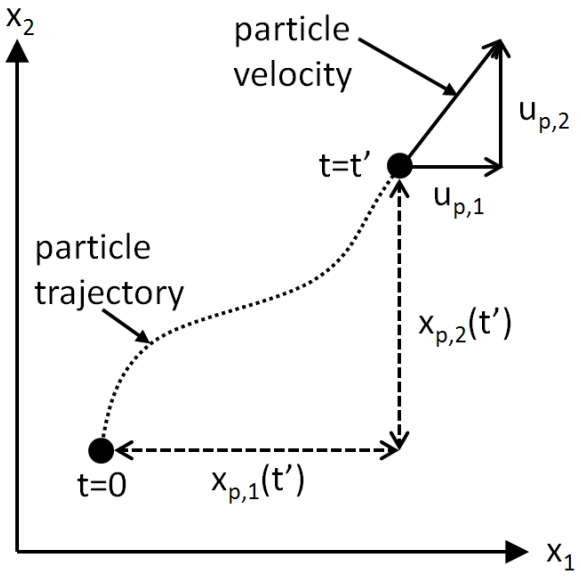

Figure 2.2: Coordinate system for the dispersion of a particle in a turbulent flow. The particle is shown at its initial time $t = 0$, and at some later time t'.

becomes

$$\frac{d\langle x_{fp}^2 \rangle}{dt} = 2\langle u_f'^2 \rangle t \quad \text{for very short times} \tag{2.24}$$

and the dispersion is

$$\langle x_{fp}^2 \rangle = \langle u_f'^2 \rangle t^2 \quad \text{for very short times} \tag{2.25}$$

The long time behaviour is found by integrating the autocorrelation coefficient to obtain the fluid particle Lagrangian integral timescale

$$\tau_{L,fp} = \int_0^\infty R_{L,fp}(\tau) d\tau \tag{2.26}$$

Using this relationship, Taylor's result for very long times becomes

$$\frac{d\langle x_{fp}^2 \rangle}{dt} = 2\langle u'^2_f \rangle \tau_{L,fp} \quad \text{for very long times} \tag{2.27}$$

$$\langle x_{fp}^2 \rangle = 2\langle u'^2_f \rangle \tau_{L,fp} t \quad \text{for very long times} \tag{2.28}$$

Taylor's work shows that at short times particle dispersion has a parabolic relationship with time, and for long times particle dispersion increases linearly with time. It is also important to note which properties of the turbulence and particles affect dispersion. At short times dispersion is only influenced by the turbulent kinetic energy of the fluid particles. At long times dispersion is determined by both the fluid particle turbulent kinetic energy and Lagrangian integral timescale.

The results of Taylor's work can be extended to real particles by making use of real particle Lagrangian velocity autocorrelation coefficients and statistically stationary particle velocities.

$$\frac{d\langle x_p^2 \rangle}{dt} = 2\langle u'^2_p \rangle \int_0^t R_{Lp}(\tau) d\tau \tag{2.29}$$

Based on this result, all conclusions from Taylor's work for fluid particles are also valid for inertial particles. Therefore, at long times the dispersion of real particles is determined by both the particle turbulent kinetic energy and the particle velocity Lagrangian integral timescale.

2.2.3 Particle phenomena

The trajectories of real particles differ from fluid particles. This deviation in particle paths leads to several important effects that inertial particles experience. Particle phenomena that are relevant to the current work are discussed in this section.

Inertia effect

High inertia particles have smaller velocity fluctuations and are unable to follow all of the high frequency turbulent velocity fluctuations of the surrounding fluid (Shirolkar *et al.*, 1996). This is well demonstrated by the particle relaxation time (defined in equation 2.21), which characterizes the size and inertia of a particle. A small particle with little inertia is able to respond very quickly to the fluid and behaves similar to a tracer particle. In contrast, if a particle is large and heavy it will take a significant amount of time to respond to changes in the fluid, and will be unable to follow the high frequency fluid velocity fluctuations.

Since inertial particles take time to respond to the fluid, an inertial particle is correlated to its initial velocity for a longer length of time. A particle with very small inertia will have a Lagrangian timescale approximately equal to the Lagrangian integral timescale of the fluid. Conversely, the Lagrangian timescale of a particle with very high inertia will be similar to the fluid Eulerian integral timescale (Berrouk *et al.*, 2007).

Taylor's work (Section 2.2.2) shows that dispersion depends on particle velocity fluctuations and the particle Lagrangian integral timescale. Inertia decreases particle velocity fluctuations but increases a particle's Lagrangian timescale. Therefore, it is not clear if inertia increases or decreases particle dispersion.

Crossing trajectory effect

The crossing trajectory effect (CTE) is a reduction in dispersion due to particles migrating out of eddies before they decay (Csanady, 1963). Unlike a fluid particle, a real particle may or may not remain in a turbulent eddy for the eddy's entire lifetime.

The primary reason that a particle prematurely leaves an eddy is its drift velocity due to gravity, which can cause it to transverse the eddy before it dies. Fluid velocities in a turbulent eddy are highly correlated. Thus, when a particle leaves on eddy it is exposed to fluid velocities that are less correlated to the previous fluid velocities. As a result, the particle Lagrangian integral timescale is reduced. This reduction in particle Lagrangian timescale causes a decrease in dispersion.

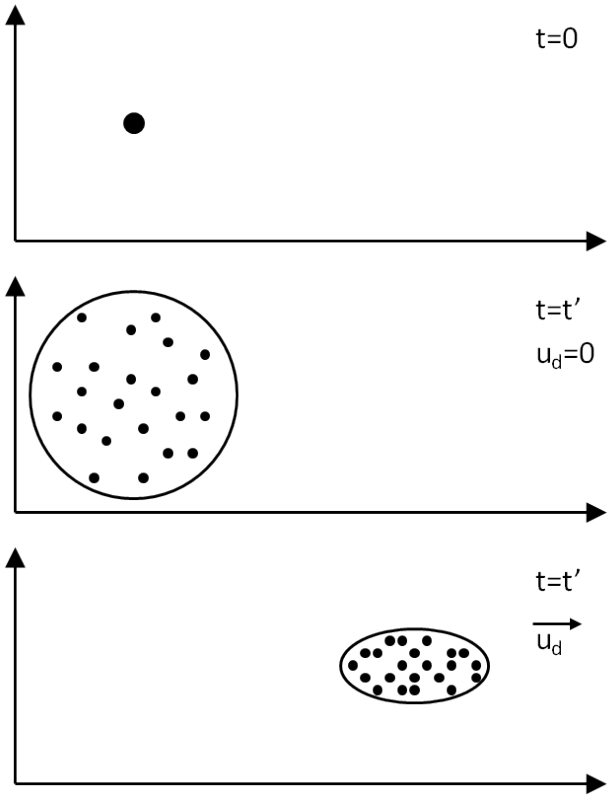

Figure 2.3: Illustration of a cloud of particles initially released from a point source in a turbulent flow. Dispersion is reduced when a mean drift velocity exists due to the crossing trajectory and continuity effects. The contintuiy effect causes dispersion to be further reduced in the transverse directions.

Continuity effect

The continuity effect causes dispersion to be reduced in the transverse directions (directions perpendicular to the mean drift) (Csanady, 1963). The continuity effect is a result of the CTE, but it is a distinct phenomenon. When a particle falls out of an eddy, due to the CTE, it enters the eddy's back flow in order to satisfy continuity. As a result, the correlation coefficients of the fluid velocity seen by the particles in the transverse directions contain negative loops. In the asymptotic case of very high drift velocity, the work of Csanady (1963) shows that particle dispersion in the mean drift direction should be twice that of the two transverse directions ($(D_p)_{\parallel} \sim 2(D_p)_{\perp}$). The influence of the crossing trajectory and continuity effects is demonstrated in Figure 2.3 and Figure 2.4.

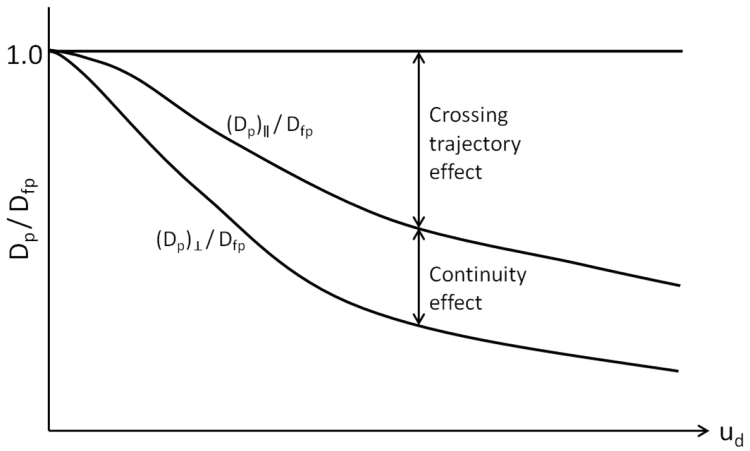

Figure 2.4: Dispersion in the mean drift and transverse directions, normalized by fluid particle dispersion, as a function of mean drift velocity. Dispersion is reduced due to crossing trajectory and continuity effects. Reproduced from Csanady (1963).

Preferential concentration

Intermediate sized particles accumulate in certain regions of a turbulent flow field due to coherent structures. This phenomenon is called preferential concentration (Eaton and Fessler, 1994). Preferential concentration is most significant for Stokes numbers of approximately unity. The Stokes number is defined as the ratio of the particle response time to a characteristic fluid timescale.

$$\mathrm{St} = \frac{\tau_p}{\tau_f} \tag{2.30}$$

The Kolmogorov timescale is commonly used as the fluid timescale in (2.30) for simple turbulent flows. In homogeneous isotropic turbulence, particles with either very small or very high inertia tend to have particle distributions with uniform probability density functions (equally likely at all points in space). This is because very small inertia particles behave like tracer particles, and very high inertia particles easily travel through turbulent structures due to their inertia. However, coherent structures cause intermediate sized to have some organized motions. Particles with Stokes numbers of approximately unity are flung out of high vorticity structures, which causes them to accumulate in regions of low vorticity and high strain. A non-uniform particle distribution resulting from preferential concentration is shown in Figure 2.5(b). In Figure 2.5(a) the fluid particles have a uniformly random distribution throughout the entire domain. However, in Figure 2.5(b) the particles are highly concentrated in turbulent structures with low vorticity and high strain, and high vorticity structures contain very few particles.

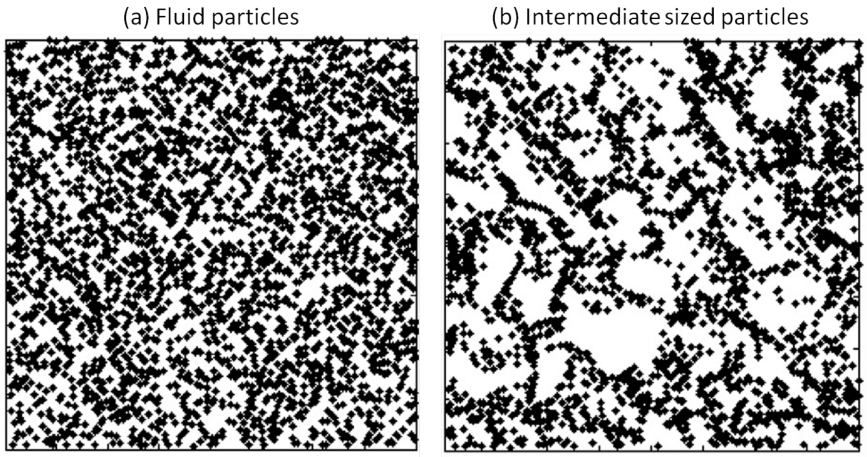

Figure 2.5: Snapshot of the particle field from a particle-laden DNS with (a) fluid particles and (b) intermediate sized particles (Strutt *et al.*, 2011).

2.2.4 Particle-laden turbulence modeling

Modeling particle-laden turbulence requires solutions to both the fluid field and the particulate phase. The fluid phase is generally treated in an Eulerian frame of reference and a solution is obtained using one of the methods reviewed in Section 2.1. To solve for the particle phase either a Langrangian or Eulerian frame of reference may be used.

Eulerian models are the simplest approach to particle-laden turbulence modeling. In this approach, the particle phase is treated as a continuum and a set of conservation equations are used to solve for particle concentrations and velocities. The simplest Eulerian particle dispersion model is the locally homogeneous flow model. This model assumes that the particles have the same velocity as the fluid, which results is a pseudo single phase (Shirolkar *et al.*, 1996). A more advanced Eulerian approach is the two-fluid model. The two-fluid model treats the particles as a distinct phase that is mixed into the fluid phase. The difficulty with this approach is that the effective particle

turbulent diffusivity must be modeled (Shirolkar *et al.*, 1996).

Lagrangian particle models track a large number of individual particles in a Lagrangian reference frame. Lagrangian dispersion models have the potential to account for non-continuum and particle history effects that cannot be accounted for with Eulerian methods. Individual particle trajectories are determined by solving the particle equation of motion. Depending on the method used to solve for the fluid field, further modeling may be required.

In particle-laden DNS the complete turbulent flow field is available, and as a result no modeling is required to solve the particle equation of motion.

RANS turbulence models provide only the time-averaged flow field, but it is the instantaneous turbulent velocity that is required to evaluate the particle equation of motion. Therefore, Lagrangian particles coupled with RANS solvers require additional modeling to account for the turbulence. The most common approach is to use a stochastic model to modify the fluid velocity based on the local turbulent kinetic energy (Shirolkar *et al.*, 1996). The fluctuating velocity is commonly assumed to be constant during the time that a particle interacts with a turbulent eddy. The eddy lifetime is usually estimated using the turbulent kinetic energy and dissipation rate from the RANS turbulence model. RANS particle models do not fully capture the physics of particle-laden turbulence. Some RANS models do account for the CTE, but many particle effects cannot be accounted for. It is particularity difficult to capture the effects of turbulent structures on particles since in RANS all turbulent scales are modeled. For instance, RANS particle models are unable to account for the effects that coherent structures have on particle distributions.

The focus of this thesis is Lagrangian particle tracking with LES. Particle-laden

LES has the potential to overcome some of the problems associated with particle-laden RANS, and have significantly less computational expense than particle-laden DNS. In LES the larger turbulent motions are solved for but the smaller turbulent scales are modeled. In order to simulate particle-laden turbulence using LES the effect of the SGS fluid motions on the particles may have to be accounted for. A literature review of SGS particle modeling is given in Section 2.3.

2.3 Particle subgrid scale modeling

LES is a promising tool for simulation of particle-laden turbulence. LES can be used to simulate particle-laden flows of industrial interest with high Reynolds numbers and complex geometries for which DNS is impractical. LES can also provide superior accuracy with more description than RANS simulations. Additionally, LES can explicitly capture the interactions between particles and turbulent structures. RANS is incapable of this since it does not resolve any of the turbulence.

Yeh and Lei were the first, to the author's knowledge, to investigate particle-laden turbulence using LES. They performed LES particle simulations in homogeneous isotropic turbulence (Yeh and Lei, 1991a), and in homogeneous turbulent shear flow (Yeh and Lei, 1991b). They assumed that the effect of the SGS fluid field on the particles was negligible, and therefore solved the particle equation of motion using the filtered fluid velocities provided by LES. This has been the standard practice for the majority of particle-laden LES studies.

Depending on the particle properties and LES resolution, the effect of the SGS fluid on the particles may be significant. This was studied by Armenio *et al.* (1999) who performed DNS and LES of particle-laden channel flow and determined that

neglecting SGS effects can lead to inaccurate particle statistics. The authors found that the SGS effects on particles are most significant when the particle relaxation time is small and the LES resolution is coarse (a large filter size). Furthermore, it was shown that particle statistics could be considerably affected by the fluid LES model.

Particle SGS models account for the effect of the SGS fluid field on the particles through modeling. Several different particle SGS models have been proposed, many of which are based on applying RANS particle modeling concepts to LES. One of the earliest and simplest is the model of Wang and Squires (1996). Wang and Squires proposed to calculate the SGS fluid velocity based on the local SGS kinetic energy:

$$u''_{f,i} = \sqrt{\frac{2}{3}k_{sgs}}\xi \tag{2.31}$$

where ξ is a Gaussian random number with zero mean and unit variance. The modeled SGS fluid velocity is added to the filtered velocity provided by the LES.

$$u_{s,i} = \widetilde{u_{f,i}} + u''_{f,i} \tag{2.32}$$

u_s is the fluid velocity seen by the particle and is used in the particle equation of motion to calculate the particle's velocity. The authors did not explicitly state how frequntly $u''_{f,i}$ was sampled, but it was likely every timestep. The results of the author's tests using turbulent channel flow showed that the model had minimal influence on particle statistics.

There are two main types of particle SGS models. The first type is the approximate deconvolution method (ADM) which attempts to apply an inverse filter to obtain

the correct fluid velocity. Alternatively, stochastic models make use of a random component to model the effect of the residual fluid field. The model of Wang and Squires (1996) is an example of a stochastic particle SGS model. In the current work the stochastic particle SGS models of Fukagata *et al.* (2004), Shotorban and Mashayek (2006) and Berrouk *et al.* (2007), and the approximate deconvolution method are tested and compared.

2.3.1 Approximate deconvolution method (ADM)

The approximate deconvolution method (ADM) has been used in several previous studies to model the effect of SGS motions on particles (Kuerten and Vreman, 2005) (Shotorban and Mashayek, 2005) (Kuerten, 2006) (Shotorban *et al.*, 2007). Background on the theory of ADM and a simple one-dimensional example can be found in Appendix A. ADM is a deterministic approach that tries to reconstruct the instantaneous velocities from the filtered field using an inverse filter:

$$u_{s,i} = G^{-1} * \widetilde{u_{f,i}} \tag{2.33}$$

where G is the filter kernel. This reconstructed velocity is then used in the particle equation of motion to track particles. Typically, the inverse filter is approximated with a truncated Van Cittert series expansion:

$$u_{s,i} = \sum_{\alpha=0}^{m} (1 - G)^{\alpha} * \widetilde{u_{f,i}} \tag{2.34}$$

This formula can be evaluated by consecutively applying the filter:

$$u_{s,i} = \widetilde{u_{f,i}} + (\widetilde{u_{f,i}} - \widetilde{\widetilde{u_{f,i}}}) + (\widetilde{u_{f,i}} - 2\widetilde{\widetilde{u_{f,i}}} + \widetilde{\widetilde{\widetilde{u_{f,i}}}}) + ... \tag{2.35}$$

Using (2.35) the reconstructed velocity can be obtained by explicitly filtering the LES field.

Previous studies have shown that ADM often improves particle results compared to LES with no particle SGS model. However, there are some disadvantages of the ADM approach. ADM is never capable of recovering the true instantaneous velocities since the filtered velocities are solved for on an LES grid. ADM is only able to enhance scales that are near the cut-off and are larger than the LES grid. It cannot reconstruct scales that are smaller than the grid, and therefore ADM can only recover a portion of the SGS kinetic energy. As a result, ADM is probably best suited to fine LES and may not be appropriate for coarse LES. Another problem with ADM is the type of filter that is used for the inverse filtering operation. In LES the filter is implicit, so any filter type that is selected for the inverse filtering operation will have no relation to the LES filter. To perform a true deconvolution the original filter and inverse filter must be the same.

2.3.2 Model of Fukagata *et al.* (2004)

The stochastic particle SGS model of Fukagata *et al.* (2004) accounts for the influence of the SGS with a "SGS Brownian" force. This "SGS Brownian" force is added to

the right hand side of the particle equation of motion.

$$\frac{du_{p,i}}{dt} = \frac{F_{sgs,i}}{m_p} + \Big\{\text{Standard Particle Forces}\Big\} \tag{2.36}$$

The standard forces in the particle equation of motion are evaluated using the filtered fluid field velocities. The SGS force is modeled similarly to Brownian motion:

$$\frac{F_{sgs,i}}{m_p} = \frac{\sigma_s}{\Delta t}\xi_i \tag{2.37}$$

where σ_s is the increase in standard deviation of particle velocity due to SGS velocity fluctuations during the simulation timestep Δt, and ξ is a Gaussian random number with zero mean and unit variance. The quantity σ_s is modeled using the kinetic theory for particle motion in isotropic turbulence (Reeks, 1991).

$$\sigma_s = \sqrt{\frac{2}{3}k_{sgs}\lambda} \tag{2.38}$$

where the parameter λ is defined as

$$\lambda = \left(\frac{1}{1+\theta}\right)\Big[1-\exp(-\alpha(1+\theta))\Big] - \left(\frac{1}{1-\theta}\right)\exp(-2\alpha)\Big[1-\exp(\alpha(1-\theta))\Big] \tag{2.39}$$

and the parameters α and θ are defined as

$$\alpha = \frac{\Delta t}{\tau_p} \quad \text{and} \quad \theta = \frac{\tau_p}{T^*_{L,sgs}} \tag{2.40}$$

Further modeling is required to evaluate the SGS turbulent kinetic energy, and the SGS fluid Lagrangian integral timescale along an inertial particle's path ($T^*_{L,sgs}$).

Fukagata *et al.* tested their model with LES of turbulent channel flow. They examined particle deposition rates and the magnitude of different forces in the viscous sublayer and logarithmic region. They had minimal conclusions regarding their particle SGS model.

2.3.3 Model of Shotorban and Mashayek (2006)

Shotorban and Mashayek (2006) developed a stochastic particle SGS model by starting with the Navier-Stokes equations for the acceleration of a fluid particle, broken up into filtered and SGS components.

$$\frac{Du_{f,i}}{Dt} = \left[-\frac{\partial \widetilde{P}}{\partial x_i} + \nu \frac{\partial^2 \widetilde{u_{f,i}}}{\partial x_j \partial x_j} \right] + \left[-\frac{\partial P''}{\partial x_i} + \nu \frac{\partial^2 u''_{f,i}}{\partial x_j \partial x_j} \right] \tag{2.41}$$

where P is the pressure normalized by the fluid density:

$$P = \frac{p}{\rho_f} \tag{2.42}$$

The first two terms on the right hand side of (2.41) can be calculated from the LES field, but the last two terms must be modeled. Shotorban and Mashayek modeled these terms using a Langevin equation. The generalized Langevin equation originally developed by Pope (1994) has been used extensively for particle-laden RANS simulations (Minier and Peirano, 2001). Shotorban and Mashayek extended the RANS concepts to modeling of particle-laden LES. The Langevin equation that they used for the fluid velocity seen by the particles is:

$$du_{s,i} = \left[-\frac{\partial \widetilde{P}}{\partial x_i} + \nu \frac{\partial^2 \widetilde{u_{f,i}}}{\partial x_j \partial x_j} - \frac{(u_{s,i} - \widetilde{u_{f,i}})}{T^*_{L,sgs}} \right] dt + \sqrt{C_0 \epsilon_{sgs}} dW_i \tag{2.43}$$

where C_0 is a model constant, ϵ_{sgs} is the SGS fluid dissipation rate and W_i denotes a Wiener process.

The timescale and SGS dissipation are modeled using relationships given by Gicquel *et al.* (2002) and Heinz (2003):

$$T^*_{L,sgs} = \left(\frac{1}{2} + \frac{3}{4}C_0\right)^{-1} \frac{k_{sgs}}{\epsilon_{sgs}} \tag{2.44}$$

$$\epsilon_{sgs} = C_\epsilon \frac{(k_{sgs})^{3/2}}{\Delta} \tag{2.45}$$

where C_ϵ is a model constant. Equation (2.44) is based on the assumption the SGS fluid Lagrangian integral timescale along an inertial particle's path is equal to that of a fluid particle. The SGS kinetic energy must be modeled to close the equations.

The authors tested their model using decaying isotropic turbulence in a box. They found that the model performed best for small time constant particles. For large particles the model added too much turbulent kinetic energy, and particle dispersion was overpredicted.

2.3.4 Model of Berrouk *et al.* (2007)

The model of Berrouk *et al.* (2007) is similar to the model of Shotorban and Mashayek (2006), but includes additional complexities to account for particle inertia, the crossing trajectory effect, the continuity effect, fluid anisotropy and non-stationary turbulence. The Langevin equation that they used has a direction specific timescale and a

modified diffusion term constant:

$$du_{s,i} = \left[-\frac{\partial \widetilde{P}}{\partial x_i} + \nu \frac{\partial^2 \widetilde{u_{f,i}}}{\partial x_j \partial x_j} - \frac{(u_{s,i} - \widetilde{u_{f,i}})}{T_i^*} \right] dt + \sqrt{C_0^* \epsilon_{sgs}} dW_i \tag{2.46}$$

The diffusion term is closed by specifying the direction specific SGS fluid Lagrangian integral timescale along an inertial particle's path. To begin, the fluid particle timescale is calculated using the same method as Shotorban and Mashayek (2006):

$$T_{L,sgs} = \left(\frac{1}{2} + \frac{3}{4} C_0 \right)^{-1} \frac{k_{sgs}}{\epsilon_{sgs}} \tag{2.47}$$

A correlation developed by Wang and Stock (1993) is used to account for particle inertia:

$$T_{L,sgs}^* = \frac{T_{L,sgs}}{\beta} \left[1 - (1 - \beta)(1 + \mathrm{St}_{E,sgs})^{-0.4(1+0.01\mathrm{St}_{E,sgs})} \right] \tag{2.48}$$

$\mathrm{St}_{E,sgs}$ is the Stokes number based on the Eulerian SGS timescale, and β is the ratio of the Lagrangian and Eulerian fluid SGS timescales.

$$\beta = \frac{T_{L,sgs}}{T_{E,sgs}} \tag{2.49}$$

The correlation in (2.48) was developed for the large turbulent scales using a numerical simulation that generated turbulence using Fourier modes. Berrouk *et al.* chose to apply (2.48) to the subgrid scales. They also assumed that β does not vary across different scales of turbulence and used a constant value of 0.356 based on the numerical work of Wang and Stock (1993). However, the authors state that it has been shown that β is a function of Reynolds number and that a large range of values have been reported in the literature. Equation (2.48) has the correct asymptotic behaviour that

for very small inertia particles $T^*_{L,sgs} \rightarrow T_{L,sgs}$, and for very high inertia particles $T^*_{L,sgs} \rightarrow T_{E,sgs}$.

The particle Lagrangian SGS timescales in the direction of mean drift ($\parallel$) and transverse directions ($\perp$) are calculated using the correction factors proposed by Csanady (1963):

$$T^*_i = \frac{T^*_{L,sgs}}{b_i} \tag{2.50}$$

$$b_i = \begin{cases} b_\parallel = \sqrt{1 + \beta^2 \frac{|\langle u_r \rangle|^2}{(2/3)\langle k_{sgs} \rangle}} \\ b_\perp = \sqrt{1 + 4\beta^2 \frac{|\langle u_r \rangle|^2}{(2/3)\langle k_{sgs} \rangle}} \end{cases} \tag{2.51}$$

where $\langle u_r \rangle$ is the mean slip velocity between the particles and the fluid. Csanady's factors are used to account for the crossing trajectory and continuity effects.

Closure of the diffusion term is accomplished by modeling the SGS dissipation rate and the modified model constant C^*_0. The modified model constant is modeled by extending RANS particle Langevin equation concepts to LES (Minier and Peirano, 2001). It accounts for fluid anisotropy and non-stationary turbulence.

$$C^*_0 = C_0 b_i \frac{\widehat{k}_{sgs}}{k_{sgs}} + \frac{2}{3}\left(b_i \frac{\widehat{k}_{sgs}}{k_{sgs}} - 1 \right) \tag{2.52}$$

where $\widehat{k}_{sgs}$ is a modified SGS kinetic energy which is weighted by the Csanady factors to account for anisotropy.

For certain cases the models of Shotorban and Mashayek (2006) and Berrouk *et al.* (2007) have minimal or no differences between them. For instance, the two models are identical for fluid particles in isotropic turbulence. In the case of inertial particles with zero mean drift, such as the case of no gravity, the only difference between the

two models is the particle inertia correction in equation (2.48).

The authors tested their model using turbulent pipe flow (Berrouk *et al.*, 2007) (Berrouk *et al.*, 2008) and turbulent flow around a 90 degree bend (Berrouk and Laurence, 2008). Concentration profiles and particle deposition statistics for small particles using the model of (Berrouk *et al.*, 2007) agreed well with experimental data, and were superior to the results of RANS simulations. For large particles the statistics were shown to be sensitive to the value of β.

2.3.5 Other particle SGS models

In addition to the models considered in this thesis, several other particle SGS models have been proposed. Amiri and Hannani (2006) extended the model of of Fukagata *et al.* (2004) to account for fluid anisotropy by making use of damping functions to evaluate the SGS fluid velocities in the three principal directions. Their model improved particle turbulent intensities in turbulent channel flow compared to the isotropic model of Fukagata *et al.* (2004). Another "SGS Brownian" force model was proposed by Bini and Jones (2007). They introduced non-linearity into the SGS force term, which the authors argue is appropriate since experimental results have shown particle acceleration to be non-Gaussian.

Fede *et al.* (2006) proposed a stochastic model based on the earlier work of Simonin *et al.* (1993). Their model has many similarities with the model of Shotorban and Mashayek (2006). Both models use a Langevin equation and do not account for particle inertia, the crossing trajectory effect, the continuity effect or fluid anisotropy. The main difference between the two models is that Shotorban and Mashayek use a Langevin equation for the seen fluid velocity (u_s), while Fede *et al.* use a Langevin

equation for the SGS fluid velocity along an inertial particle's path (u_f''). Another difference is that Fede *et al.* chose to transport u_s using the particle velocities, but Shotorban and Mashayek used the fluid velocities to transport u_s. Both sets of authors used identical relationships to model the particle SGS Lagrangian integral timescale and the diffusion term. The results of Fede *et al.* (2006) showed their model improved particle kinetic energy statistics compared to LES with no model, but the random component of the model caused inferior particle distribution results.

The stochastic particle SGS model of Pozorski and Apte (2009) is similar to the model of Berrouk *et al.* (2007). Both models use a Langevin equation for the seen fluid fluid velocity and account for the crossing trajectory and continuity effects. However, the model of Pozorski and Apte (2009) neglects the fluid convective term and does not account for particle inertia. Pozorski and Apte's tests showed improved particle statistics relative to LES with no model, but also found results to be sensitive to the values of model constants.

Weil *et al.* (2004) and Vinkovic *et al.* (2006) each proposed a stochastic particle SGS model with the purpose of simulating particle dispersion in atmospheric flows. Both models used a Langevin equation and tracked inertial particles by treating them as fluid particles. Both sets of authors tested their model using a turbulent boundary layer and found that results agreed well with experimental data.

Khan *et al.* (2010) applied kinematic simulation (Fung *et al.*, 2006) to LES of particle-laden turbulence to model the SGS effects on particles. Based on a prescribed turbulent kinetic energy spectrum, a fluid SGS velocity field is generated using a large number of random orthogonal Fourier modes. The advantage of this method is that the generated fluid SGS velocity field can have an underlying structure. Therefore,

turbulent structures that are smaller than the filter size can possibly be accounted for. This is not possible for most stochastic models which treat the SGS field as white noise. The authors tested their model using LES of turbulent channel flow with a ribbed wall.

Spectrally Optimised Interpolation (SOI) is a rather unique particle SGS model that has been proposed by Gobert and Manhart (2011). SOI tries to model the SGS effects by taking advantage of the fluid velocity interpolation error. The concept is similar to using implicit LES as a fluid SGS model. In SOI, fluid velocity interpolation is optimized such that the particles see a specified energy spectrum. The goal of this method is that the correct spectrum is represented all the way down to the Kolmogorov scales, which is not possible for ADM. Gobert and Manhart tested SOI using forced isotropic turbulence in a box, and found that SOI generally yields superior particle results compared to ADM.

2.3.6 Relevant studies

Fede and Simonin (2006) and Jin *et al.* (2010) studied the influence of filtering on a variety of fluid and particle timescales, and other particle statistics. Some of the results of Jin *et al.* are of particular interest with respect to the model of Berrouk *et al.* (2007). Jin *et al.* determined that the assumption that β is constant across different scales of turbulence is not always valid, and that β can be a function of filter size. Their results showed that at the cut-off β can be greater than unity, which would drastically change the qualitative behaviour of the particle inertia correction given in equation (2.48).

The effect of filtering on preferential concentration was examined by Ray and

Collins (2011). Their results showed that filtering reduces particle clustering for small Stokes number particles, but increases particle clustering for high Stokes number particles. They explain both of these phenomena as follows. For small particles, preferential concentration is mostly due to the smallest eddies, so when these eddies are removed by filtering particle clustering is reduced. For large particles, the particle timescale is greater than that of the smallest eddies. Consequently, the smallest eddies randomize the motion of large particles which reduces preferential concentration, so when these eddies are removed clustering increases. The authors also found that filtering increases the particle timescale at which maximum particle clustering occurs.

Gobert (2010) and Gobert and Manhart (2010) assessed particle SGS models using analytical and numerical methods, respectively. They tested ADM and the stochastic models of Shotorban and Mashayek (2006) and Fede *et al.* (2006). For the numerical study (Gobert and Manhart, 2010) the models were tested using forced isotropic turbulence in a box with zero gravity. The authors examined fluid turbulent kinetic energy seen by the particles, particle turbulent kinetic energy and particle diffusivity. The authors did not test velocity autocorrelations and timescales, particle clustering, crossing trajectory and continuity effects, or the influence of filter size, all of which are considered in the current thesis. Gobert and Manhart found that ADM only recovered a portion of the SGS turbulent kinetic energy and underpredicted the rate of dispersion. The stochastic models that they tested performed poorly, especially for high inertia particles. There were no consistent differences between the stochastic models of Shotorban and Mashayek (2006) and Fede *et al.* (2006).

2.4 Summary

The chapter reviewed modeling of particle-laden turbulent flows, with a particular emphasis on particle-laden LES and modeling of SGS effects on particles. LES can be used to simulate industrial flows with high Reynolds numbers for which DNS is not practical due to the computational expense, and can provide superior accuracy compared to RANS methods. LES is particularly attractive for particulate flows since the interaction between turbulent structures and particles can be accounted for.

The physics of particles in turbulence was discussed in Section 2.2. There are numerous forces that act on a spherical particle in a turbulent flow. However, most forces are negligible when the particle density is much greater than that of the fluid, which is the case in this investigation. Only the drag and gravitational forces are considered in the current work. Important particle phenomena are the inertia effect, the crossing trajectory effect, the continuity effect and preferential concentration.

The mathematical description of particle dispersion in a turbulent flow is given by the work of Taylor (1921), who showed that at long times dispersion is dependent on the product of particle turbulent kinetic energy and the particle's Lagrangian integral timescale. Relating this result to LES, Taylor's work suggests that long term dispersion may not be significantly different in LES since filtering should decrease the particle turbulent kinetic and increase the Lagrangian integral timescale. However, all previous particle LES studies have found that LES causes a reduction in particle dispersion. This indicates that filtering has a more significant effect on particle turbulent kinetic energy than it does on the particle Lagrangian integral timescale.

Particle SGS models account for the effects of the small turbulent motions, which

are not resolved in LES, on particles. Several particle SGS models have been proposed in the literature. The goal of this thesis is to evaluate and compare some of the different models that exist. The particle SGS models tested here are the approximate deconvolution method (ADM), and the stochastic models of Fukagata *et al.* (2004), Shotorban and Mashayek (2006) and Berrouk *et al.* (2007). These models were selected based on the differences in their formulation, and how frequently they have been referenced in the literature. The model of Shotorban and Mashayek (2006) was selected instead of the model of Fede *et al.* (2006) since it is more closely related to the model of Berrouk *et al.* (2007), and the results of Gobert and Manhart (2010) showed similar performance between the two models. The particle statistics that are used to evaluate the models are turbulent kinetic energy of the particles and seen fluid, particle dispersion, Lagrangian autocorrelations of particle velocity and seen fluid velocity, and preferential concentration statistics. The models are tested under a variety of conditions by varying the following parameters: particle timescale, gravity (importance of CTE and continuity effect), filter size and model constant values.

Chapter 3

Methodology

3.1 Introduction

Details of the numerical solution techniques used to calculate the fluid field, calculate particle trajectories, implement particle SGS models and calculate relevant particle statistics are discussed in this chapter. Calculation of the carrier phase is done by using both LES and DNS. The particle SGS models are evaluated by comparing the model results to particle statistics obtained from tracking particles in the DNS velocity field.

3.1.1 Testing methodology

Particle SGS models are validated and tested using either *a posteriori* or *a priori* testing methods. A schematic of the two methods is presented in Figure 3.1. In *a posteriori* tests particles are tracked using the LES velocity field with the particle SGS models applied, and the results are compared with DNS or experimental data.

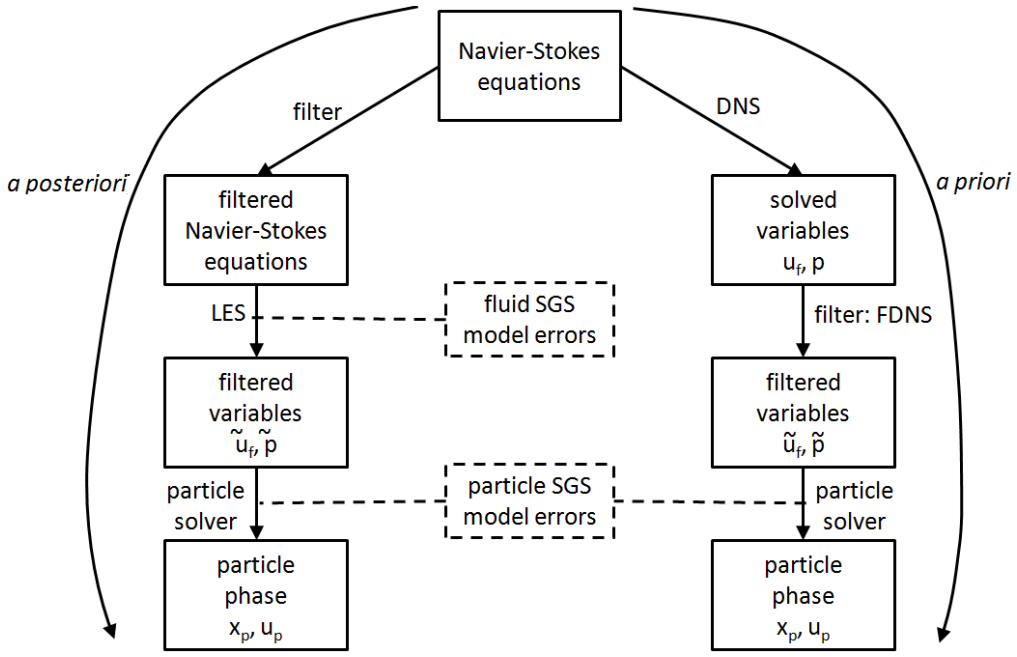

Figure 3.1: Diagram illustrating *a priori* and *a posteriori* testing methods.

The advantage of this method is that it tests how particle SGS models perform in a true LES simulation. Discrepancies between the DNS and LES particle statistics are due to errors in both the particle SGS and fluid SGS models. However, this can be undesirable for evaluating particle SGS models since it is very difficult to distinguish between the two types of errors. This complication is overcome by using *a priori* testing.

A priori tests involve tracking particles in a filtered DNS (FDNS) flow field. The FDNS velocity field is obtained by first performing a DNS, and then explicitly filtering the DNS to obtain a FDNS velocity field that does not contain any fluid SGS modeling errors. Therefore, *a priori* testing isolates the error that is caused by the particle SGS model. Both testing methods are used in the current work, but much more emphasis is put on the *a priori* results since they are superior for evaluating model formulation

and the ability of the models to capture SGS physics.

3.2 Fluid phase

3.2.1 OpenFOAM

Calculation of the DNS and LES velocity fields is done using the open source CFD package OpenFOAM. OpenFOAM is a collection of finite-volume method CFD solvers that are written in C++, and it is distributed for free under the GNU General Public License (OpenFOAM Foundation, 2011). OpenFOAM is well suited for very large simulations, such as DNS, since it runs in parallel using domain decomposition and is not subject to license constraints.

Many previous studies have been reported in the literature that have used OpenFOAM to simulate and model a variety of different fluid and energy processes. OpenFOAM has been used for LES [(Baba-Ahmadi and Tabor, 2008) (Tabor and Baba-Ahmadi, 2010) (Renze *et al.*, 2011) (Wang *et al.*, 2011)], particle tracking (Macpherson *et al.*, 2009), multiphase flows with the two-fluid model (Silva *et al.*, 2008), bubbly flows [(Selma *et al.*, 2010) (Renze *et al.*, 2011)] and water turbines (Nilsson, 2007). Excellent agreement has been reported between OpenFOAM and other CFD packages, such as ANSYS CFX and ANSYS Fluent, giving confidence that the code has been implemented correctly. The present study requires only basic components of OpenFOAM to solve the Navier-Stokes equations (2.1) and (2.2) for DNS, and the filtered Navier-Stokes equations (2.8) and (2.9) for LES.

3.2.2 DNS

The fluid phase is simulated using a DNS to solve the incompressible three-dimensional time-dependent Navier-Stokes equations for decaying, isotropic turbulence in a periodic box. This simple turbulent flow is a logical starting point for evaluating particle SGS models. The Eulerian velocity field is solved for in physical space on a Cartesian equidistant grid with 256 nodes in each direction. All spatial derivatives are evaluated using a fourth order scheme, and the simulation is advanced in time using a second order Crank-Nicolson method. The pressure term is treated using the Pressure Implicit Split Operator (PISO) method (Issa, 1986).

The initial velocity field is generated using a spectral method that produces a periodic box of isotropic, incompressible turbulence that is solenoidal and corresponds to a specified energy spectrum. The specified initial turbulent kinetic energy spectrum is the same as that used by Shotorban and Mashayek (2006):

$$E(\kappa) = E_a \left[\frac{\kappa}{\kappa_m} \right] \exp \left[-\frac{\kappa}{\kappa_m} \right] \tag{3.1}$$

where κ is the wavenumber, $E(\kappa)$ is the energy density, E_a is a constant, and κ_m is the wave number at which $E(\kappa)$ is maximum. In this study the parameters in (3.1) are set to the values $E_a = 800$ and $\kappa_m = 10$. Starting with the generated initial velocity field, the Navier-Stokes equations are advanced in time until an appropriate turbulent energy spectrum is obtained with a $-5/3$ spectrum in the inertial subrange. At this point the particles are inserted into the flow. Plots of the energy spectrum can be found in Appendix B. In this thesis, the initial time ($t = 0$) denotes the time at which the particles are inserted, and the DNS is run until a final time of $t = 7.5\,\mathrm{s}$.

Grid size		N^3	256^3
Domain length	(m)	L_0	1.0
Time	(s)	t	$0.0 \rightarrow 7.5$
DNS timestep	(s)	Δt	0.00025
Kinematic viscosity	(m^2/s)	ν	6×10^{-5}
Minimum wave number		κ_0	2π
Maximum wave number		κ_{max}	256π
Taylor scale Reynolds number		Re_λ	$74 \rightarrow 39$
Fluid turbulent kinetic energy	(m^2/s^2)	k	$0.0889 \rightarrow 0.0027$
RMS turbulent velocity	(m/s)	u'_{rms}	$0.243 \rightarrow 0.043$
Dissipation rate	(m^2/s^3)	ϵ	$0.16030 \rightarrow 0.00054$
Eulerian integral length scale	(m)	$L_{E,f}$	$0.087 \rightarrow 0.152$
Eulerian integral timescale	(s)	$T_{E,f}$	$0.36 \rightarrow 3.56$
Taylor microscale	(m)	λ	$0.018 \rightarrow 0.055$
Kolmogorov length scale	(m)	η_K	$0.0011 \rightarrow 0.0045$
Kolmogorov timescale	(s)	τ_K	$0.019 \rightarrow 0.332$
Spatial resolution		$\kappa_{max}\eta_K$	$0.87 \rightarrow 3.59$

Table 3.1: DNS fluid properties. Properties with two values are at the initial ($t = 0.0\,\mathrm{s}$) and final ($t = 7.5\,\mathrm{s}$) simulation times.

Properties of the DNS are listed in Table 3.1. More extensive details of the DNS results are given in Appendix B. In order to evaluate particle SGS models, it is essential that we have confidence in the DNS. The following were considered to verify the correctness of the DNS: sufficient spatial resolution, timestep independence, appropriate turbulent kinetic energy spectrum, temporal evolution of the skewness of the streamwise velocity derivative, isotropy, and rate of decay of turbulent kinetic energy and dissipation rate.

3.2.3 Filtering

Explicit filtering is performed to obtain the FDNS flow fields, and for the ADM model. In *a priori*, the FDNS field is obtain by explicitly filtering the DNS velocity field. The

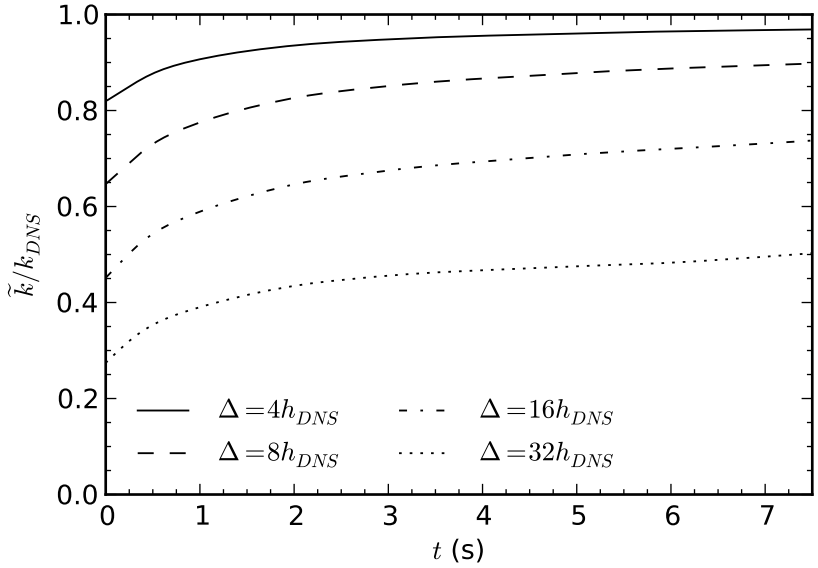

Figure 3.2: Turbulent kinetic energy of the FDNS fluid fields normalized by the turbulent kinetic energy of the DNS.

three-dimensional filtering operation using a filter kernel G is defined as

$$\widetilde{\phi}(\vec{x},t) = \int_V G(\vec{r})\phi(\vec{x}-\vec{r},t)d\vec{r} \tag{3.2}$$

where ϕ is the variable to be filtered and V is entire domain volume. The most commonly used filter functions are the top-hat and Gaussian filters. The sharp spectral filter function is often used when performing LES in spectral space. Previous *a priori* particle-laden LES studies have shown that the filter type has little influence on particle statistics (Armenio *et al.*, 1999) (Shotorban and Mashayek, 2006).

In this study, all filtering operations are performed using the Gaussian filter function. The Gaussian filter kernel is:

$$G(\vec{r}) = \prod_{i=1}^{3}\left(\frac{\alpha}{\pi\Delta^2}\right)^{1/2}\exp\left[-\alpha\frac{r_i^2}{\Delta^2}\right] \tag{3.3}$$

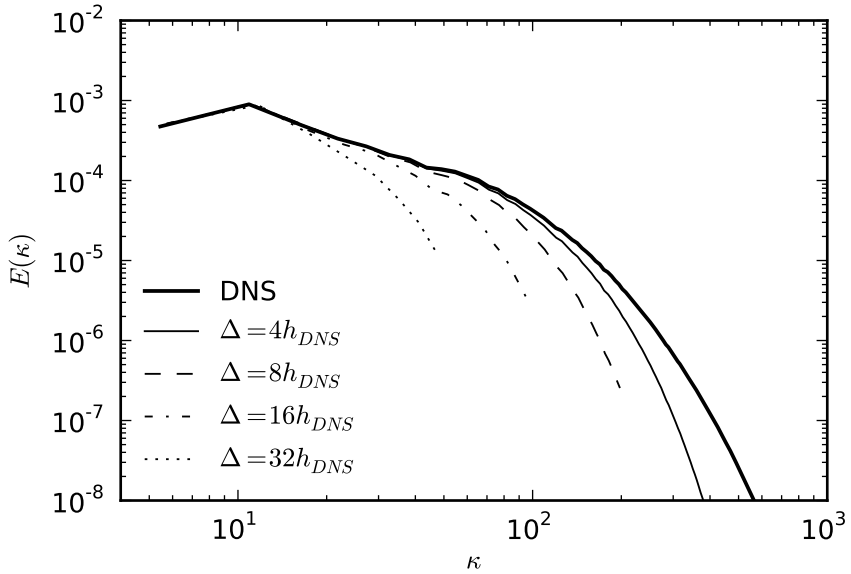

Figure 3.3: Turbulent kinetic energy spectra of the FDNS fluid fields at $t = 2.5s$.

In this thesis the constant α is set to $\alpha = 6$, which is often used in the literature (Geurts, 2004). To perform the filtering operation, the Gaussian filter is clipped so that only nodes within $|\vec{r}| \leq 3\Delta$ are included in the numerical integration.

Four different FDNS fluid fields, which are generated using different filter sizes, are used in the *a priori* testing. The filter sizes are $\Delta = 4h_{DNS}$, $\Delta = 8h_{DNS}$, $\Delta = 16h_{DNS}$, and $\Delta = 32h_{DNS}$, where h_{DNS} is the DNS grid spacing. In all cases the FDNS grid spacing is half of the filter size $h_{FDNS} = \frac{1}{2}\Delta$, which ensures that turbulent scales at the filter cut-off are properly represented.

The amount of energy resolved in each of the FDNS fluid fields is shown Figure 3.2. The percentage of resolved energy increases with time since the smallest turbulent scales get larger but the size of the cut-off scale remains constant. In practice, resolving about 80% of the bulk energy is considered to be a fairly well resolved LES. The turbulent kinetic energy spectra of the FDNS and DNS fields at $t = 2.5s$ are shown

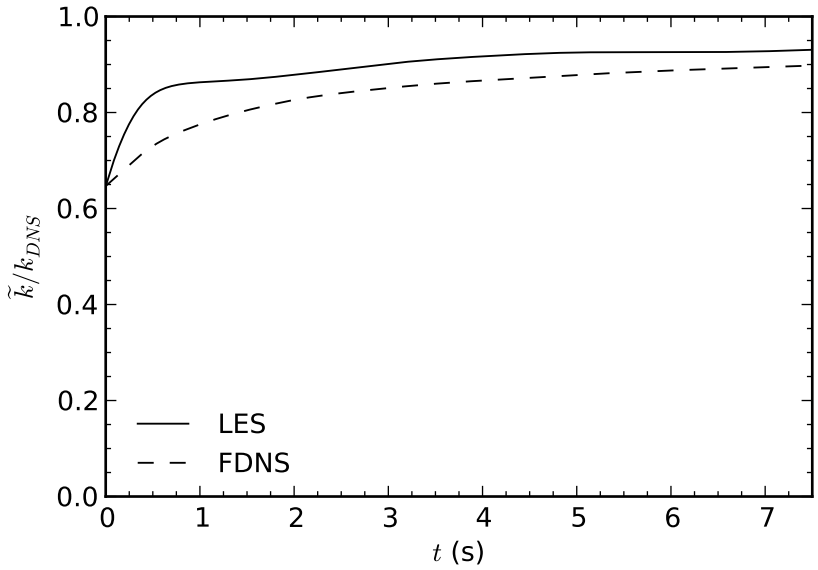

Figure 3.4: Turbulent kinetic energy of the LES and FDNS fluid fields normalized by the turbulent kinetic energy of the DNS. The LES and FDNS filter size is $\Delta = 8h_{DNS}$.

in Figure 3.3. As the filter size is increased the cut-off wavenumber is decreased and less turbulent kinetic energy is resolved.

3.2.4 LES

LES of decaying isotropic turbulence in a periodic box was performed for the *a posteriori* study. The dynamic Smagorinsky model proposed by Germano *et al.* (1991) and later modified by Lilly (1992) was used as the fluid SGS model. The filtered Navier-Stokes equations were solved on a 64^3 grid with a single filter size of $\Delta = 8h_{DNS}$. The initial condition was obtained in two steps. Firstly, a DNS field prior to the initial time ($t < 0$) was filtered. Secondly, starting with this filtered field the LES was advanced in time until the resolved turbulent kinetic energy was equal to that of the corresponding FDNS velocity field at time zero ($\widetilde{k}_{LES} = \widetilde{k}_{FDNS}(\Delta = 8h_{DNS}, t = 0)$).

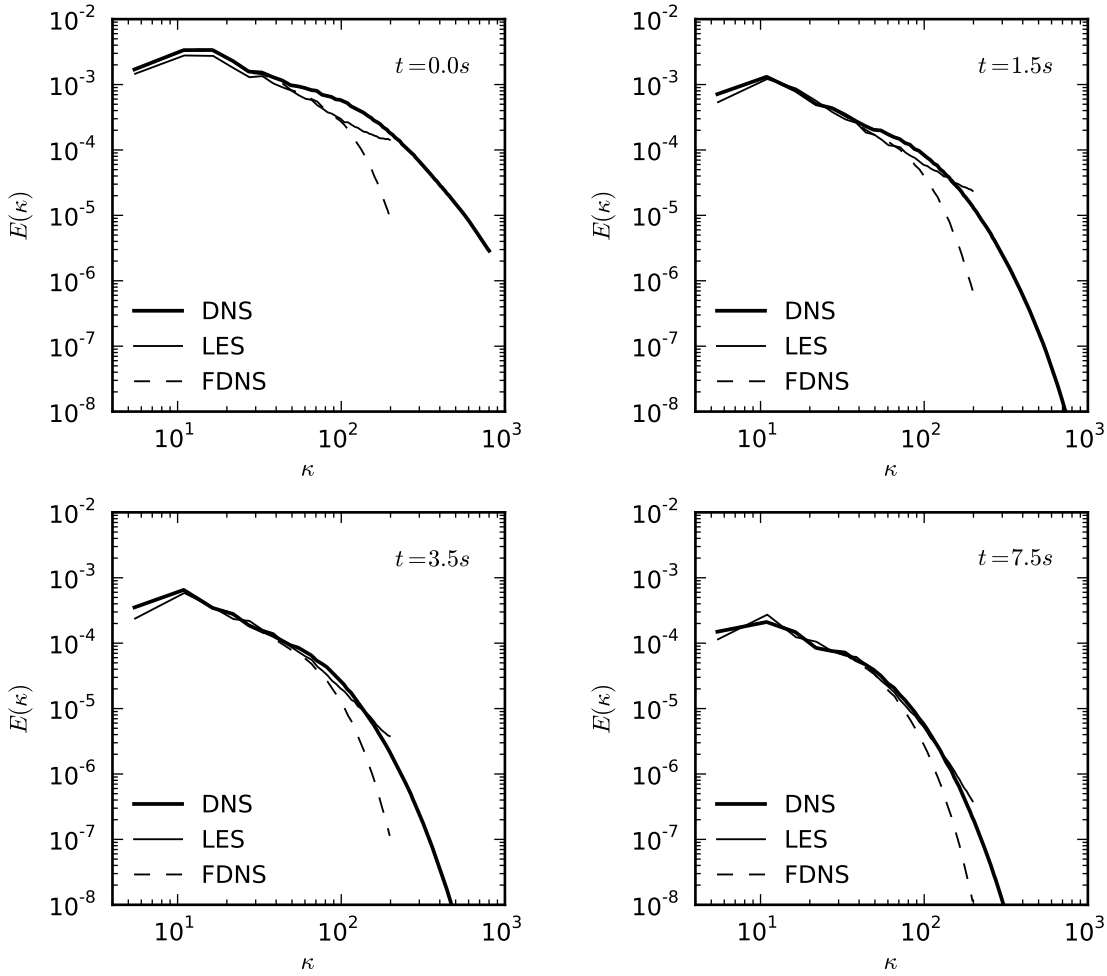

Figure 3.5: Turbulent kinetic energy spectra of the LES, FDNS and DNS fluid fields at various times. The LES and FDNS filter size is $\Delta = 8h_{DNS}$.

This resulting LES field was used as the initial condition for the particle-laden LES. The timestep used in the LES is twice that of the DNS ($(\Delta t)_{LES} = 0.00050s$), but the LES Courant is much lower since $\widetilde{u_f}$ is solved for instead of u_f.

The LES filtered kinetic energy normalized by the DNS kinetic energy is shown in Figure 3.4, and the LES energy spectrum at multiple times is shown in Figure 3.5. Throughout the simulation the LES filtered kinetic energy is greater than that of the FDNS since the LES has a smaller rate of decay, particularly at early times. This is

caused by differences in the energy spectra of the resolved scales, and due to errors with the fluid SGS model for scales smaller than the cut-off. The LES energy spectra are similar to what a sharp spectral filter would produce, with more energy contained at scales near the cut-off. If forced turbulence was simulated then the kinetic energy of the LES and FDNS fields would be identical and constant in time. However, differences could still exist between the energy spectra and dissipation rates.

3.3 Particle phase

3.3.1 Particle tracking

The particles are assumed to be perfectly spherical with a density much greater than that of the fluid, and as a result only the drag force and gravity force are important. It also assumed that the particles are small and the mixture is dilute such that particle-particle interactions can be ignored, and the particles have no effect on the carrier fluid. Therefore, the particle equation of motion that is used in this work, which was previously given in (2.20), is:

$$\frac{du_{p,i}}{dt} = \frac{f}{\tau_p}(u_{f,i} - u_{p,i}) + g_i \tag{3.4}$$

It is solved numerically using a fourth order Adams-Bashforth method:

$$u_{p,i}(t_n) = u_{p,i}(t_{n-1}) + \left[\frac{55}{24}\frac{du_{p,i}}{dt}(t_{n-1}) - \frac{59}{24}\frac{du_{p,i}}{dt}(t_{n-2}) + \frac{37}{24}\frac{du_{p,i}}{dt}(t_{n-3}) - \frac{3}{8}\frac{du_{p,i}}{dt}(t_{n-4})\right]\Delta t \tag{3.5}$$

where t_n is the current timestep and t_{n-1} is the previous timestep. The equation for particle position is

$$\frac{dx_{p,i}}{dt} = u_{p,i} \tag{3.6}$$

A fourth order Adams-Bashforth method is used to numerically solve the particle position equation:

$$x_{p,i}(t_n) = x_{p,i}(t_{n-1}) + \left[\frac{55}{24}u_{p,i}(t_{n-1}) - \frac{59}{24}u_{p,i}(t_{n-2}) + \frac{37}{24}u_{p,i}(t_{n-3}) - \frac{3}{8}u_{p,i}(t_{n-4})\right]\Delta t \tag{3.7}$$

The particle equation of motion and position equation are solved using Euler, second order Adams-Bashforth, and third order Adams-Bashforth methods for the first, second and third timesteps of the simulation, respectively.

The fluid field is solved using OpenFOAM and the output is written to disk. The particles are tracked in a separate Fortran program with the fluid field from OpenFOAM read in from disk. The particles are injected into the flow at $t = 0$ on a uniform grid, and initially their velocities are set to the local fluid velocity $u_{p,i}(t = 0) = u_{f,i}[x_{p,i}(t = 0), t = 0]$. All spatial interpolations, such as interpolating fluid velocities to the particle's position, are done using a third order Hermite polynomial interpolation scheme as recommended by Strutt *et al.* (2011). A particle timestep of $\Delta t = 0.001s$ was selected based on a particle timestep independence test. Details of the particle timestep independence test are given in Appendix C.

Type ID	P1	P2	P3	P4	P5	P6	P7	P8	P9
d_p (μm)	100	163	209	267	302	341	436	557	910
ρ_p/ρ_f	2000	2000	2000	2000	2000	2000	2000	2000	2000
τ_p (s)	0.019	0.049	0.081	0.132	0.169	0.215	0.352	0.575	1.534
$\mathrm{St}_{\eta_K}(t = t_0)$	0.50	1.32	2.17	3.53	4.52	5.76	9.42	15.38	41.04
$d_p/\eta_K(t = t_0)$	0.07	0.11	0.14	0.18	0.20	0.23	0.29	0.37	0.61

Table 3.2: Particle properties. $t_0 = 0.5\,\mathrm{s}$.

3.3.2 Particle parameters

The Stokes number based on the Kolmogorov timescale is defined as $\mathrm{St}_{\eta_K} = \tau_p/\tau_K$. A range of Stokes numbers are tested by using nine different types of particles, which are listed in Table 3.2. The type ID notation is used in this thesis to identify the type of particle. In the table, the Stokes number and size ratio are specified for time $t = 0.5\,\mathrm{s}$, which is the earliest time that particle statistics are considered (this will be discussed in Section 3.3.4). For all particle types the density ratio is set to $\rho_p/\rho_f = 2000$, and the particle diameter is varied among the different groups. The particle diameters were selected to create an acceptable distribution of Stokes numbers, which is shown in Figure 3.6. The Stokes numbers decrease with time since τ_p remains constant but τ_K increases as the Kolmogorov scales get larger with time. A greater number of particle types with Stokes number close to unity were tested since preferential concentration is most significant for these particles. The assumption that particles are small ($d_p/\eta_K \leq 1$) is valid for all particle types throughout the entire simulation.

Each particle group consists of $N_p = 262,144$ particles initially placed on a 64^3 uniform grid at time $t = 0$. This was determined to be a sufficient number of particles based on an independence test. The independence test consisted of tracking particles in the DNS flow field and examining particle statistics that are used in this study.

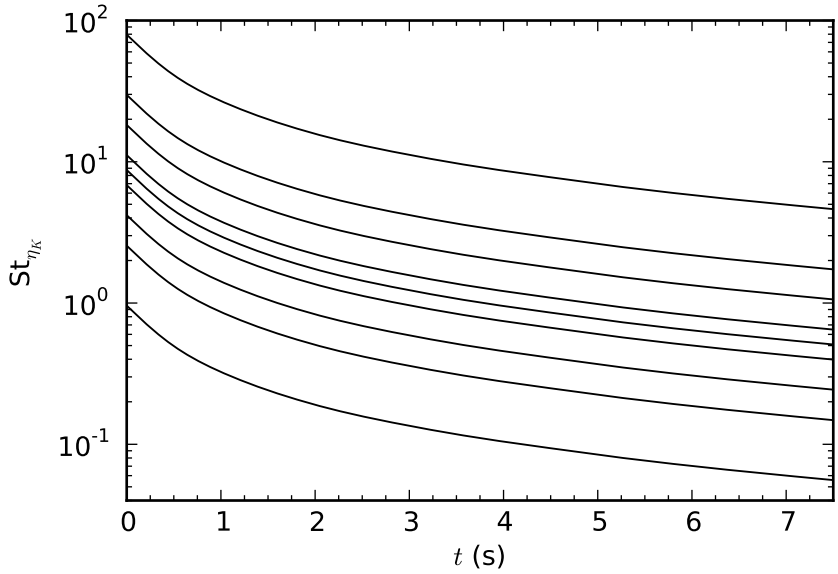

Figure 3.6: Stokes number as a function of time for the nine different types of particles listed in Table 3.2.

Further details of the independence test are given in Appendix C.

3.3.3 Gravity

Simulations with and without gravity were conducted. Including gravity is required to evaluate the ability of particle SGS models to predict the crossing trajectory and continuity effects.

The choice of the gravitational constant used in the particle equation of motion is restricted by the time it takes a particle to traverse the domain, and the total length of time simulated. If a particle travels the length of the domain then it ends up in roughly the same location as it started since periodic boundary conditions are used. If this occurs too quickly, then the particle will enter the same turbulent structure that it started in. As a result, the particle will see fluid velocities that are highly correlated

to the initial conditions, which is unphysical and incorrect. Therefore, the mean drift velocity must be limited so that this does not occur. The maximum acceptable value for the mean drift velocity was determined to be $u_d = 0.1\,\mathrm{m/s}$. This value was determined by examining the Eulerian temporal autocorrelation coefficient function of the fluid velocity, and running particle-laden flow tests with various gravitational constant values.

For each particle type the mean drift velocity was chosen to be $u_d = 0.1\,\mathrm{m/s}$, and this was set by using a different gravitational constant value for each type of particle. Ideally, the same gravitational constant should be used for all particle types. If the gravity value was set based on the largest particles and the maximum allowable mean drift velocity, then the CTE and continuity effect would be insignificant for the small and medium sized particles. Wells and Stock (1983) determined that the CTE is fairly insignificant if $u_d/u'_{f,rms} < 1$. The parameter $u_d/u'_{f,rms}$ as function of time is plotted in Figure 3.7 for $u_d = 0.1\,\mathrm{m/s}$, which shows that for the majority of the simulation $u_d/u'_{f,rms} > 1$. Using this method of setting $u_d = 0.1\,\mathrm{m/s}$ for all particle types allows for the CTE and continuity effect to be examined for a range of Stokes numbers, and for the effect of particle inertia in the presence of gravity to also be tested.

Calculation of the gravitational constant for each particle type is done by setting the particle acceleration and fluid velocity to zero (since there is no mean fluid flow) in the particle equation of motion:

$$0 = \frac{f}{\tau_p}(0 - u_d) + g \tag{3.8}$$

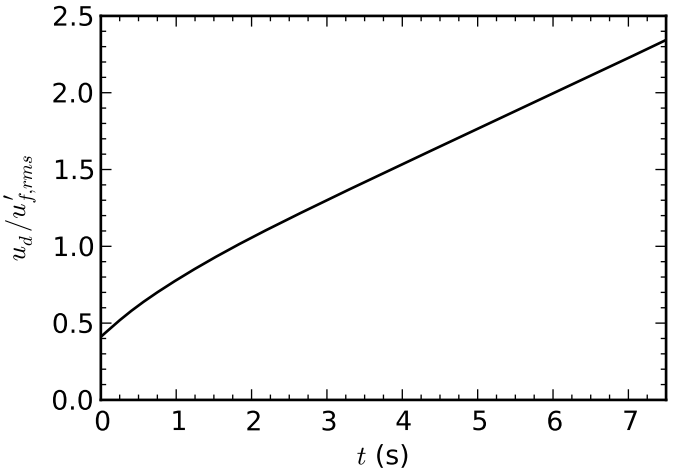

Figure 3.7: Time development of $u_d/u'_{f,rms}$ for $u_d = 0.1\,\mathrm{m/s}$. The importance of the crossing trajectory and continuity effects increases as $u_d/u'_{f,rms}$ increases.

Substituting in the appropriate relationships for τ_p and f, and rearranging gives:

$$g = \frac{18 u_d \nu}{(\rho_p/\rho_f) d_p^2} \left[1 + 0.15 \left(\frac{d_p u_d}{\nu} \right)^{0.687} \right] \tag{3.9}$$

For $u_d = 0.1\,\mathrm{m/s}$ and the nine particle types used in this work, (3.9) gives gravitational constant values ranging from 0.078 to 5.6 $\mathrm{m/s^2}$. The direction of gravitational acceleration is selected to be in the negative x_3 direction.

For simulations with gravity, the initial particle velocity is set to the local fluid velocity plus the mean drift velocity $u_{p,i}(t=0) = u_{f,i}[x_{p,i}(t=0), t=0] + (u_d)_i$.

3.3.4 Selection of t_0

The variable t_0 is the earliest time that particle statistics are examined and used to compare the different particle SGS models. Ideally, t_0 should be chosen to be the time when the particles become independent of their initial conditions, which is denoted by

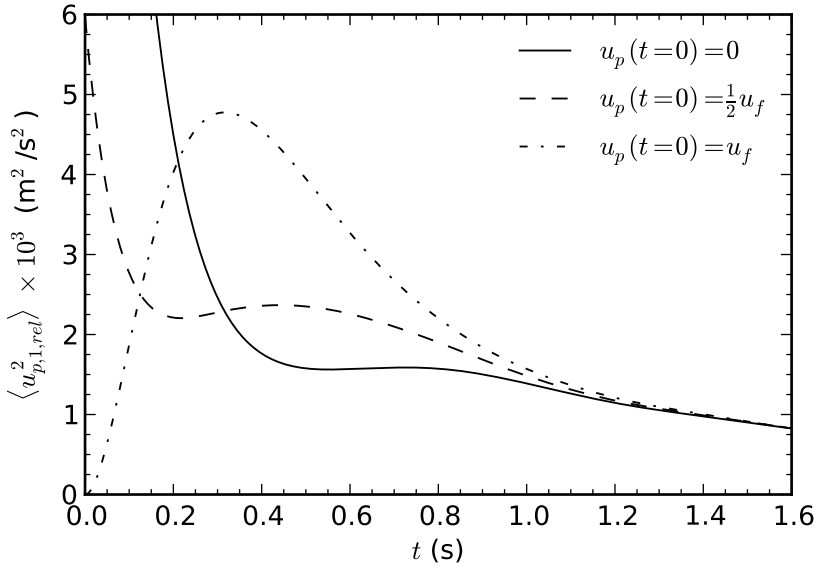

Figure 3.8: Mean squared relative velocity of P7 type particles in the $\Delta = 16h_{DNS}$ FDNS flow field with zero gravity, using three different sets of particle initial conditions. The particles are independent of their initial conditions once the lines converge.

t^*. In the large majority of the literature, t^* is determined using a method first used by Riley and Patterson (1974). They used the time at which the mean squared relative velocity reached a maximum value to indicate when the particles are independent of their initial conditions. The mean squared relative velocity is defined as:

$$\left\langle u^2_{p,i,rel} \right\rangle = \left\langle [u_{p,i} - u_{f@p,i}]^2 \right\rangle \tag{3.10}$$

Riley and Patterson did not provide any insight into why the peak of $\left\langle u^2_{p,i,rel} \right\rangle$ would indicate that the particles are independent of their initial conditions, nor have any subsequent researchers.

Strutt *et al.* (2011) showed that the traditional peak mean squared relative velocity method may not be sufficient to indicate independence of initial conditions

Particle type		P1	P5	P7	P8	P9
t^* (s)	$\Delta = 8h_{DNS}$	0.111	0.666	1.172	1.533	3.726
	$\Delta = 16h_{DNS}$	0.128	0.725	1.428	1.754	4.378

Table 3.3: Time required for particles to become independent of initial conditions (t^*) using the method proposed by Strutt *et al.* (2011). Results are for two different filter size FDNS flow fields with zero gravity.

for particles. They proposed another method which is used in this work. In their method, t^* is found by tracking multiple sets of particles with different initial conditions, and observing the time at which particle statistics, such as $\langle u^2_{p,i,rel} \rangle$, become identical for the different particle sets. Three sets of different initial conditions are used in this work: $u_p(t=0) = 0$, $u_p(t=0) = \frac{1}{2}u_f$ and $u_p(t=0) = u_f$. This method is demonstrated in Figure 3.8. The results for various particle types and filter sizes are summarized in Table 3.3. The time t^* is taken to be the time when the difference between the $u_p(t=0) = \frac{1}{2}u_f$ and $u_p(t=0) = u_f$ results is less than 1.0%. The time for particles to become independent of initial conditions increases with both the particle relaxation time and filter size. Gravity had a small influence on t^*, but no consistent trend was observed.

The earliest time that particle statistics are considered was chosen to be $t_0 = 0.5\,\mathrm{s}$ for the particle simulations in this study. Comparing this to the t^* values listed in Table 3.3, the larger particles are not yet independent of their initial conditions at this time. There are difficulties with choosing t_0 for particles in decaying turbulence. Ideally, the Reynolds number and time frame during which particle statistics are examined should be maximized. However, both of these parameters would be unacceptably small if t_0 was selected so that $t_0 \geq t^*$ for all particle types. The goal of this work is to examine and compare various particle SGS models. To test if the selected

value of $t_0 = 0.5\,\mathrm{s}$ is acceptable, a second set of model simulations was run using $t_0 = 1.8\,\mathrm{s}$. This corresponds to the smallest eight particle sizes being independent of their initial conditions. The results from the $t_0 = 1.8\,\mathrm{s}$ simulations yielded the same conclusions regarding the particle SGS models as the $t_0 = 0.5\,\mathrm{s}$ simulations. This indicates that the selection of $t_0 = 0.5\,\mathrm{s}$ should be acceptable and not influence conclusions regarding the particle SGS models.

3.3.5 Particle statistics

This section reviews the particle statistics that are considered in this work. The turbulent kinetic energy of the particles (k_p), the seen fluid velocity (k_s), and the filtered fluid velocity at the particles' position ($\widetilde{k}_{f@p}$) are defined as:

$$k_p = \left\langle \frac{1}{2} u'_{p,i} u'_{p,i} \right\rangle \tag{3.11}$$

$$k_s = \left\langle \frac{1}{2} u'_{s,i} u'_{s,i} \right\rangle \tag{3.12}$$

$$\widetilde{k}_{f@p} = \left\langle \frac{1}{2} \widetilde{u}_{f@p,i} \widetilde{u}_{f@p,i} \right\rangle \tag{3.13}$$

The particle mean square dispersion $\left\langle x^2_{p,i} \right\rangle$, and rate of dispersion $D_{p,i}$ (also known as dispersion coefficient or particle turbulent diffusivity) are calculated as:

$$\left\langle x^2_{p,i} \right\rangle = \left\langle [x_{p,i}(t) - x_{p,i}(t_0)]^2 \right\rangle \tag{3.14}$$

$$D_{p,i} = \frac{1}{2} \frac{d}{dt} \left\langle x^2_{p,i} \right\rangle \tag{3.15}$$

For (3.14) only turbulent dispersion is considered. Therefore, when gravity is included the distance a particle travels due to the mean particle velocity is subtracted from $x_{p,i}(t)$. The time derivative in (3.15) is calculated using a fourth order central difference scheme.

The Lagrangian autocorrelation coefficient functions of the particle velocity $R_{Lp,i}(t,\tau)$ and seen fluid velocity along a particle's path $R_{Lu_s,i}(t,\tau)$ are examined in this thesis.

$$R_{Lp,i}(t,\tau) = \frac{\left\langle u_{p,i}(t)u_{p,i}(t+\tau)\right\rangle}{[\left\langle u_{p,i}^2(t)\right\rangle]^{1/2}[\left\langle u_{p,i}^2(t+\tau)\right\rangle]^{1/2}} \tag{3.16}$$

$$R_{Lu_s,i}(t,\tau) = \frac{\left\langle u_{s,i}(t)u_{s,i}(t+\tau)\right\rangle}{[\left\langle u_{s,i}^2(t)\right\rangle]^{1/2}[\left\langle u_{s,i}^2(t+\tau)\right\rangle]^{1/2}} \tag{3.17}$$

where t is start time for calculation of the autocorrelation function, and τ is the time that has elapsed since t. In statistically stationary turbulence the autocorrelation functions are independent of the choice of t. However, for decaying turbulence the autocorrelation functions depend on the choice of t since the turbulent kinetic energy of the fluid and of the particles are not constant in time. In this study, only autocorrelation functions with $t = t_0$ are considered.

The fractal dimension d_{pc}, also called the correlation dimension, and the radial distribution function $g(r_i)$ are measures of preferential concentration. The fractal dimension measures the spatial dimension of the particle distribution. It is evaluated by first calculating the number of particles $N_p(r_i)$ within a sphere of radius r_i, with its origin at some base particle. The fractal dimension is then found by calculating the slope of $\log[N_p(r_i)]$ vs. $\log[r_i]$. A fractal dimension of $d_{pc} = 2$ corresponds to particles aligned on a surface, and $d_{pc} = 3$ corresponds to a random distribution with uniform probability throughout the volume of the domain. Particle clustering due to

preferential concentration causes the fractal dimension to be less than three ($d_{pc} < 3$).

The radial distribution function (RDF) $g(r_i)$ is the ratio of the number of particle pairs with a separation distance r_i to the expected number if the particles had a uniformly random distribution. It is calculated as:

$$g(r_i) = \frac{P_i/V_i}{P/V} \tag{3.18}$$

where P_i is the number of particle pairs within a separation distance between $(r_i - \Delta r/2)$ and $(r_i + \Delta r/2)$, $P = N_p(N_p - 1)/2$ is the total number of particle pairs, $V_i = \frac{4}{3}\pi[(r_i + \Delta r/2)^3 - (r_i - \Delta r/2)^3]$ is volume of the elemental shell, and V is the total domain volume. In this study, the shell thickness used for binning the particles is chosen to be $\Delta r = 0.3 h_{DNS}$. The radial distribution function and fractal dimension are calculated at every multiple of $t = 0.5\,\mathrm{s}$ during the particle simulation.

3.3.6 DNS fluid particle results

The results of fluid particles tracked in the DNS fluid field were examined to ensure that the code has been implemented correctly. Firstly, fluid particle dispersion is compared with Taylor's theorem, which is shown in Figure 3.9. The two lines plotted for Taylor's result are $\left\langle x_{p,i}^2 \right\rangle \propto t^2$ for short times and $\left\langle x_{p,i}^2 \right\rangle \propto t$ for long times. For short times the fluid particle results have identical behaviour to Taylor's theorem. At long times the agreement is also good, but the fluid particle results are not perfectly linear. This discrepancy is because Taylor's result is for stationary turbulence, not decaying turbulence. This long time behaviour for particles in decaying turbulence has also been observed in previous studies (Elghobashi and Truesdell, 1992).

The normalized turbulent kinetic energies of the particles and seen fluid velocity,

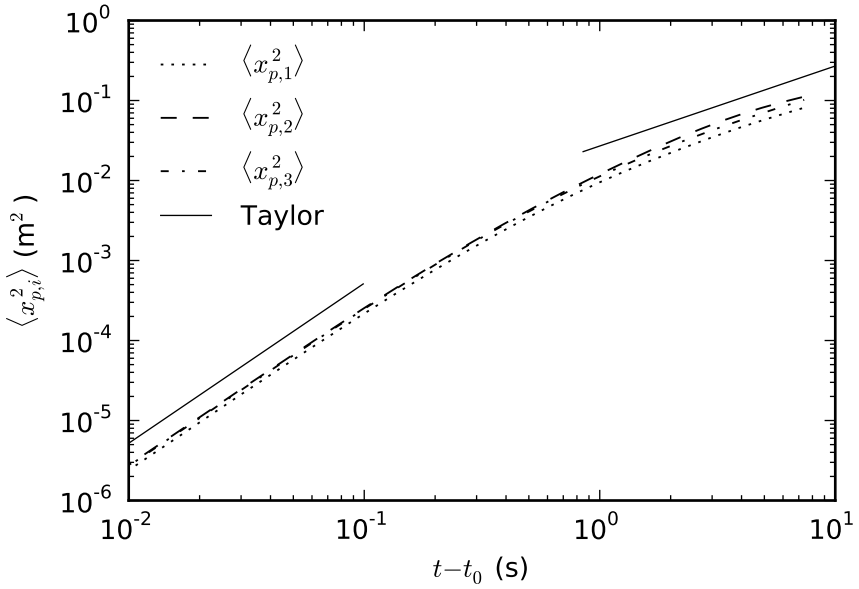

Figure 3.9: Dispersion of fluid particles in the DNS flow field compared with Taylor's theorem.

and the fractal dimension are shown in Figure 3.10. For fluid particles, the turbulent kinetic energy of the particles and of the seen fluid velocity should be equal to the fluid turbulent kinetic energy at all times, which is the case in Figure 3.10. Fluid particles should have a uniform spatial distribution. Therefore, there should be no particle clustering and the fractal dimension should be $d_{pc} = 3$. This behaviour is observed in Figure 3.10. Furthermore, the RDF for the fluid particles (not shown) is approximately unity for all separation distances and at all times.

3.4 Particle subgrid scale models

This section details the implementation of the particle SGS models that are tested in this work. These models are the approximate deconvolution method (ADM), and the stochastic models proposed by Fukagata *et al.* (2004), Shotorban and Mashayek

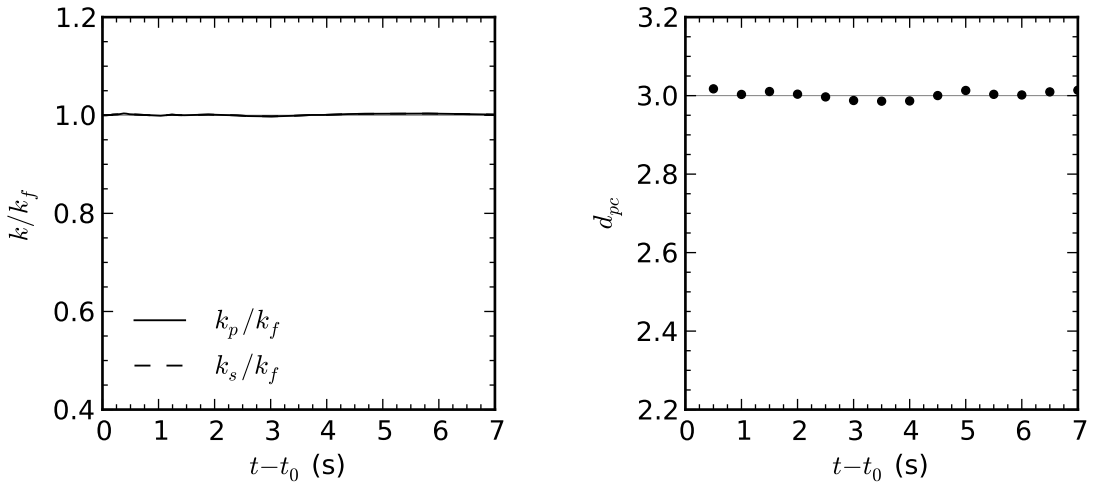

Figure 3.10: Time development of the particle and seen turbulent kinetic energies (left), and fractal dimension (right) for fluid particles in the DNS flow field.

(2006), and Berrouk *et al.* (2007). All of these models were previously reviewed in Section 2.3.

3.4.1 ADM

ADM is implemented by consecutively filtering the FDNS field and then using the truncated Van Cittert series expansion previously given in equation (2.34), which is :

$$u_{s,i} = \sum_{\alpha=0}^{m} (1 - G)^{\alpha} * \widetilde{u_{f,i}} \tag{3.19}$$

The filtering operations are performed as described in Section 3.2.3, and the same grid is used as that of the FDNS field.

The truncation level (m) used for the Van Cittert series expansion must be selected. Previous studies have used $m = 1$ and $m = 2$ (Shotorban and Mashayek, 2005) (Shotorban *et al.*, 2007), and $m = 5$ (Kuerten, 2006). In this work, ADM is

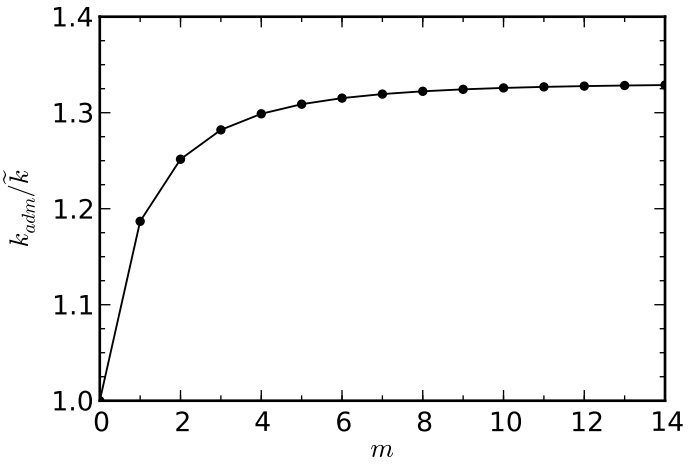

Figure 3.11: Ratio of ADM to FDNS turbulent kinetic energies as a function of Van Cittert series truncation level. FNDS field is $\Delta = 8h_{DNS}$ at time $t = 0$.

performed using both $m = 2$ and $m = 11$. ADM with $m = 2$ was chosen to represent a realistic implementation that could be used in practical applications. At this truncation level the FDNS field must only be filtered two additional times, which is reasonable. ADM with $m = 11$ was chosen to represent a "perfect" ADM implementation ($m \to \infty$). Figure 3.11 shows the amount of energy that is added to the ADM flow field, for $\Delta = 8h_{DNS}$ and at time $t = 0$, by including additional terms in the series expansion up to $m = 14$. The marginal amount of energy that is added for larger m values is very small. A horizontal asymptote for Figure 3.11 was estimated by fitting an exponential function using a least squares method. Using a criteria of at least 99% of the added energy associated with the asymptotic value, $m = 11$ was selected as the "perfect" case.

Turbulent kinetic energy spectra for the ADM velocity fields are shown in Figure 3.12. The corresponding DNS and FDNS spectra are also shown for comparison.

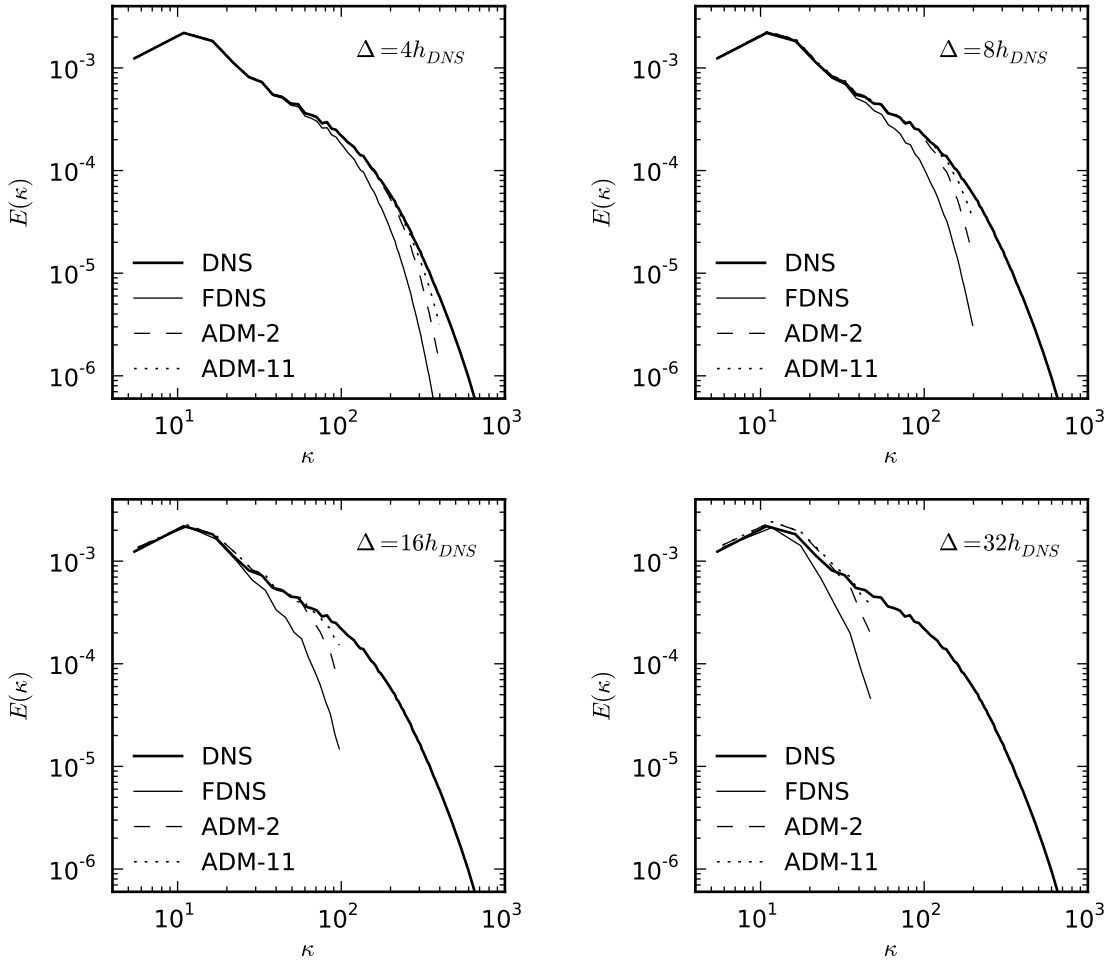

Figure 3.12: Turbulent kinetic energy spectra of the DNS, FDNS, and ADM velocity fields at time $t_0 = 0.5\,\mathrm{s}$ for the four different filter sizes.

Figure 3.12 shows that ADM enhances scales near the cut-off by mimicking the behaviour of a sharp spectral filter. However, ADM only recovers a portion of the SGS turbulent kinetic energy since it cannot recover any energy associated with scales smaller than the LES grid.

3.4.2 Gaussian random numbers

All three of the stochastic particle SGS models require random numbers with a Gaussian distribution. The Box-Muller algorithm (Box and Muller, 1958) is used to generate a Gaussian random number (ξ) with zero mean and unit variance:

$$\xi = \big[-2\ln(U_1)\big]^{1/2}\cos(2\pi U_2) \tag{3.20}$$

where U_1 and U_2 are independent random variables with uniform distributions in the interval $(0, 1)$.

3.4.3 Wiener process

The Wiener process W_i is present in both of the models that are based on a Langevin equation. The Wiener process is a Gaussian stochastic process that is continuous in time, and is frequently used to model Gaussian white noise. The increment in the Wiener process dW_i is a Gaussian random variable with zero mean and variance dt (Pope, 1994). In three dimensional space, the directional Wiener process increments are calculated as (Pope, 2000):

$$\Delta W_i = \sqrt{\Delta t}\,\xi_i \tag{3.21}$$

where $i = 1, 2, 3$, Δt is the simulation timestep, and ξ is a Gaussian random number with zero mean and unit variance. The Wiener process increment ΔW_i is an independent random variable.

3.4.4 Lagrangian fluid SGS timescale

The stochastic particle SGS models require the Lagrangian fluid SGS timescale. In this study $T_{L,sgs}$ is calculated using the relationship given by Gicquel *et al.* (2002) and Heinz (2003):

$$T_{L,sgs} = \left(\frac{1}{2} + \frac{3}{4}C_0\right)^{-1} \frac{k_{sgs}}{\epsilon_{sgs}} \tag{3.22}$$

For the models of Fukagata *et al.* (2004) and Shotorban and Mashayek (2006) the SGS fluid Lagrangian timescale along an inertial particle's path ($T^*_{L,sgs}$) is calculated using (3.22) since these models assume $T^*_{L,sgs} = T_{L,sgs}$.

3.4.5 SGS turbulent kinetic energy and dissipation rate

The SGS turbulent kinetic energy at the particle's location is needed for each of the stochastic particle SGS models. For the *a priori* testing the k_{sgs} field is calculated directly from the DNS and FDNS velocity fields without the use of any modeling. This is done by taking the trace of the SGS stress tensor (Meneveau and O'Neil, 1994):

$$k_{sgs} = \frac{1}{2}\tau_{ii} = \frac{1}{2}\left(\widetilde{u_{f,i}u_{f,i}} - \widetilde{u_{f,i}}\widetilde{u_{f,i}}\right) \tag{3.23}$$

The goal of this thesis is to evaluate the performance and formulation of particle SGS models. Testing models used for estimating k_{sgs} is therefore out of scope of the current work. Calculating k_{sgs} using (3.23) in the *a priori* testing allows for the particle SGS models to be tested without any modeling errors due to the calculation of k_{sgs}.

The SGS turbulent kinetic energy must be calculated with a model for the *a posteriori* testing. Numerous models have been proposed in the literature. In this work

k_{sgs} is calculated using a method that is consistent with the dynamic Smagorinsky model (Lilly, 1992):

$$k_{sgs} = C_I \Delta^2 |\widetilde{S}|^2 \tag{3.24}$$

The constant C_I is calculated dynamically based on the smallest resolved scales (Moin *et al.*, 1991). The filtered pressure field is calculated as:

$$\widetilde{P} = \widetilde{P}^* - \frac{2}{3} k_{sgs} \tag{3.25}$$

where $\widetilde{P}^*$ is the modified filtered pressure normalized by the fluid density, which is given by the LES.

For both the *a priori* and *a posteriori* testing the SGS dissipation rate is calculated using the relationship from Gicquel *et al.* (2002):

$$\epsilon_{sgs} = C_\epsilon \frac{(k_{sgs})^{3/2}}{\Delta} \tag{3.26}$$

3.4.6 Model of Fukagata *et al.* (2004)

The implementation of the particle SGS model proposed by Fukagata *et al.* (2004) is very straightforward. The SGS Brownian force is calculated using equation (2.37):

$$\frac{F_{sgs,i}}{m_p} = \frac{\sigma_s}{\Delta t} \xi_i \tag{3.27}$$

The parameter σ_s is evaluated using equations (2.38) to (2.40), and the SGS Brownian force is then added to the right-hand side of the particle equation of motion. The Lagrangian timescale and turbulent kinetic energy are evaluated using the methods

described in the Sections 3.4.4 and 3.4.5.

It should be noted that Fukagata *et al.* used a different method to calculate $T^*_{L,sgs}$. They estimated $T^*_{L,sgs}$ using the inverse of the the resolved local vorticity magnitude. This quantity represents a timescale associated with the filtered fluid field, not the residual fluid field. Consequently, it was decided to use (3.22) instead of the method used by Fukagata *et al.*.

3.4.7 Model of Shotorban and Mashayek (2006)

The Langevin equation proposed by Shotorban and Mashayek (2006) for the seen fluid velocity, previously given in (2.43), is:

$$du_{s,i} = \left[-\frac{\partial \widetilde{P}}{\partial x_i} + \nu \frac{\partial^2 \widetilde{u_{f,i}}}{\partial x_j \partial x_j} - \frac{(u_{s,i} - \widetilde{u_{f,i}})}{T^*_{L,sgs}} \right] dt + \sqrt{C_0 \epsilon_{sgs}} dW_i \tag{3.28}$$

This equation is solved numerically using an explicit Euler-Maruyama scheme (Kloeden and Platen, 1992). The discretized version of (2.43) is

$$\begin{aligned}(u_{s,i})_n = (u_{s,i})_{n-1} + \Delta t \left[-\frac{\partial \widetilde{P}}{\partial x_i} + \nu \frac{\partial^2 \widetilde{u_{f,i}}}{\partial x_j \partial x_j} - \frac{(u_{s,i} - \widetilde{u_{f,i}})}{T^*_{L,sgs}} \right]_{n-1} \\ + \sqrt{C_0 (\epsilon_{sgs})_{n-1} \Delta t}\, \xi \end{aligned} \tag{3.29}$$

The subscripts n and $n-1$ denote the current and previous timesteps, respectively. The pressure and viscous terms are calculated by numerically differentiating the filtered flow field using a fourth order central difference scheme.

3.4.8 Model of Berrouk *et al.* (2007)

An explicit Euler-Maruyama scheme (Kloeden and Platen, 1992) is used to solve the Langevin equation included in the model of Berrouk *et al.* (2007):

$$du_{s,i} = \left[-\frac{\partial \widetilde{P}}{\partial x_i} + \nu \frac{\partial^2 \widetilde{u_{f,i}}}{\partial x_j \partial x_j} - \frac{(u_{s,i} - \widetilde{u_{f,i}})}{T_i^*} \right] dt + \sqrt{C_0^* \epsilon_{sgs}} dW_i \tag{3.30}$$

$$\begin{aligned}(u_{s,i})_n = (u_{s,i})_{n-1} + \Delta t \left[-\frac{\partial \widetilde{P}}{\partial x_i} + \nu \frac{\partial^2 \widetilde{u_{f,i}}}{\partial x_j \partial x_j} - \frac{(u_{s,i} - \widetilde{u_{f,i}})}{T_i^*} \right]_{n-1} \\ + \sqrt{(C_0^*)_{n-1} (\epsilon_{sgs})_{n-1} \Delta t}\, \xi\end{aligned} \tag{3.31}$$

The spatial derivatives are calculated using a fourth order central difference scheme. Equations (2.48) to (2.51) are used to evaluate the direction specific timescale. The modified model constant is calculated as

$$C_0^* = C_0 b_i + \frac{2}{3}\left(b_i - 1\right) \tag{3.32}$$

The term $\widehat{k}_{sgs}/k_{sgs}$ is neglected in (3.32) since this term accounts for anisotropy of the turbulence, but the current simulations are isotropic.

The value of β used is $\beta = 0.356$, which is the same value that was used by Berrouk *et al.* (2007). Different values of β are not tested, although the results of Berrouk *et al.* (2007) showed sensitivity to its value. The timescale $T_{E,sgs}$, which is required to calculate $\mathrm{St}_{E,sgs}$, is calculated using (2.49) and the prescribed value of β.

3.4.9 DNS pressure gradient

Analysis of the DNS output from OpenFOAM revealed that the pressure is written to disk incorrectly when running the code in parallel. However, it was confirmed that the code correctly handles the pressure in parallel since the velocity fields obtained when running the code in serial or parallel were identical. It is only the pressure output which is incorrect, the internal calculation is treated properly. Using the velocity field from the parallel simulation, the DNS pressure gradient was obtained by rearranging the Navier-Stokes equations:

$$\frac{\partial P}{\partial x_i} = -\frac{\partial u_{f,i}}{\partial t} - u_{f,j}\frac{\partial u_{f,i}}{\partial x_j} + \nu\frac{\partial^2 u_{f,i}}{\partial x_j \partial x_j} \tag{3.33}$$

The right-hand side of (3.33) was calculated by numerically differentiating the DNS velocity field. The time and spatial derivatives were computed using a second order and a fourth order central difference scheme, respectively. This method was validated by comparing the pressure gradient output from a serial run, with the pressure gradient calculated from the velocity field output of a parallel run. The pressure gradient fields from the two different methods were identical.

The gradient of the filtered pressure is required for the models of Shotorban and Mashayek (2006) and Berrouk *et al.* (2007). Filtering commutes with differentiation for uniform filter sizes (Pope, 2000), which is the case here. For the *a priori* testing, the gradient of the filtered pressure was obtained by explicitly filtering the pressure gradient calculated using (3.33):

$$\frac{\partial \widetilde{P}}{\partial x_i} = \widetilde{\left(\frac{\partial P}{\partial x_i}\right)} \tag{3.34}$$

No special treatment is required for the *a posteriori* testing since the LES is run in serial and the correct filtered pressure field is output. Therefore, the filtered pressure output can be spatially differentiated and the calculation of (3.33) is not required for the LES testing.

3.4.10 Model constants

The model constants C_0 and C_ϵ must be specified to close the three stochastic particle SGS models. Turbulence modeling using a Langevin equation was originally developed for RANS and was later applied to LES. Gicquel *et al.* (2002) were the first to apply the generalized Langevin model to LES. The Langevin model constant, C_0, relates the Lagrangian fluid SGS timescale to the turbulent kinetic energy and dissipation rate:

$$C_0 = \frac{4}{3}\left[\frac{1}{T_{L,sgs}}\frac{k_{sgs}}{\epsilon_{sgs}} - \frac{1}{2}\right] \tag{3.35}$$

The standard value of the Langevin model constant reported in the literature is $C_0 = 2.1$, and this value has been frequently used for stochastic particle SGS models. The value $C_0 = 2.1$ was determined by Anand and Pope (1985), who developed a probability density function equation for turbulent dispersion based on the Langevin equation. They applied this equation to a thermal wake and compared it with the experimental data of Warhaft (1984), for which they found $C_0 = 2.1$ to be the optimal value.

The constant C_0 is not expected to be universal, but instead should be a function of the turbulence, and in the case of LES a function of the filter size. The Langevin

model constant can be calculated directly from the DNS and FDNS as:

$$C_0(t) = \frac{4}{3}\left[\frac{1}{T_{L,sgs}(t)}\frac{\langle k_{sgs}(t)\rangle}{\langle \epsilon_{sgs}(t)\rangle} - \frac{1}{2}\right] \tag{3.36}$$

The difficulty with calculating C_0 in decaying turbulence is that the various parameters in (3.36) are a function of t, which would not be the case with forced turbulence. The Lagrangian fluid SGS timescale is found by integrating the Lagrangian autocorrelation coefficient of the SGS fluid velocity fluctuations along a fluid particle's path $R_{Lu''_{f@fp}}(t,\tau)$ (Fede and Simonin, 2006).

$$T_{L,sgs}(t) = \int_0^\infty R_{Lu''_{f@fp}}(t,\tau)d\tau \tag{3.37}$$

$$R_{Lu''_{f@fp,i}}(t,\tau) = \frac{\langle u''_{f@fp,i}(t)u''_{f@fp,i}(t+\tau)\rangle}{[\langle {u''_{f@fp,i}}^2(t)\rangle]^{1/2}[\langle {u''_{f@fp,i}}^2(t+\tau)\rangle]^{1/2}} \tag{3.38}$$

The value of C_0 for this simulation was found by calculating $T_{L,sgs}(t)$, $\langle k_{sgs}(t)\rangle$ and $\langle \epsilon_{sgs}(t)\rangle$ from the DNS and FDNS, and then using (3.36). The effect of decaying turbulence on $R_{Lu''_{f@fp}}(t,\tau)$ was not accounted for. The calculated C_0 values as a function of time and filter size are plotted in Figure 3.13. The results show a large range for C_0, but the data is roughly centered around the standard value of $C_0 = 2.1$.

Several authors have noted that the formulation of the Langevin model is consistent with the Kolmogorov hypothesis, and that the Langevin model constant C_0 is consistent with the Kolmogorov constant (Pope, 2000). The Kolmogorov hypothesis predicts

$$D_{Lu''_{f@fp}}(t,\tau) = C_0\langle \epsilon_{sgs}\rangle\tau \quad \text{for} \quad \tau_K << t << T_{L,f} \tag{3.39}$$

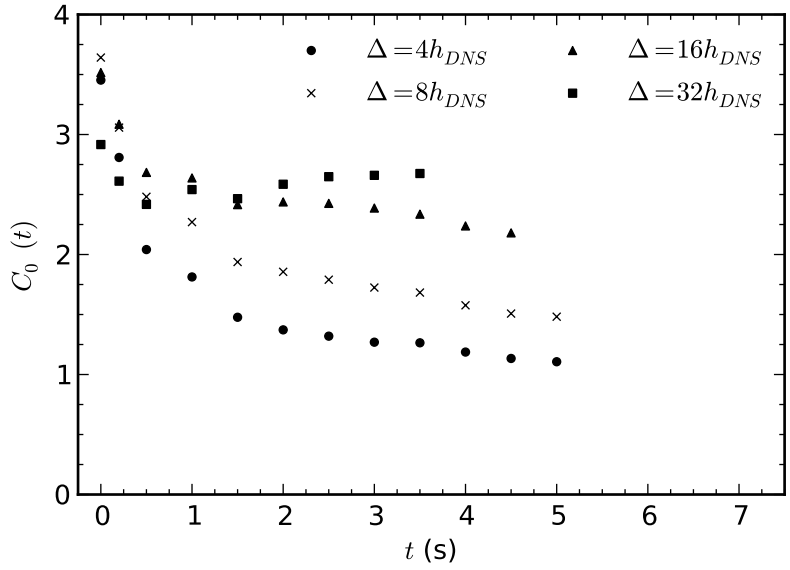

Figure 3.13: Model constant C_0 calculated from the DNS and FDNS velocity fields using equation (3.36).

where $D_{Lu''_{f@fp}}(t,\tau)$ is the Lagrangian structure function which is defined as

$$D_{Lu''_{f@fp}}(t,\tau) = \left\langle \left[u''_{f@fp,i}(t+\tau) - u''_{f@fp,i}(t) \right]^2 \right\rangle \tag{3.40}$$

Pope (2000) explains that although the formulations are consistent with one another, the two constants are not necessarily equivalent. The two constants would be expected to be identical for high Reynolds number turbulence with a very well defined inertial subrange, which has not been tested experimentally or with DNS. Low Reynolds number experiments have shown discrepancies between the two constants.

As a comparison, the constant C_0 was also calculated from the DNS and FDNS using the Lagrangian structure function method. Least squares linear regression was used to determine C_0 from (3.39) and (3.40). Figure 3.14 shows that this method leads to a larger range of C_0 with somewhat smaller values, although the standard

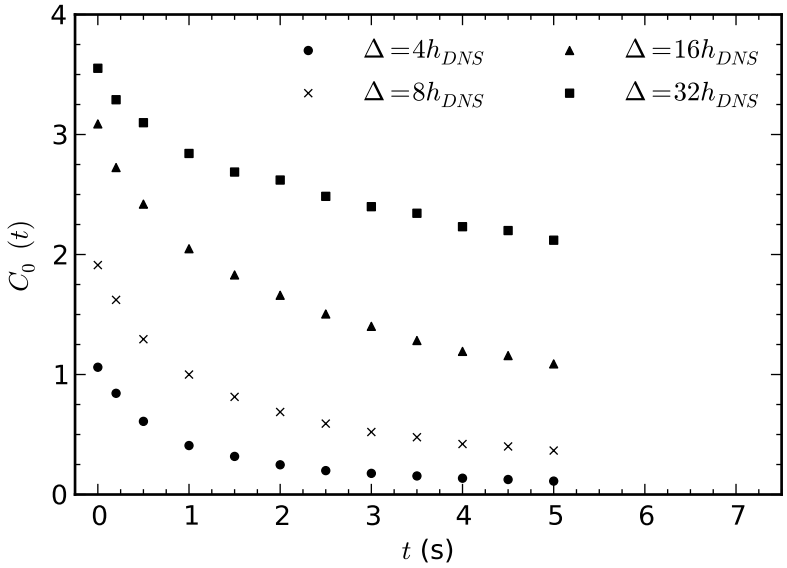

Figure 3.14: Model constant C_0 calculated from the DNS and FDNS velocity fields using the Lagrangian structure function.

value $C_0 = 2.1$ is still within the range of results.

The constant C_ϵ is the LES dissipation coefficient and has no relation to RANS. It relates the SGS dissipation rate to the SGS turbulent kinetic energy:

$$C_\epsilon = \frac{\epsilon_{sgs}\Delta}{(k_{sgs})^{3/2}} \tag{3.41}$$

The LES dissipation coefficient has been used in the past for modeling of atmospheric flows with LES (Deardorff, 1973), and more recently has been used in LES Langevin modeling Gicquel *et al.* (2002). The standard value that has been adopted for SGS particle modeling is $C_\epsilon = 1.0$. Using the DNS and FDNS, C_ϵ can be calculated directly as:

$$C_\epsilon(t) = \frac{\big\langle \epsilon_{sgs}(t) \big\rangle \Delta}{\big[\big\langle k_{sgs}(t) \big\rangle\big]^{3/2}} \tag{3.42}$$

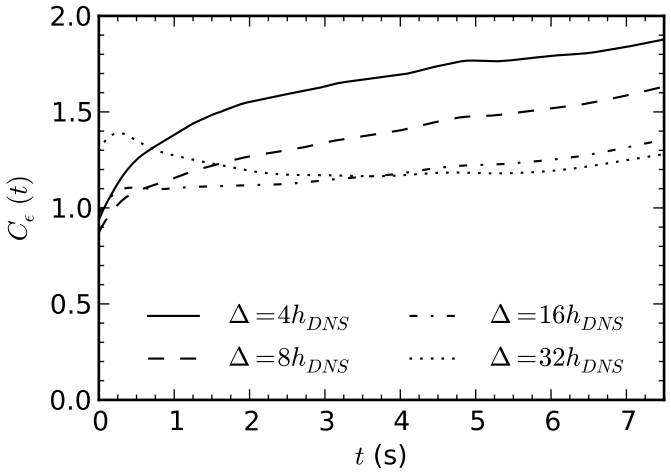

Figure 3.15: Model constant C_ϵ calculated from the DNS and FDNS velocity fields using equation (3.42).

The calculated C_ϵ values are shown in Figure 3.15. The large majority of calculated values are greater than the standard value of $C_\epsilon = 1.0$.

In this thesis, various values of model constants C_0 and C_ϵ are used to test the sensitivity and influence of the constants on the stochastic particle SGS models. Based on the values calculated from the DNS and FDNS (Figures 3.13 and 3.15), low, medium and high values were selected for each of the constants, with the standard values included. The values selected were $C_0 = 1.0, 2.1, 3.2$ and $C_\epsilon = 1.0, 1.4, 1.8$. Table 3.4 lists the different combinations of model constants that were selected for testing.

C_0	1.0	2.1^*	2.1	2.1	3.2
C_ϵ	1.4	1.0^*	1.4	1.8	1.4

Table 3.4: Combinations of model constants C_0 and C_ϵ selected for testing. Superscript * denotes standard constant values.

Chapter 4

Results and Discussion

This chapter presents the results of the *a priori* and *a posteriori* tests for assessment of the particle SGS models. The particle SGS models that are tested are ADM, the stochastic models of Fukagata *et al.* (2004), Shotorban and Mashayek (2006) and Berrouk *et al.* (2007), and the case of no model (tracking particles in the FDNS or LES flow fields without any particle SGS modeling). The model results are compared to particle statistics obtained by tracking particles in the DNS flow field.

The majority of the results focus on the *a priori* testing. The first results presented are for a single filter size of $\Delta = 16h_{DNS}$ with the standard model constants ($C_0 = 2.1$ and $C_\epsilon = 1.0$), which are referred to as the standard tests in this thesis, with both gravity neglected and included. Next, *a priori* results analysing the significance of filter size and model constant values are included. Lastly, the *a posteriori* results are examined.

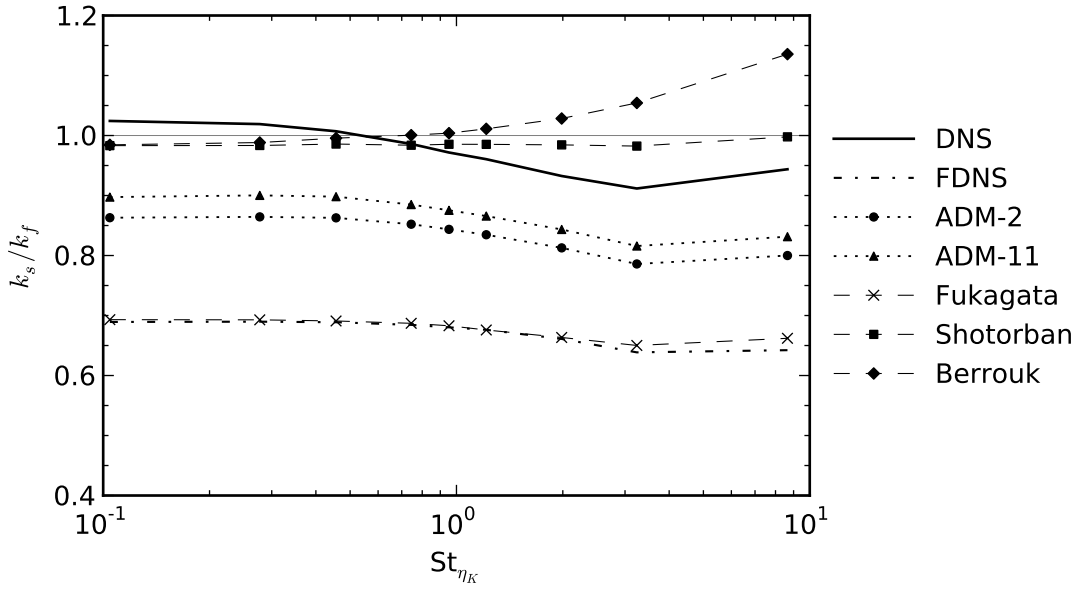

Figure 4.1: Turbulent kinetic energy of the fluid seen by the particles at time $t = 4.0\,\mathrm{s}$. *A priori* testing with filter size $\Delta = 16h_{DNS}$, standard model constants, and zero gravity.

4.1 *A priori*

4.1.1 Standard tests with zero gravity

This section contains the results of the *a priori* analysis with standard test parameters ($\Delta = 16h_{DNS}$, $C_0 = 2.1$ and $C_\epsilon = 1.0$) and zero gravity. The turbulent kinetic energy (TKE) at time $t = 4.0\,\mathrm{s}$ of the fluid seen by the particles and of the particles themselves are shown in Figures 4.1 and 4.2, respectively. Both plots are normalized by the TKE of the fluid, and are plotted as a function of Stokes number based on the Kolmogorov timescale at the current time. The TKE plots are only shown at a single time since the conclusions regarding the ability of the particle SGS models to predict TKE were found to be independent of time.

The DNS results of the TKE of the fluid seen by the particles shows a dependence

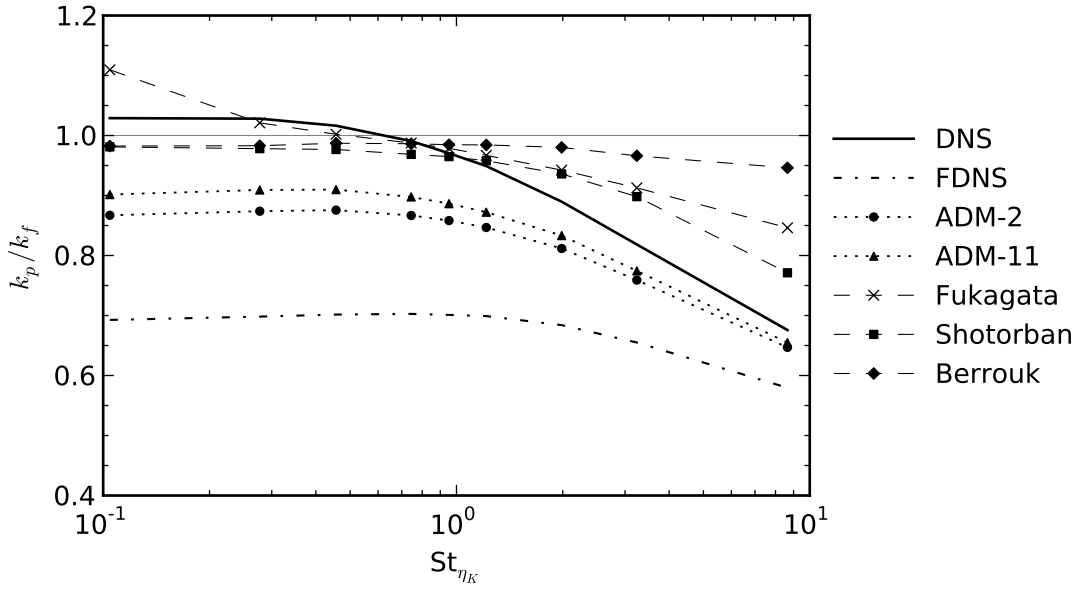

Figure 4.2: Turbulent kinetic energy of the particles at time $t = 4.0\,\mathrm{s}$. *A priori* testing with filter size $\Delta = 16h_{DNS}$, standard model constants, and zero gravity.

on Stokes number. This is due to particle clustering, which causes inertial particles to have spatial distributions that differ from fluid particles. The shape of the seen fluid TKE DNS results as a function of Stokes number agree well with the DNS results of Gobert and Manhart (2010). The seen TKE of the DNS fluid particles is equal to the fluid TKE ($k_s/k_f \sim 1.0$), as previously shown in Section 3.3.6.

The k_s and k_p results from the FDNS simulations are much less than the DNS since filtering removes the fluid subgrid scale TKE. The discrepancy between the FDNS and DNS particle TKE results is reduced at larger Stokes numbers since large inertia particles are not significantly affected by small turbulent scales.

The TKE results from ADM are superior to FNDS but are still smaller than the DNS. This is expected since ADM is only capable of improving scales near the cut-off, and cannot recover energy associated with scales that are smaller than the LES grid. The ADM results using truncation levels $m = 2$ and $m = 11$ are denoted by ADM-2

and ADM-11, respectively, in the plot legends. The ADM results with truncation level $m = 11$ are superior to $m = 2$, but the discrepancy between the two is fairly small. These ADM results are representative of the general trend that will be observed for most of the *a priori* results in this work; ADM is superior to FDNS but is unable to match the DNS, and the ADM-11 results are slightly better than the ADM-2 results.

The seen TKE from the stochastic model of Fukagata *et al.* (2004) is almost identical to the FNDS. In the model of Fukagata *et al.* (2004) the particles see the filtered fluid velocity, so any discrepancy with the FNDS for the seen TKE is due to differences in particle distributions. Figure 4.2 shows that the k_p results from the model proposed by Fukagata *et al.* have good agreement with the DNS for intermediate sized particles, but too much energy is added for the smallest and largest particles. The excess energy for the smallest particles is due to the particle SGS force becoming very large as $\tau_p \to \infty$, which can be seen by analysing equations (2.38) to (2.40). It is not clear why k_p is overpredicted for the large particles.

The model of Shotorban and Mashayek (2006) predicts that the TKE of the fluid seen by the particles is relatively constant for different Stokes numbers with a value of $k_s/k_f \sim 1.0$. The independence of k_s with respect to Stokes number is a result of the SGS kinetic energy being calculated directly from the DNS, the timescale calculations being independent of particle size (fluid particle assumptions), and zero particle clustering (which will be shown later). All of these factors imply that the TKE of the seen fluid velocity should not be dependent on the particle relaxation time. Using the model proposed by Shotorban and Mashayek the particle TKE is well predicted for small and intermediate sized particles, but is overpredicted for large particles. This result has been observed previously by Shotorban and Mashayek

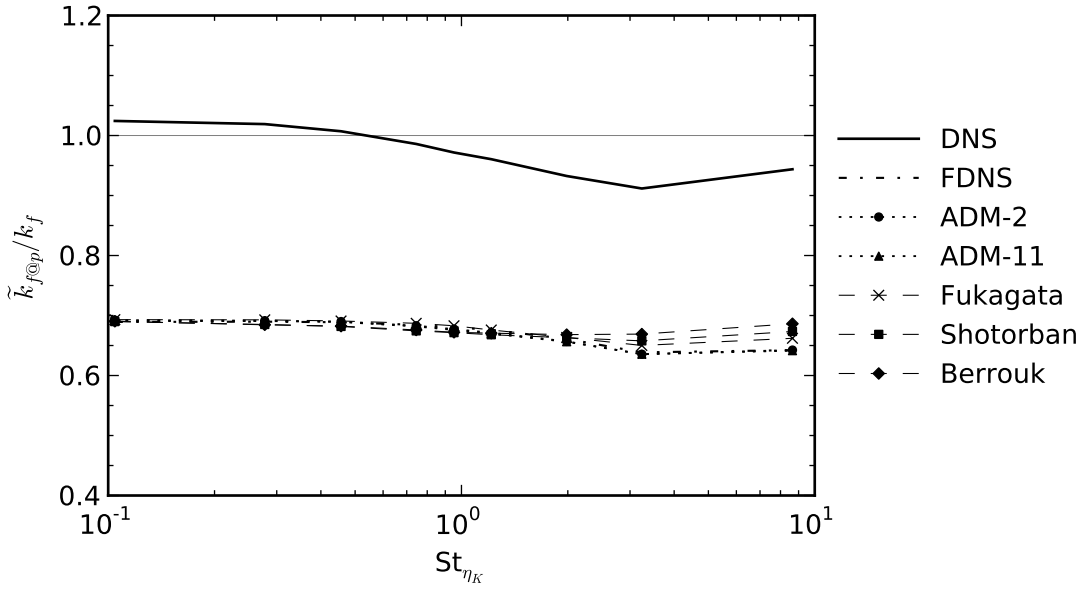

Figure 4.3: Turbulent kinetic energy of the filtered fluid velocity at the particles' position at time $t = 4.0\,\mathrm{s}$. *A priori* testing with filter size $\Delta = 16h_{DNS}$, standard model constants, and zero gravity.

(2006). The error for the large particles can likely be attributed to the fluid particle timescale assumptions.

When gravity is neglected the only difference between the stochastic models of Shotorban and Mashayek (2006) and Berrouk *et al.* (2007) is the timescale correction to account for particle inertia, given in (2.48). Therefore, in this case of zero gravity the results for the smallest particles using the two models should be identical, which is shown to be true in Figures 4.1 and 4.2. Far too much energy is added for the large particles when using the model of Berrouk *et al.* (2007), which indicates that the particle inertia correction actually worsens particle results. As discussed in Sections 2.3.4 and 2.3.6, the value of constant β has been shown to have a significant influence on model results, and a wide range of values have been reported in the literature. It is possible that an optimal value of β could improve TKE results and lead to a superior

prediction of TKE compared to the model of Shotorban and Mashayek (2006).

The TKE of the filtered fluid velocity at the particles' position is shown in Figure 4.3. As expected, the results from the different models all collapse to the FDNS result. The small discrepancies are due to differences in particle distributions, which will be discussed later.

The Lagrangian autocorrelation coefficient functions of the seen fluid velocity along a particle's path $R_{Lu_s,3}(t_0, \tau)$ and of the particle velocity $R_{Lp,3}(t_0, \tau)$ for various particle types are shown in Figures 4.4 and 4.5, respectively. Only the autocorrelation functions in the direction x_3 are presented since the turbulence is isotropic and therefore the autocorrelation functions in the three principal directions are nearly identical.

The autocorrelation coefficients R_{Lu_s} and R_{Lp} from the FDNS are much greater than the DNS for all particle types. Consequently, the particles in the FDNS simulations have larger Lagrangian particle integral timescales. This result is expected since filtering removes the smallest turbulent velocity fluctuations which contribute to fluid and particle velocities becoming uncorrelated in time.

The autocorrelation coefficients from ADM are between the FDNS and DNS functions for all particle types, with ADM-11 being slightly better than ADM-2.

The model of Fukagata *et al.* (2004) produces Lagrangian particle velocity autocorrelations that decrease very quickly at early times. This can be attributed to the particle SGS force which causes particle velocities to change very quickly due to the random component. However, this sharp drop at early times does not occur for R_{Lu_s} when using the model of Fukagata *et al.* (2004). Although the particle velocity changes abruptly, the particles do not travel far in such short times. Thus, the local

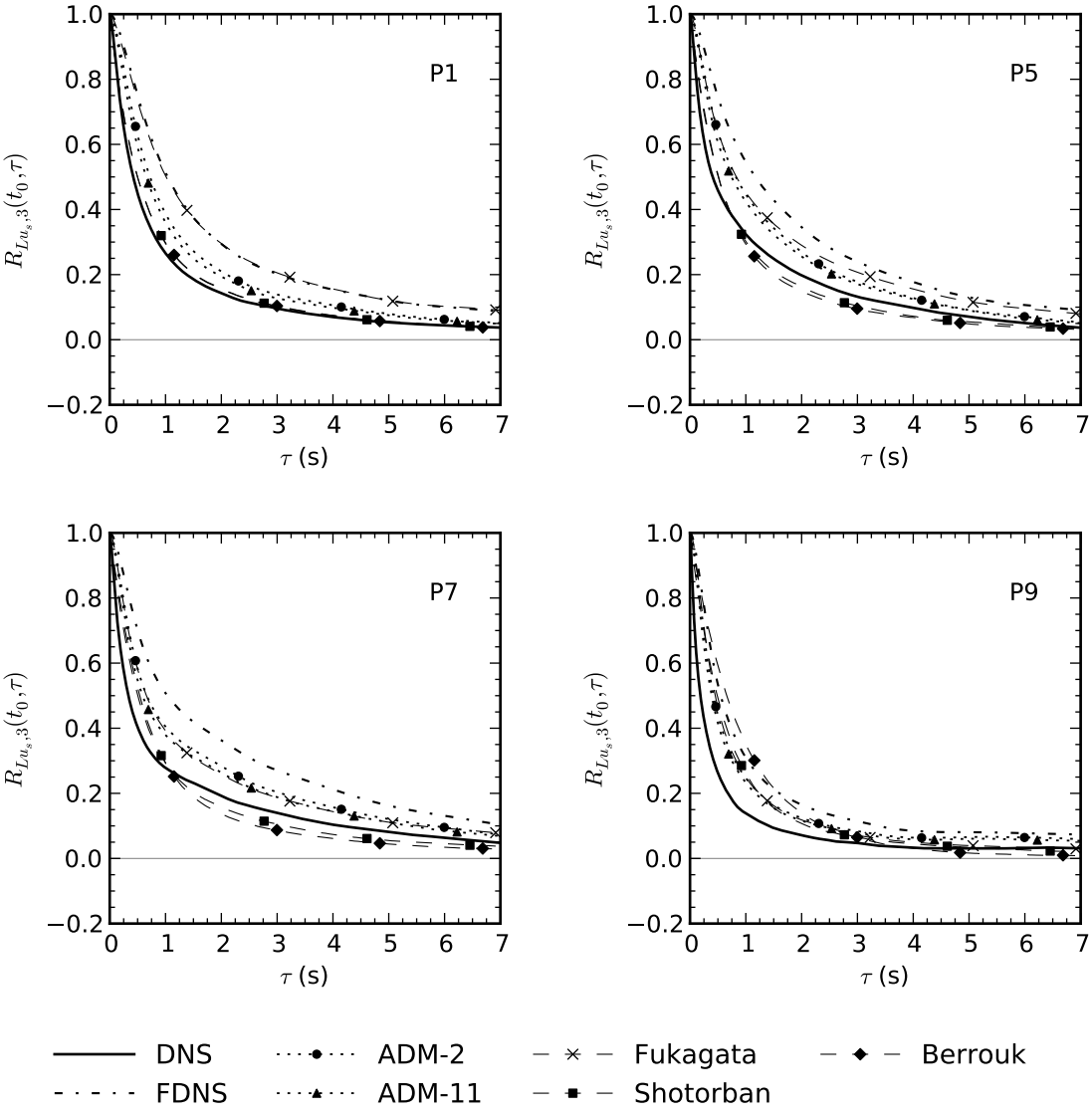

Figure 4.4: Lagrangian autocorrelation coefficient function of seen fluid velocity in direction x_3 along a particle's path, for various particle types with initial time $t = t_0$. *A priori* testing with filter size $\Delta = 16h_{DNS}$, standard model constants, and zero gravity.

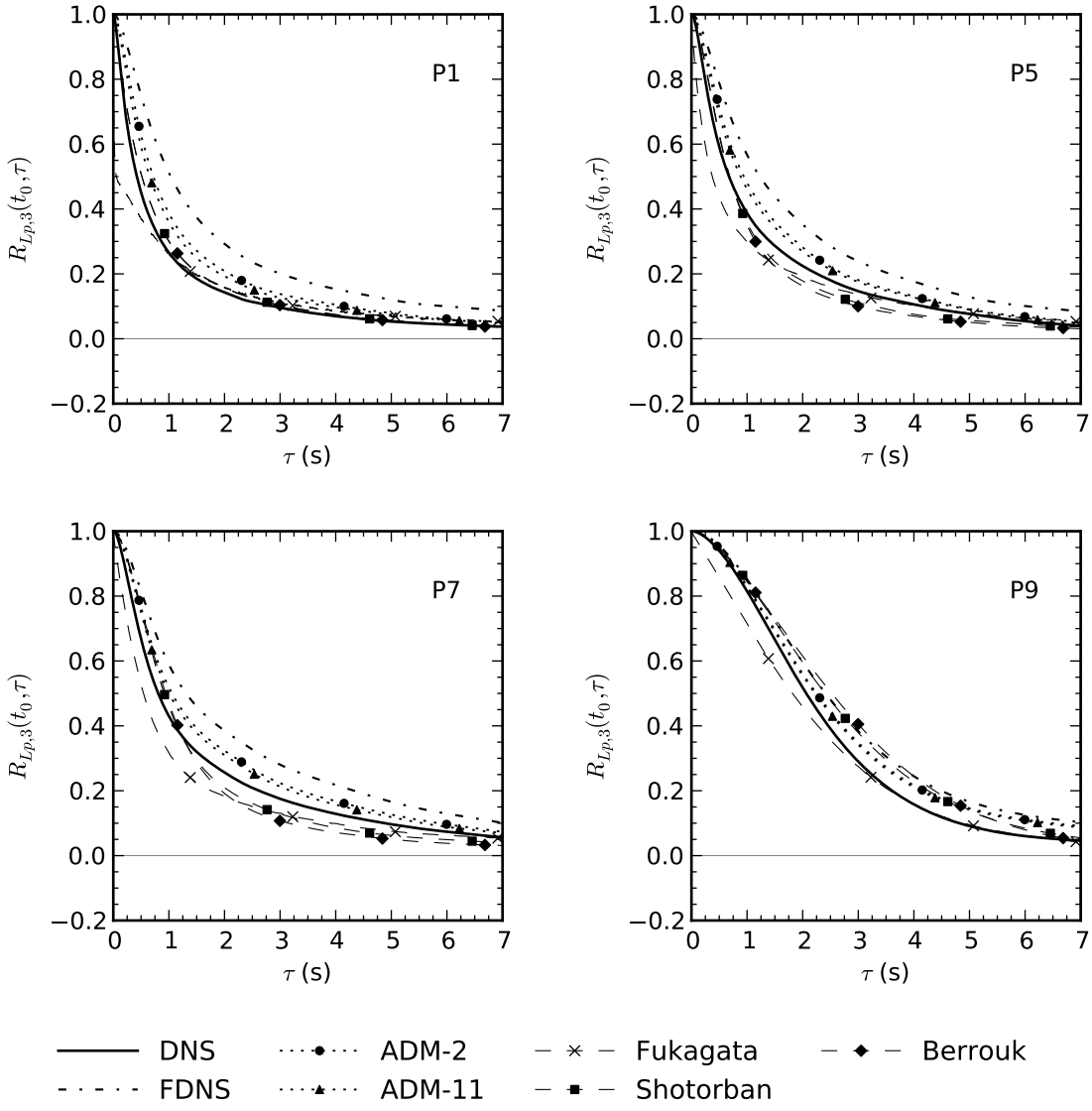

Figure 4.5: Lagrangian autocorrelation coefficient function of particle velocity in direction x_3, for various particle types with initial time $t = t_0$. *A priori* testing with filter size $\Delta = 16h_{DNS}$, standard model constants, and zero gravity.

filtered fluid velocity does not change rapidly. For the smallest particles the R_{Lu_s} results are almost identical to the DNS, and as Stokes number increases the R_{Lu_s} function moves towards the DNS.

For small particles the autocorrelation coefficients R_{Lu_s} and R_{Lp} predicted from the models of Shotorban and Mashayek (2006) and Berrouk *et al.* (2007) are in close agreement with the DNS, which is consistent with the findings of Shotorban and Mashayek (2006). As the Stokes number is increased the two stochastic models tend to overpredict the autocorrelation functions at early times and underpredict at later times. For large particles the results of Shotorban and Mashayek (2006) are superior to Berrouk *et al.* (2007), which again shows that the particle inertia correction does not necessarily improve model performance.

Shown in Figures 4.6 to 4.8 are the particle mean square dispersion and rate of dispersion results for the standard tests without gravity. The work of Taylor (1921) tells us that the rate of particle dispersion is dependent on the product of particle TKE and the particle Lagrangian integral timescale, as shown in equation (2.27). Therefore, the particle dispersion results can be explained using the previously analyzed particle TKE and particle velocity Lagrangian autocorrelation function results.

The previous DNS results showed that as Stokes number was increased, k_p decreased and R_{Lp} increased. These two trends have opposing influences on dispersion, and therefore the DNS particle dispersion results do not monotonically increase or decrease with Stokes number. The shape of the DNS particle dispersion results as a function of Stokes number agree well with the DNS results of Gobert and Manhart (2010). As a comparison, the DNS results yield fluid particle dispersion of $\left\langle x_{p,3}^2 \right\rangle = 0.0499\,\mathrm{m}^2$ at time $t = 4.0\,\mathrm{s}$.

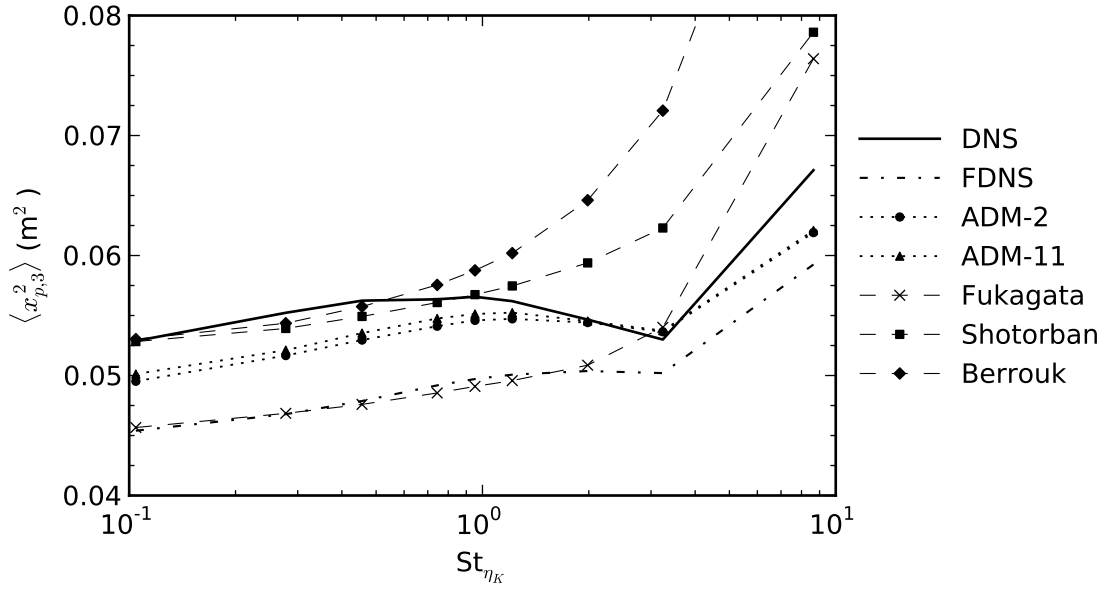

Figure 4.6: Particle mean square dispersion in direction x_3 at time $t = 4.0\,\mathrm{s}$. *A priori* testing with filter size $\Delta = 16h_{DNS}$, standard model constants, and zero gravity.

The previous FDNS results showed a decrease in k_p and an increase in R_{Lp} relative to the DNS. Based on this, it is not obvious if the FDNS particle dispersion should be less than or greater than that of the DNS. The particle dispersion and turbulent diffusivity plots in Figures 4.6 to 4.8 reveal that filtering causes a reduction in particle dispersion, which is consistent with the results of all previous particle LES studies. This implies that for the FDNS the reduction in particle TKE is more significant than the increase in the particle Lagrangian integral timescale.

The ADM particle dispersion results are generally between the FDNS and DNS results, as expected. This behaviour for particle dispersion using ADM was also found by Gobert and Manhart (2010).

The model of Fukagata *et al.* (2004) tends to underpredict dispersion for small particles due to the smaller particle Lagrangian integral timescale, and for large particles dispersion is overpredicted due to the large particle TKE. Overall, particle dispersion

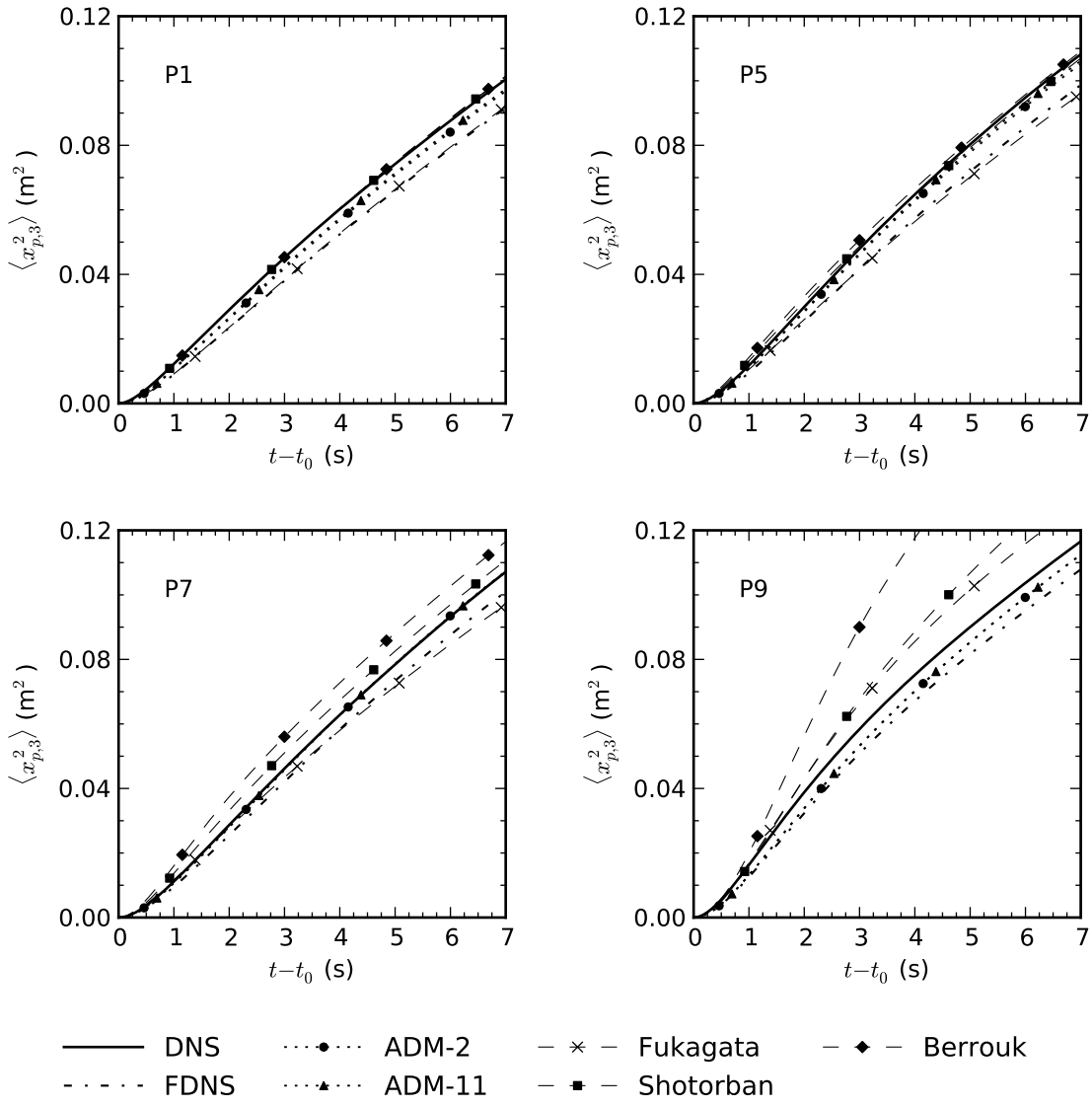

Figure 4.7: Time development of particle mean square dispersion in direction x_3 for various particle types. *A priori* testing with filter size $\Delta = 16h_{DNS}$, standard model constants, and zero gravity.

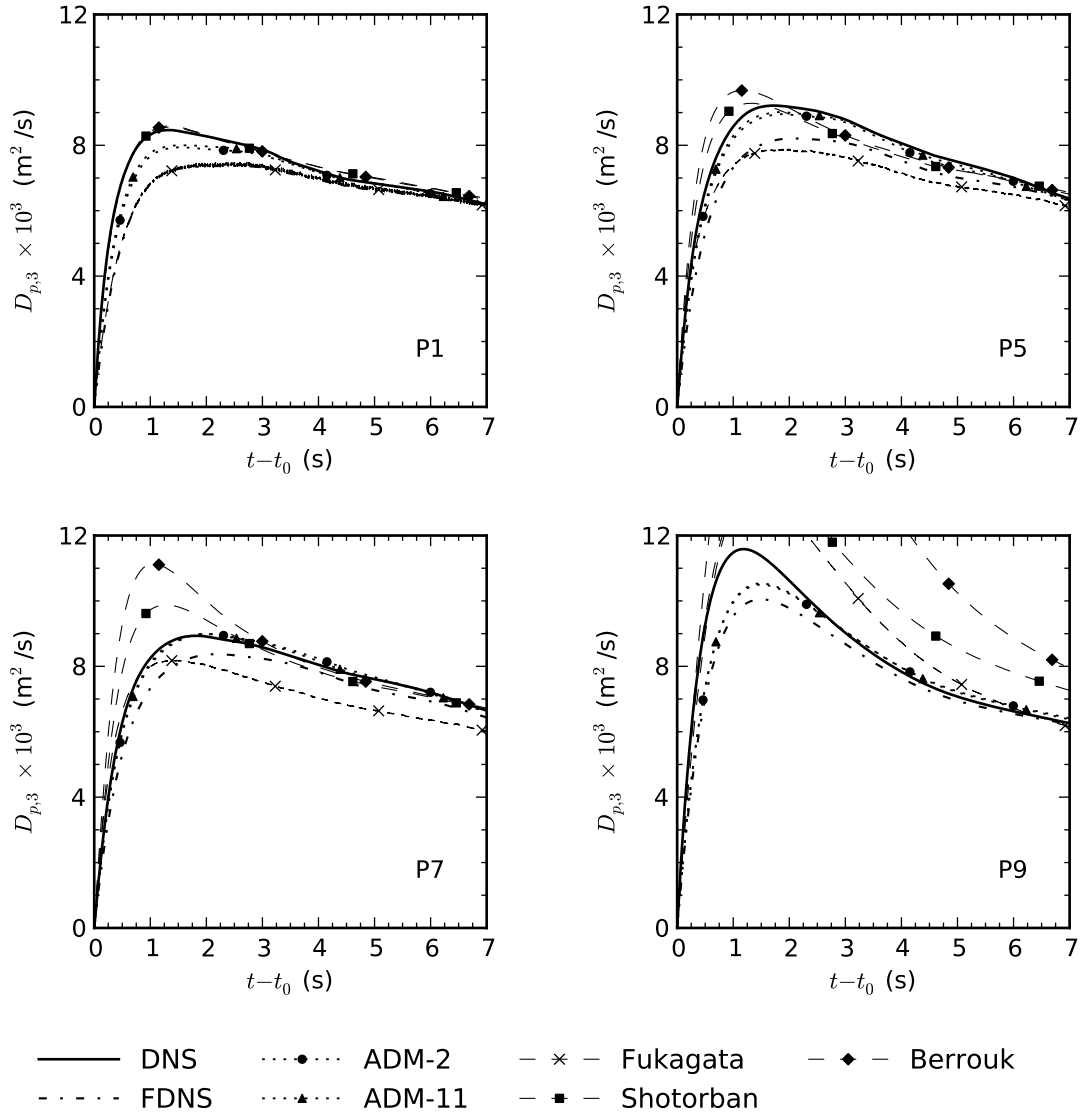

Figure 4.8: Time development of particle turbulent diffusivity in direction x_3 for various particle types. *A priori* testing with filter size $\Delta = 16h_{DNS}$, standard model constants, and zero gravity.

and rate of dispersion statistics obtained using the model of Fukagata *et al.* (2004) are generally inferior to the FDNS.

The small particle dispersion and rates of dispersion predicted using the stochastic models of Shotorban and Mashayek (2006) and Berrouk *et al.* (2007) have very good agreement with the DNS results. This was also observed by Shotorban and Mashayek (2006), but is in disagreement with Gobert and Manhart (2010) who found small particle dispersion to be underpredicted using the model proposed by Shotorban and Mashayek (2006). Model constant values, which will be examined in Section 4.1.4, may be the cause of this discrepancy. Due to the excess particle TKE for the large particles, both of the Langevin based stochastic models overpredict large particle dispersion and dispersion rates. This also agrees with the findings of Shotorban and Mashayek (2006).

The ability of the particle SGS models to predict preferential concentration is determined by analysing the fractal dimension and radial distribution function (RDF) results, which are plotted in Figures 4.9 and 4.10, respectively. The RDF results are plotted as a function of Stokes number at specific separation distances r_i.

Preferential concentration should be most significant for intermediate sized particles, and this can be seen in the DNS results as the fractal dimension is reduced for Stokes numbers of approximately unity. Fractal dimension values less than three ($d_{pc} < 3$) are caused by particle clustering, and a fractal dimension equal to three ($d_{pc} = 3$) represents a random distribution without any preferential concentration. The DNS results exhibit zero particle clustering for the smallest and largest particles since $d_{pc} = 3$ as $\mathrm{St}_{\eta_K} \to 0$ or $\mathrm{St}_{\eta_K} \to \infty$.

Figures 4.9 and 4.10 show that the FDNS simulations are able to partially predict

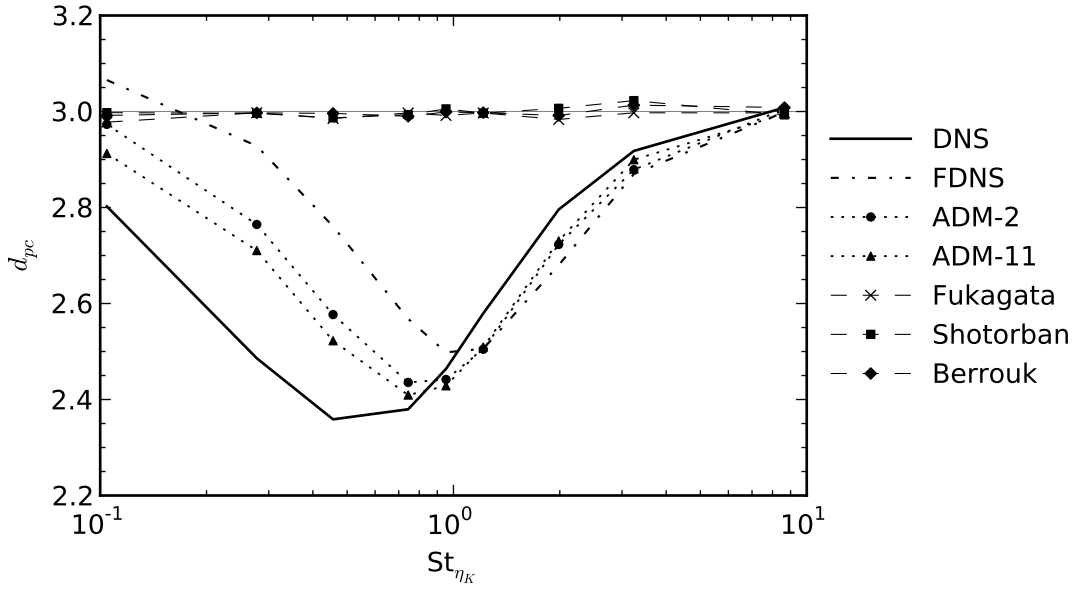

Figure 4.9: Fractal dimension at time $t = 4.0\,\mathrm{s}$. *A priori* testing with filter size $\Delta = 16h_{DNS}$, standard model constants, and zero gravity.

preferential concentration. The FDNS results show that filtering reduces particle clustering at low Stokes numbers, and increases particle clustering at high Stokes numbers. This agrees with the findings of Ray and Collins (2011), who also gave an explanation for this phenomenon which was reviewed in Section 2.3.6. Another notable result of the FDNS simulations is that filtering causes an increase in the Stokes number at which maximum particle clustering occurs (fractal dimension and RDF curves are shifted to the right). The reason for this is that the smallest turbulent vortices which drive preferential concentration in the DNS are removed by filtering. In the FDNS simulations preferential concentration is driven by the vortices at the cut-off scale, which have a larger timescale and therefore correspond to particles with larger particle relaxation times. Particle clustering in FDNS should be most significant for particles with an effective Stokes number of approximately unity, where the effective Stokes number is based on the cut-off timescale.

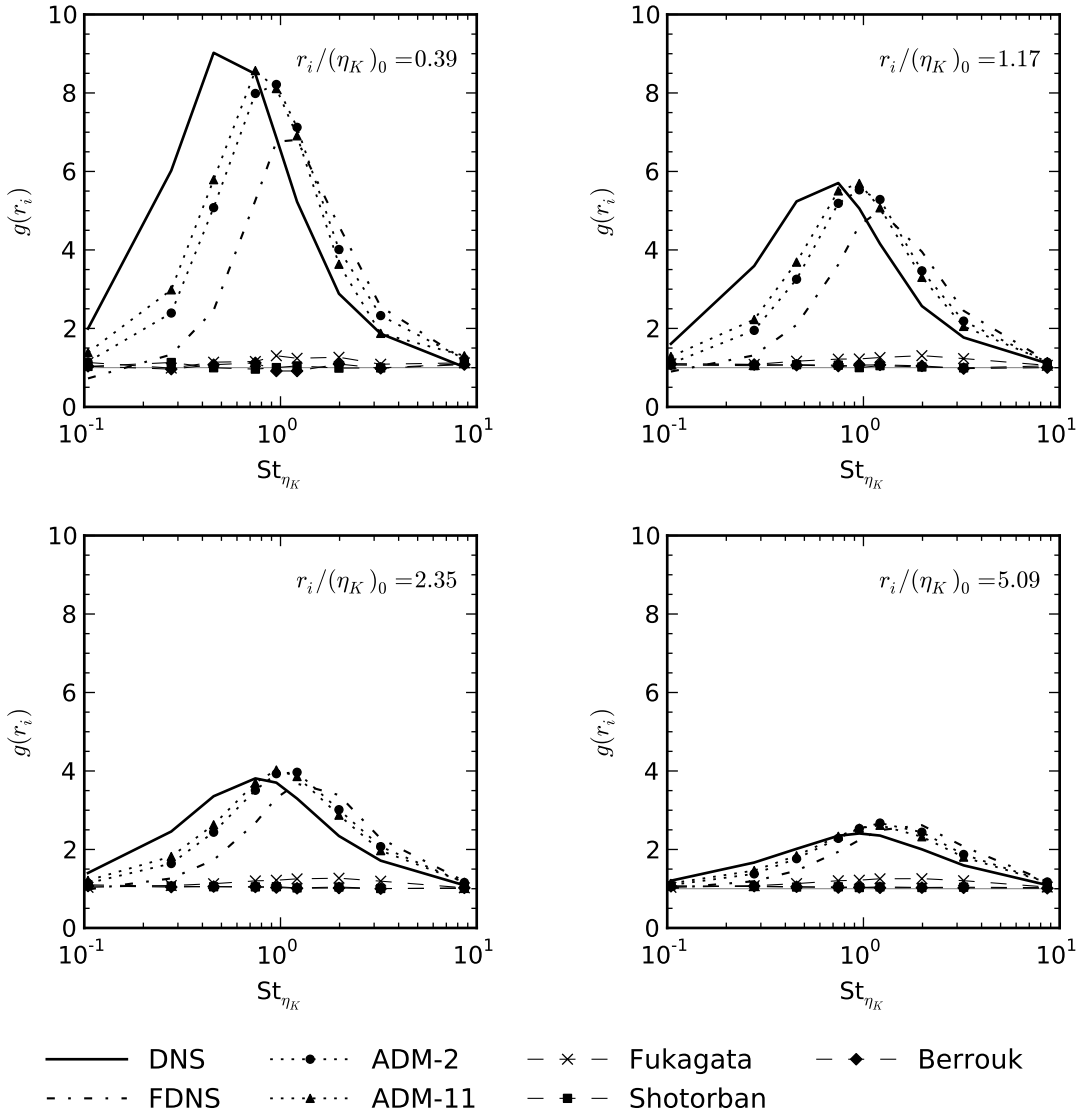

Figure 4.10: RDF for various separation distances at time $t = 4.0\,\mathrm{s}$. *A priori* testing with filter size $\Delta = 16h_{DNS}$, standard model constants, and zero gravity. The variable $(\eta_K)_0$ is the Kolmorov length scale at time t_0.

The idea of ADM is to enhance the smallest resolved scales, which would be expected to improve preferential concentration statistics. The particle clustering results show that ADM improves predictions of preferential concentration compared to FDNS, but is unable to match the DNS results.

All three of the stochastic particle SGS models predict zero particle clustering for all Stokes numbers. This uniform particle distribution is caused by the random component in each of the stochastic models, which evidently has a much more significant influence on particle distributions than do the resolved turbulent structures. The preferential concentration results from the stochastic models are inferior to the FDNS since the random component smooths particle distributions. One of the main motivations for performing particle-laden LES is that it is possible to account for the interaction between particles and turbulent structures. Unfortunately, stochastic particle SGS models have the potential to prevent particle-turbulent interactions from being properly captured due to their tendency to smooth particle distributions.

The RDF results plotted in Figure 4.10 show that the Stokes number at which the RDF is maximum increases with separation distance. This result was previously reported by Ray and Collins (2011), who postulated that at larger separation distances particle clustering is driven by larger vortices that "resonate" with higher Stokes number particles. All other conclusions from the RDF regarding the particle SGS models and preferential concentration are the same as from the fractal dimension results.

4.1.2 Standard tests including gravity

The *a priori* tests with standard conditions and gravity included are analyzed in this section. The gravitational constant for each particle type was selected such that the drift velocity is $u_d = 0.1\,\mathrm{m/s}$ for all particle types. The main purpose of the gravity simulations is to study the ability of the particle SGS models to account for the crossing trajectory and continuity effects. Without particle SGS modeling these effects are partially captured in particle-laden LES since the large turbulent eddies are resolved. However, particle SGS modeling is required to account for the crossing trajectory and continuity effects associated with the subgrid scale turbulent structures. It is important to note that for decaying turbulence the significance of the crossing trajectory and continuity effects increases with time since the drift velocity remains constant as the turbulence decays, as shown in Figure 3.7.

The FDNS and ADM results compared to the DNS results have very similar behaviour for both the gravity and zero gravity simulations. The trends from the FDNS gravity simulations are the same as those in the zero gravity case, such as FNDS dispersion is less than DNS. Once again, the ADM results are always between DNS and FDNS, with ADM-11 being slightly superior to ADM-2. However, the results of the stochastic particle SGS models do exhibit some different behaviour in the presence of gravity, and therefore the majority of the discussion in this section is focused on these models. Particular interest is paid to the comparison between the models of Shotorban and Mashayek (2006) and Berrouk *et al.* (2007). In the zero gravity case the only difference between these two models is the particle inertia correction, but in the presence of a mean drift velocity the model of Berrouk *et al.* (2007) also accounts for the crossing trajectory and continuity effects.

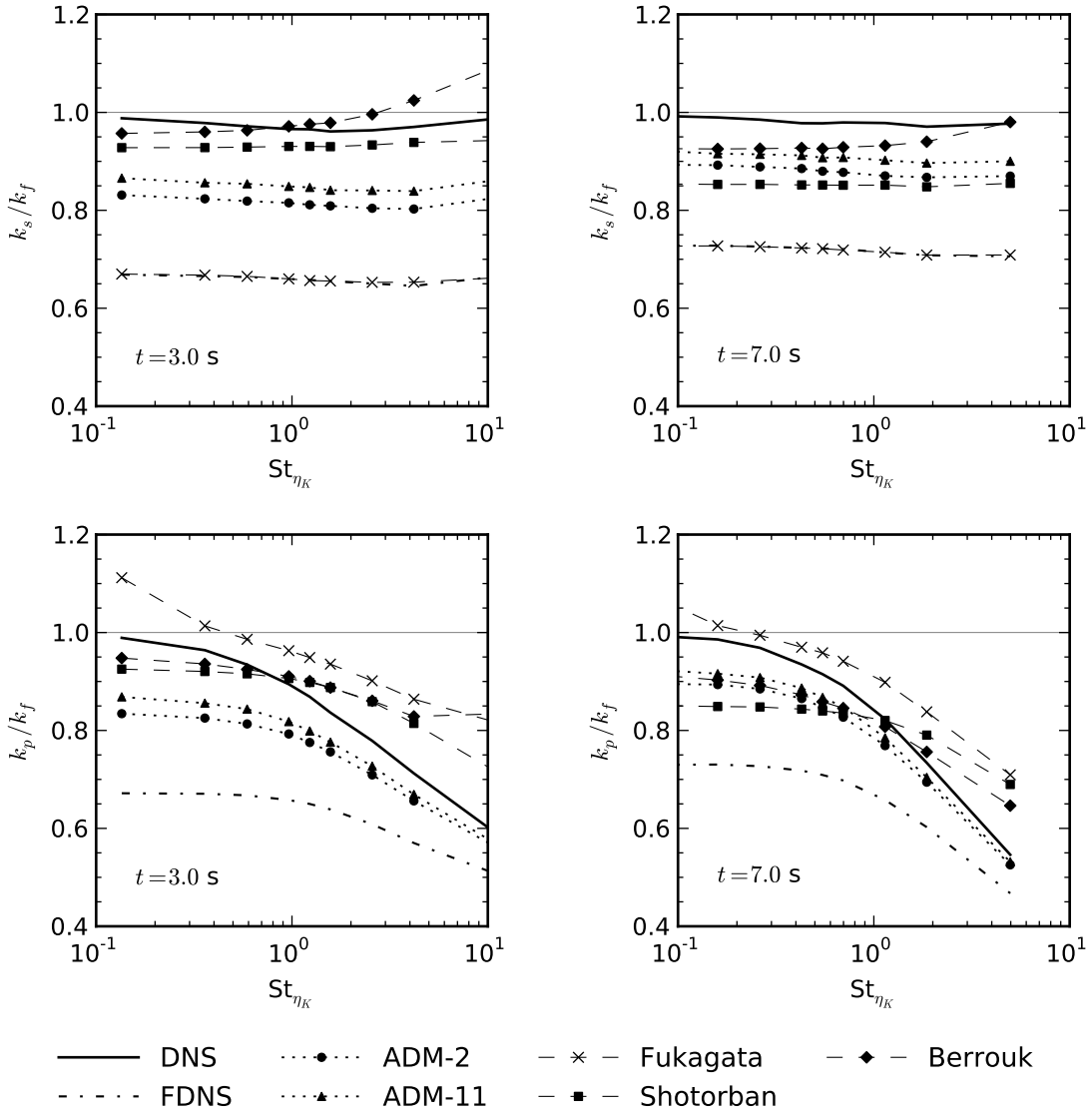

Figure 4.11: Particle and seen fluid turbulent kinetic energy at early and late times. *A priori* testing with filter size $\Delta = 16h_{DNS}$, standard model constants, and drift velocity $u_d = 0.1\,\mathrm{m/s}$.

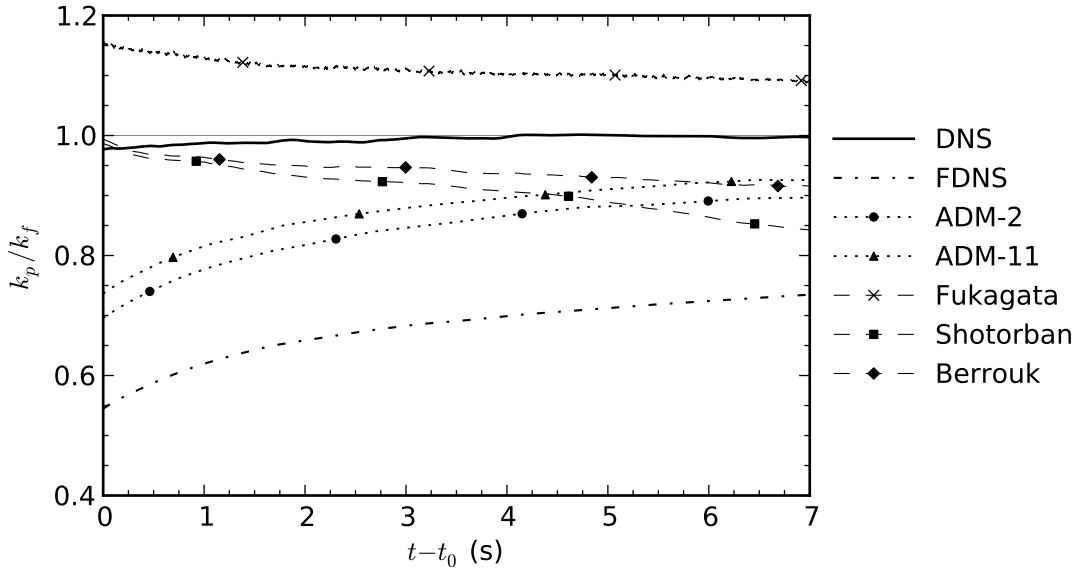

Figure 4.12: Time development of particle turbulent kinetic energy for particle type P1. *A priori* testing with filter size $\Delta = 16h_{DNS}$, standard model constants, and drift velocity $u_d = 0.1\,\mathrm{m/s}$.

The TKE results are presented in Figures 4.11 and 4.12. Figure 4.11 shows k_s and k_p at both early and late times so that the performance of the models with different values of the parameter $u_d/u'_{f,rms}$ can be examined. Compared to the zero gravity case, the DNS results for the seen TKE are less dependent on Stokes number due to less particle clustering, and the particle TKE is reduced.

The TKE of the particles predicted by the model of Fukagata *et al.* (2004) is largely unchanged from the zero gravity case, particularly for the small particles. Consequently, the particle TKE is overpredicted since the DNS particle TKE is reduced due to gravity. The SGS Brownian force is unaffected by gravity, and since it is this force that is dominant for the smaller particles their TKE is unchanged in the presence of gravity.

The particle TKE predicted by the model proposed by Shotorban and Mashayek

(2006) compared to the DNS is fairly similar to the zero gravity results. Conversely, the model of Berrouk *et al.* (2007) exhibits some significant improvements as a result of the corrections for crossing trajectory and continuity effects. For small particles the k_p results using the model of Berrouk *et al.* (2007) are superior to the model of Shotorban and Mashayek (2006) at all times. As shown in Figure 4.11, k_p for large particles from the model of Berrouk *et al.* (2007) is inferior to the model of Shotorban and Mashayek (2006) at early times, but the opposite is true at later times. At early times the particle inertia correction is the main source of error, but at later times the crossing trajectory and continuity effects are more significant significant and have a larger influence than the particle inertia correction. Figure 4.12 shows the time development of the particle TKE for particle type P1, which allows for the crossing trajectory and continuity effects to be examined without the problematic particle inertia correction since P1 has very small inertia. The plot clearly demonstrates the superiority of the model of Berrouk *et al.* (2007) for flows including gravity since the results improve relative to the model of Shotorban and Mashayek (2006) as the crossing trajectory and continuity effects become more significant.

The Lagrangian autocorrelation function results are shown in Figures 4.13 and 4.14. The R_{Lu_s} results plotted in Figure 4.13 are given in both the direction of mean drift (x_3) and one of the two transverse directions (x_1).

The DNS Lagrangian autocorrelation functions from the gravity simulations decrease faster, and therefore have smaller Lagrangian integral timescales compared to the zero gravity case. This is a result of the CTE, which causes particles to spend less time in regions with highly correlated velocities since a particle with a drift velocity will often traverse an eddy before it dies. Additionally, the R_{Lu_s} and R_{Lp} results are

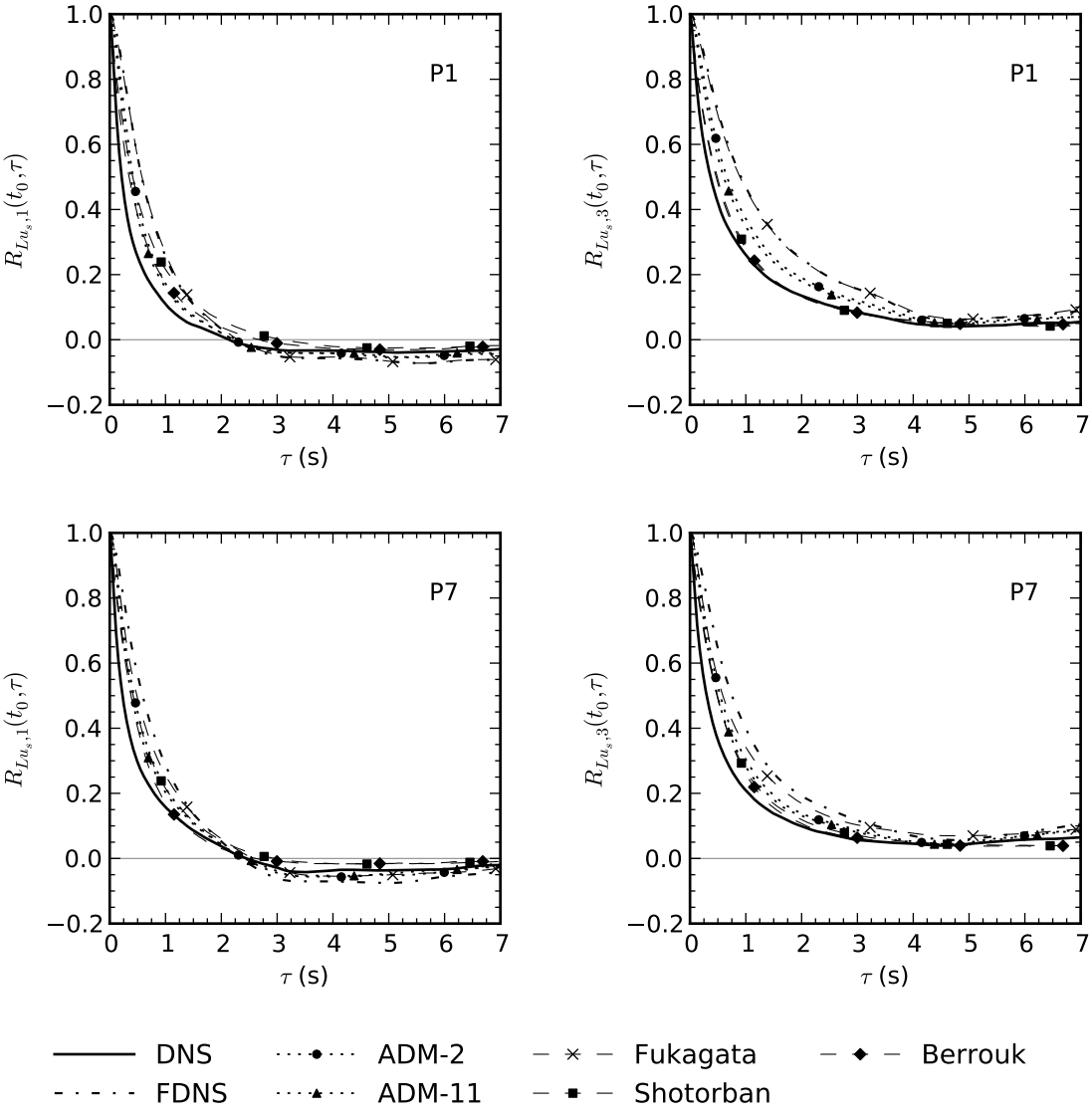

Figure 4.13: Lagrangian autocorrelation coefficient function of seen fluid velocity in directions x_1 (transverse direction) and x_3 (mean drift direction) along a particle's path, for two particle types with initial time $t = t_0$. *A priori* testing with filter size $\Delta = 16h_{DNS}$, standard model constants, and drift velocity $u_d = 0.1\,\mathrm{m/s}$.

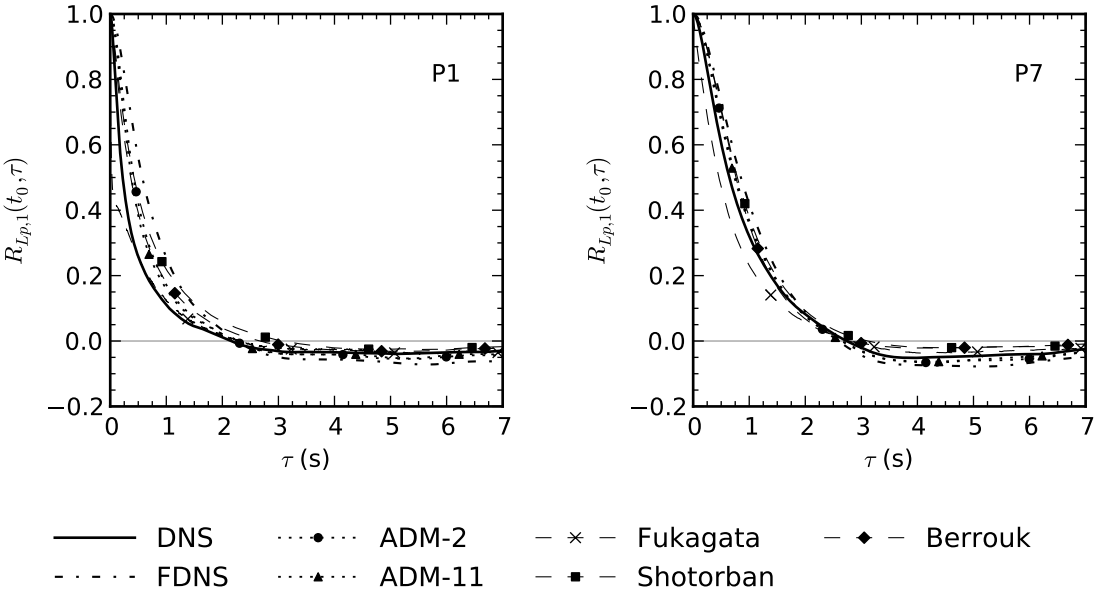

Figure 4.14: Lagrangian autocorrelation coefficient function of particle velocity in direction x_1 for two particle types with initial time $t = t_0$. *A priori* testing with filter size $\Delta = 16h_{DNS}$, standard model constants, and drift velocity $u_d = 0.1\,\mathrm{m/s}$.

less dependent on Stokes number in the gravity case. However, this may be partially due to the drift velocity being constant for all particle types, which would obviously not be the case if the gravitational constant was the same for all particles. Lastly, the autocorrelation coefficient functions in the direction of mean drift always remain positive, but in the transverse directions they contain negative loops. The negative values are caused by particles entering an eddy's back flow in order to satisfy continuity (Csanady, 1963).

The Lagrangian autocorrelation functions from the gravity simulations show much less variation among the DNS, FDNS and particle SGS models than in the zero gravity tests. When gravity is included, the mean drift velocity is the primary factor that causes particles to become uncorrelated with their initial velocities, causing the different models to have much more similar R_{Lu_s} and R_{Lp} functions. The model

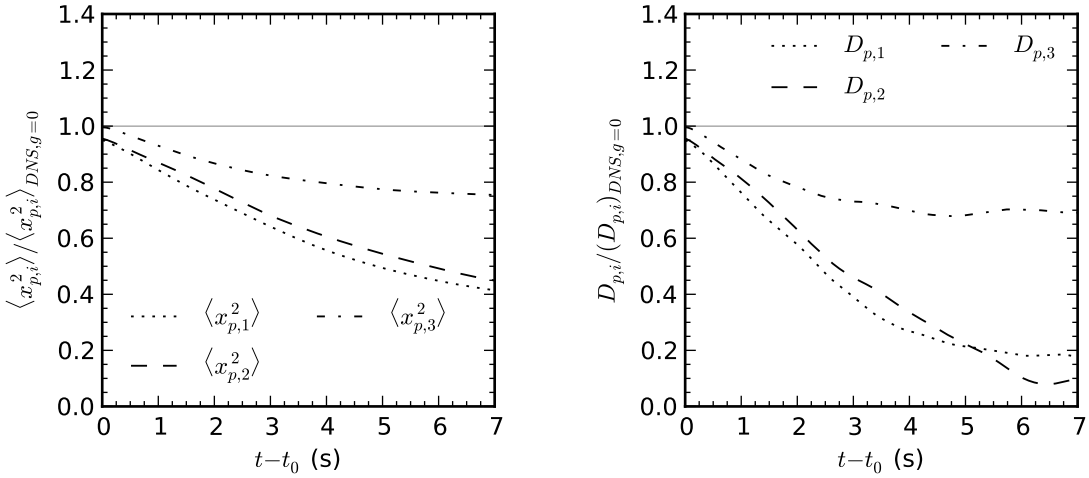

Figure 4.15: Time development of DNS particle dispersion and dispersion rate normalized by the zero gravity results for particle type P5 with drift velocity $u_d = 0.1\,\mathrm{m/s}$.

results generally lag the DNS, with the main exception being R_{Lp} from the model of Fukagata *et al.* (2004) due to the random component as explained in Section 4.1.1. The results from ADM and the stochastic models of Shotorban and Mashayek (2006) and Berrouk *et al.* (2007) are similar in the transverse directions, but the stochastic models are superior in the mean drift direction. For small and medium sized particles the model proposed by Berrouk *et al.* (2007) is superior to that of Shotorban and Mashayek (2006) due to the corrections for crossing trajectory and continuity effects.

Figure 4.15 shows DNS time development of the particle dispersion and rate of dispersion normalized by the DNS zero gravity results for particle type P5. The overall rate of dispersion is reduced due to the CTE, and the rate of dispersion in the transverse directions is much less than in the gravity direction due to the continuity effect. Dispersion rates are further reduced with time as the crossing trajectory and continuity effects become more significant. The normalized dispersion plots for all particle types are similar to the P5 particle type plots shown in Figure 4.15 since the

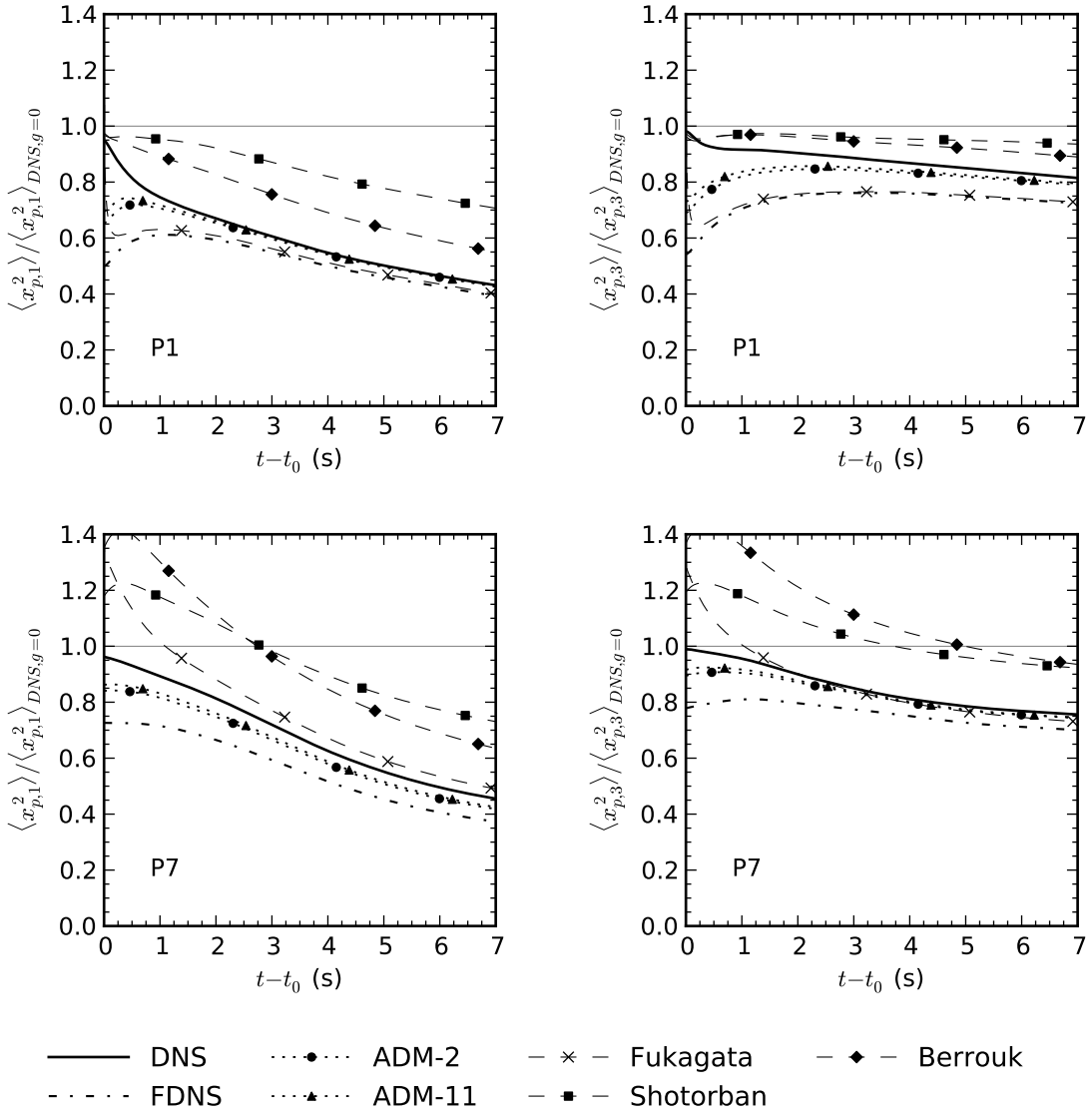

Figure 4.16: Time development of particle mean square dispersion in directions x_1 (transverse direction) and x_3 (mean drift direction) normalized by the DNS zero gravity results for two particle types. *A priori* testing with filter size $\Delta = 16h_{DNS}$, standard model constants, and drift velocity $u_d = 0.1\,\mathrm{m/s}$.

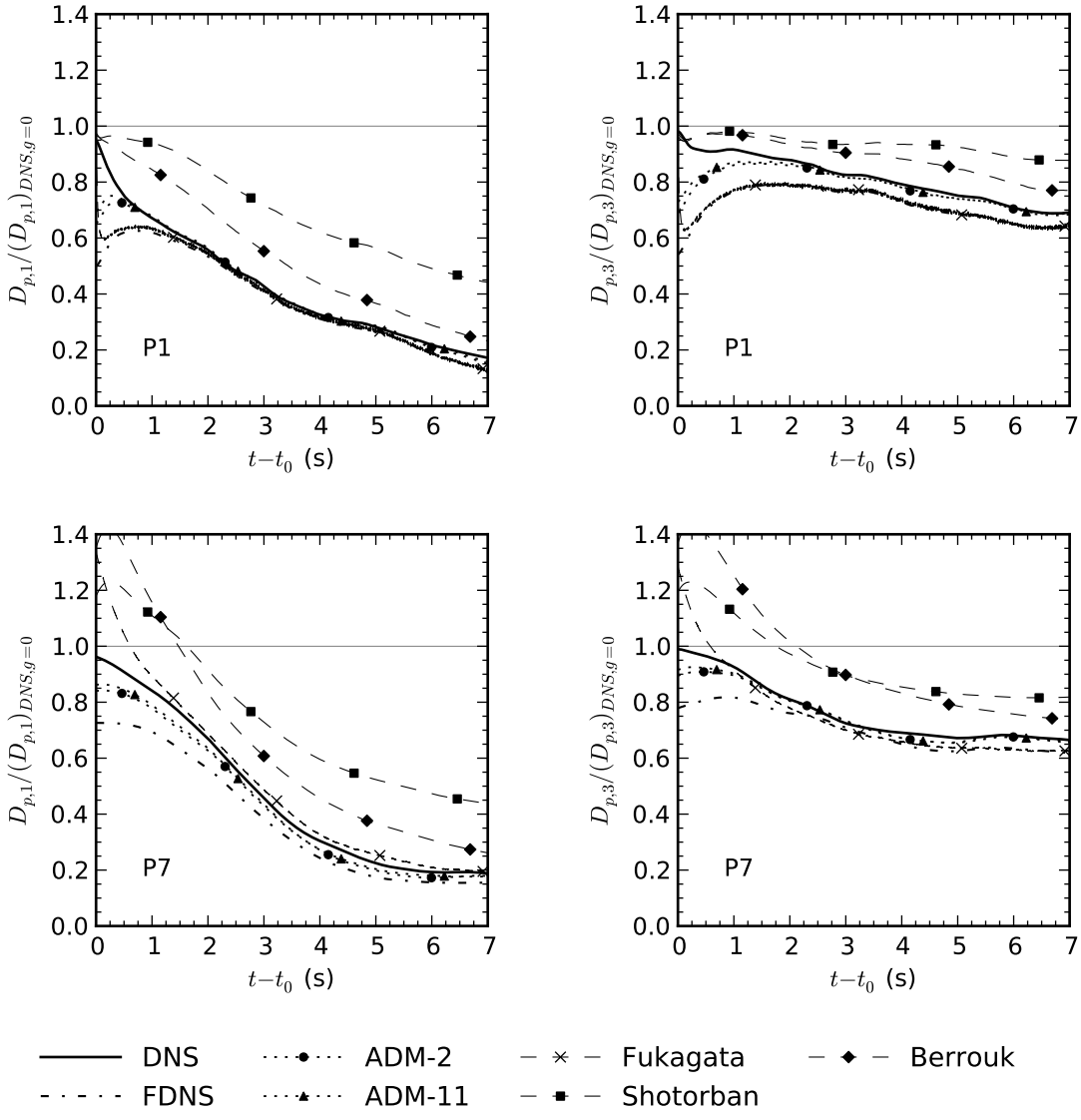

Figure 4.17: Time development of particle turbulent diffusivity in directions x_1 (transverse direction) and x_3 (mean drift direction) normalized by the DNS zero gravity results for two particle types. *A priori* testing with filter size $\Delta = 16h_{DNS}$, standard model constants, and drift velocity $u_d = 0.1\,\mathrm{m/s}$.

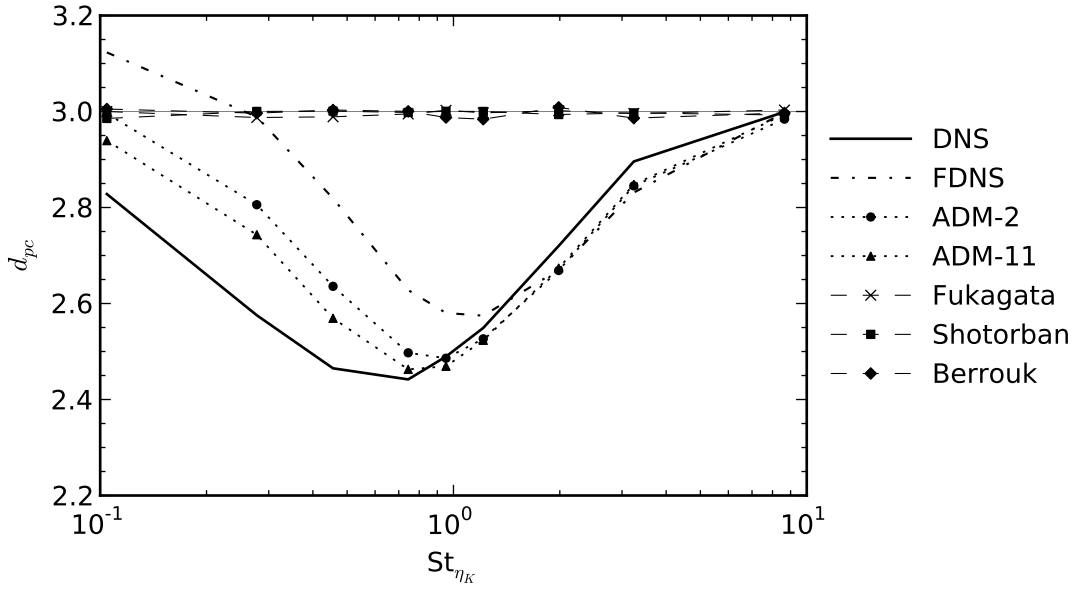

Figure 4.18: Fractal dimension at time $t = 4.0\,\mathrm{s}$. *A priori* testing with filter size $\Delta = 16h_{DNS}$, standard model constants, and drift velocity $u_d = 0.1\,\mathrm{m/s}$.

drift velocity is the same for all particles.

Normalized dispersion and rates of dispersion from the particle SGS models are plotted in Figures 4.16 and 4.17, respectively. As in the no gravity case, FDNS underpredicts dispersion and ADM is between the FDNS and DNS dispersion results. The model of Fukagata *et al.* (2004) also shows similar behaviour to the zero gravity simulations. Unlike the zero gravity case, the models of Shotorban and Mashayek (2006) and Berrouk *et al.* (2007) overpredict dispersion for all particle sizes. The model of Berrouk *et al.* (2007) better predicts particle dispersion than the model of Shotorban and Mashayek (2006) in the presence of gravity, except for the absolute largest particles (P9) at early times due to the error prone particle inertia correction.

Including gravity does not significantly alter the preferential concentration results, as shown by the fractal dimension plotted in Figure 4.18. Gravity causes a small overall decrease in particle clustering and a slight increase in the Stokes number at

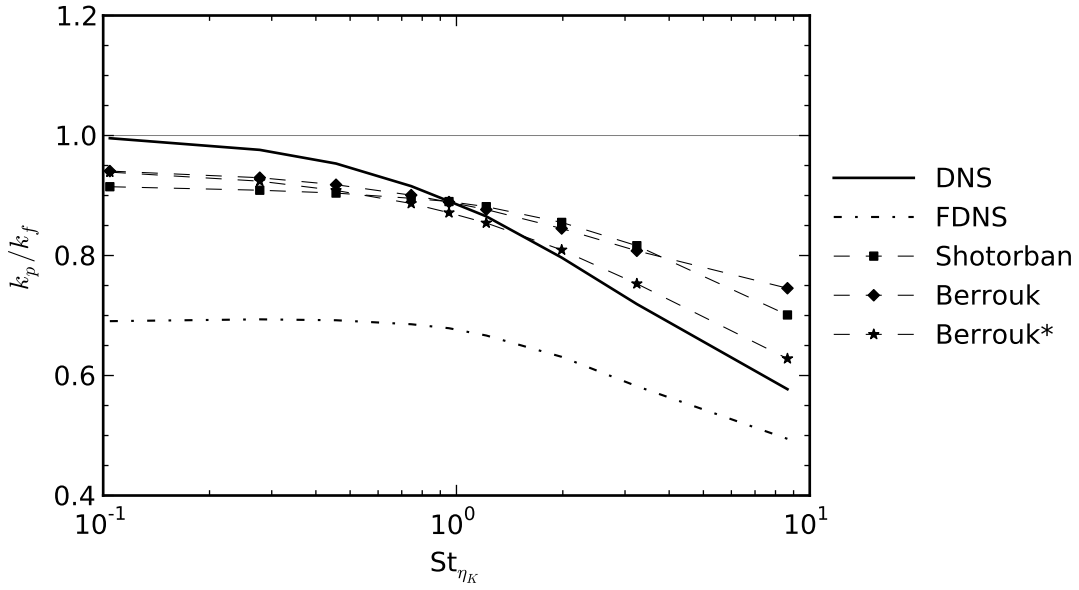

Figure 4.19: Turbulent kinetic energy of the particles at time $t = 4.0\,\mathrm{s}$. *A priori* testing with filter size $\Delta = 16h_{DNS}$, standard model constants, and drift velocity $u_d = 0.1\,\mathrm{m/s}$. Superscript * denotes model of Berrouk *et al.* (2007) with particle inertia correction neglected.

which maximum particle clustering occurs. However, there are no differences between the gravity and zero gravity tests when comparing the preferential concentration results from the DNS, FDNS and particle SGS models to one another.

The gravity simulation results have shown that the model of Berrouk *et al.* (2007) is able to account for the crossing trajectory and continuity effects, but the particle inertia correction causes significant errors for large particles. In order to isolate the gravity aspects of the model, additional tests were done using the model of Berrouk *et al.* (2007) but excluding the particle inertia correction. This modified model of Berrouk *et al.* (2007) had identical results as the original model for small particles as expected, but for intermediate and high inertia particles all statistics, apart from preferential concentration, were significantly improved. This is well exemplified by

Figure 4.19, which shows that for the largest Stokes numbers the TKE of the particles predicted by the model of Shotorban and Mashayek (2006) is better than the original model of Berrouk *et al.* (2007), but the modified model is superior to both. With the correct value of β and other model constants, the model of Berrouk *et al.* (2007) may be capable of accurately predicting many different types of particle statistics.

4.1.3 Filter size test

The particle SGS models were tested using four filter sizes to evaluate the performance of the models with different amounts of resolved fluid TKE. Standard model constants were used for the filter size tests which were conducted with and without gravity. The four filter sizes tested were $\Delta = 4h_{DNS}$, $\Delta = 8h_{DNS}$, $\Delta = 16h_{DNS}$, and $\Delta = 32h_{DNS}$, where h_{DNS} is the DNS grid spacing. Only particle types P2, P5 and P8 were tested, which were selected to represent small, intermediate and large inertia particles, respectively. Many of the results in this section are plotted as a function of resolved fluid TKE for a single particle type and at a single time. In these plots the filter size increases in the negative x-axis direction, and the DNS results are a horizontal line since they are independent of filter size. Most of the results shown are for zero gravity since the effect of filter size was usually the same with and without gravity, unless otherwise noted.

The TKE of the particles in zero gravity is shown in Figure 4.20. The seen fluid TKE results (not shown) are similar to the particle TKE results. As expected, the FDNS particle TKE decreases substantially with filter size. Figure 4.20 shows that TKE is poorly predicted by ADM for large filter sizes, which is expected since ADM can only improve scales that are larger than the LES grid. Although it always remains

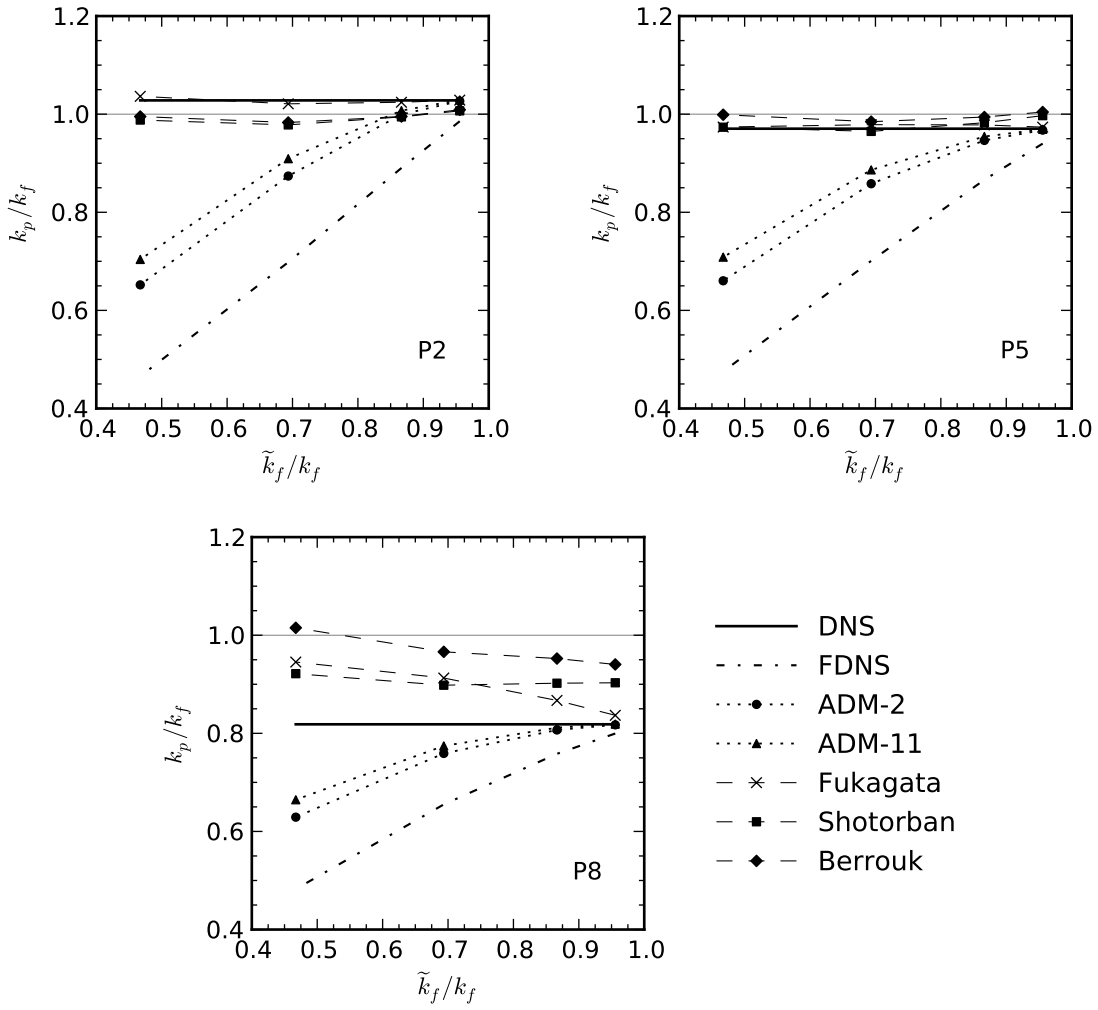

Figure 4.20: Turbulent kinetic energy of the particles as a function of resolved energy at time $t = 4.0\,\mathrm{s}$. *A priori* testing with standard model constants and zero gravity.

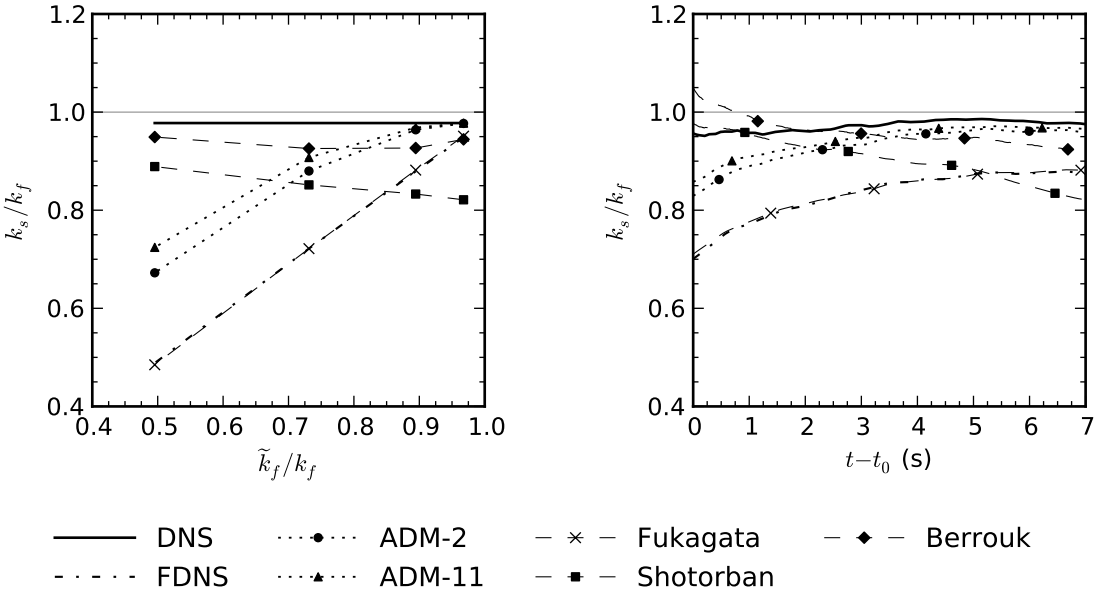

Figure 4.21: Turbulent kinetic energy of the fluid seen by the particles for particle type P5 as a function of resolved energy at time $t = 7.0\,\mathrm{s}$ (left), and as a function of time for filter size $\Delta = 8h_{DNS}$ (right). *A priori* testing with standard model constants and drift velocity $u_d = 0.1\,\mathrm{m/s}$.

fairly small, the difference between ADM-2 and ADM-11 increases with filter size. For most particle types the TKE of the particles predicted by the stochastic models shows little dependence on filter size. This is likely because the fluid SGS TKE, which is used in the stochastic models, is calculated directly from the FDNS and DNS velocity fields. If the fluid SGS TKE was calculated using a model (which is necessary in a real LES) then the particle TKE may be more dependent on the filter size. Nevertheless, the results demonstrates that stochastic models have the potential to recover all of the SGS energy no matter the filter size, which cannot be said of ADM.

An unexpected result is that for the gravity simulations with small filter sizes the TKE of the seen fluid predicted by the models of Shotorban and Mashayek (2006) and Berrouk *et al.* (2007) is less than the FDNS at long times. This can be seen in

in Figure 4.21 for particle type P5, but this result occurs for all nine particle types tested. This result is difficult to explain. Figure 4.21 displays a clear trend that k_s decreases with time for the stochastic models of Shotorban and Mashayek (2006) and Berrouk *et al.* (2007), but this only occurs when gravity is included. The problem is worse for the model of Shotorban and Mashayek (2006) than the model proposed by Berrouk *et al.* (2007), which indicates that the problem is related to the value of the fluid SGS Lagrangian integral timescale along an inertial particle's path, or to the random component coefficient. This suggests that the problem may be resolved, or at least lessened, with proper model constant values. The fact that this result occurs for all particle types suggests that it cannot be attributed to preferential concentration. Conversely, the $\widetilde{k}_{f@p}$ results (not shown) indicate that there may be some differences in the spatial distributions of the largest particles among the different models. For large particles at long times, the models of Shotorban and Mashayek (2006) and Berrouk *et al.* (2007) predict slightly larger values of $\widetilde{k}_{f@p}$ than FDNS and the other models. This discrepancy can only be caused by differences in particle distributions.

Particle velocity Lagrangian autocorrelation coefficient functions for the four different filter sizes are shown in Figure 4.22. For simplicity only $R_{Lp,3}(t_0, \tau)$ for particle type P5 in zero gravity results are presented. The results for other Lagrangian autocorrelation functions (R_{Lu_s}, other particle types, including gravity) are largely the same regarding the effect of filter size. For the smallest two filter sizes all of the models and the FDNS produce R_{Lp} results that agree well with the DNS, but clear differences exist between the DNS, FDNS and models for the two largest filter sizes. As expected, the FDNS and ADM Lagrangian particle timescales increases with filter

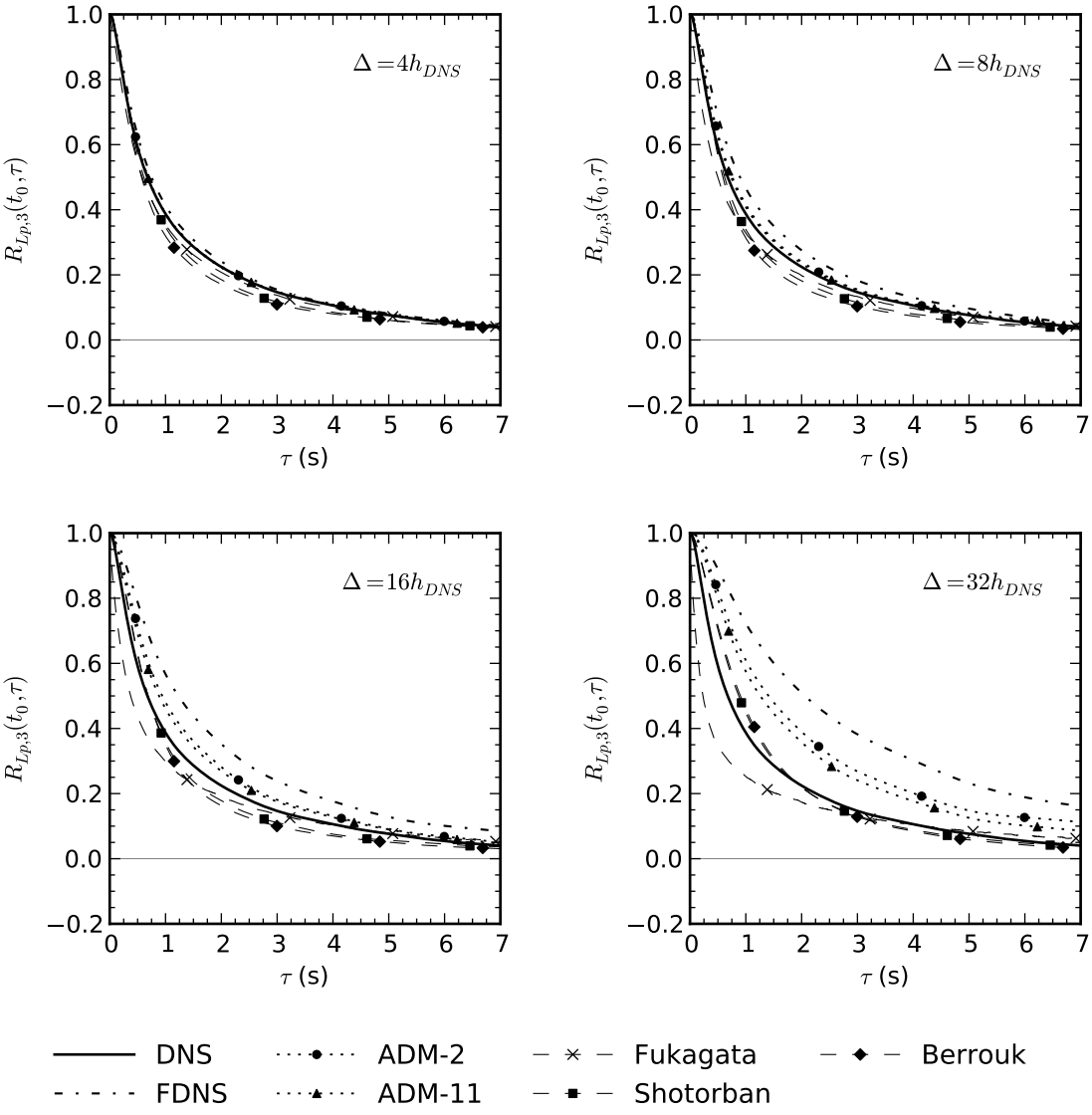

Figure 4.22: Lagrangian autocorrelation coefficient function of particle velocity in direction x_3, for particle type P5 with initial time $t = t_0$. *A priori* testing with various filter sizes, standard model constants, and zero gravity.

size since a larger range of turbulent scales are removed which would otherwise contribute to particle velocities becoming uncorrelated in time. The small filter results for the model of Fukagata *et al.* (2004) are excellent. However, as the filter size is increased R_{Lp} drops very quickly at short times, as seen in the previous sections, since the random component becomes more significant as the SGS TKE becomes greater. Overall the stochastic models of Shotorban and Mashayek (2006) and Berrouk *et al.* (2007) yield the best particle velocity Lagrangian autocorrelation coefficient function results. These two models are excellent for the three smallest filters, but tend to slightly overpredict R_{Lp} in the case of the largest filter size, particularly for the larger particles. A notable result from the gravity simulations is that the negative loops in the transverse direction FDNS Lagrangian autocorrelation functions become larger with increasing filter size. This can be explained by the filtered fields containing only large turbulent structures, which therefore have larger back flows associated with them.

The influence of filter size on particle dispersion and turbulent diffusivity is shown in Figures 4.23 and 4.24, respectively. The FDNS and ADM dispersion results for small filer sizes agree well with the DNS, but as the filter size increases dispersion is underpredicted since the FDNS and ADM particle TKE decreases with filter size. Particle dispersion and rate of dispersion from the model of Fukagata *et al.* (2004) also decrease as less energy is resolved, but the cause is different than in the case of FDNS and ADM. For the model of Fukagata *et al.* (2004) the particle TKE is well predicted for all filter sizes, but for larger filter sizes the particle velocity Lagrangian integral timescale is underpredicted, and therefore dispersion is reduced. For small and intermediate sized particles the models of Shotorban and Mashayek (2006) and

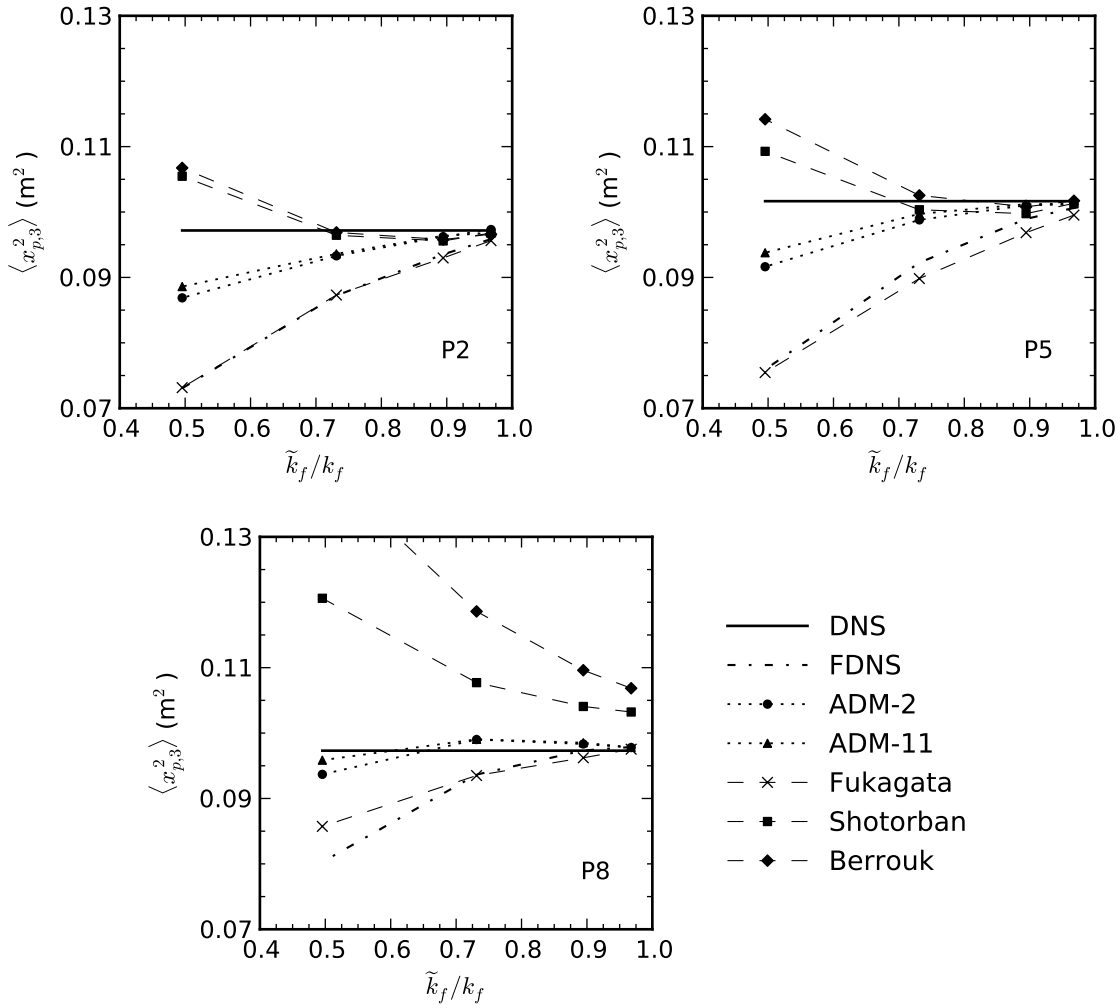

Figure 4.23: Particle mean square dispersion in direction x_3 as a function of resolved energy at time $t = 7.0\,\mathrm{s}$. *A priori* testing with standard model constants and zero gravity.

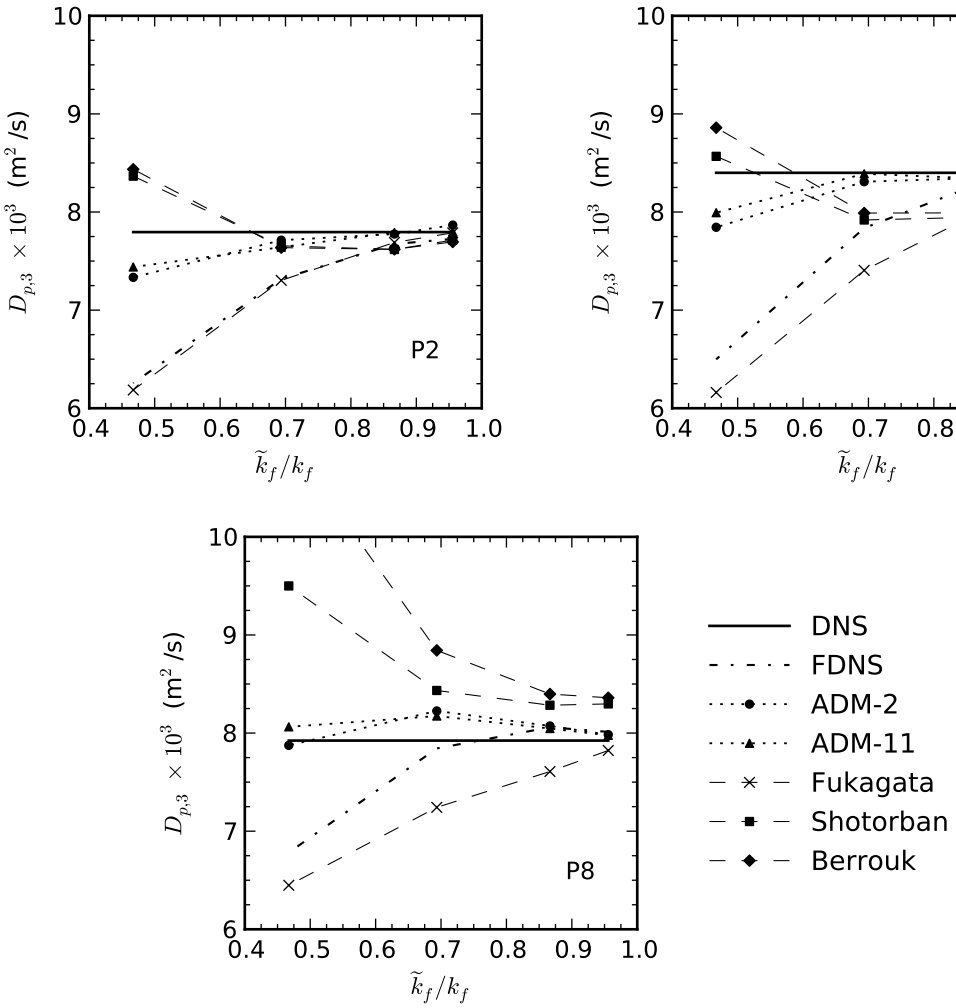

Figure 4.24: Particle turbulent diffusivity in direction x_3 as a function of resolved energy at time $t = 7.0\,\mathrm{s}$. *A priori* testing with standard model constants and zero gravity.

Berrouk *et al.* (2007) yield good results for both the particle TKE and Lagrangian integral timescale for the three smallest filter sizes, which leads to dispersion results that agree well with the DNS. However, these two models overpredict dispersion for the large filter sizes due to the large particle Lagrangian integral timescales. In summary, increasing the filter size causes FDNS, ADM and the model of Fukagata *et al.* (2004) particle dispersion to decrease, and conversely dispersion from the Langevin based models tends to increase with filter size.

Fractal dimension plots as a function of time for particle type P5 and the four different filter sizes are shown in Figure 4.25. Particle type P5 was chosen since it is an intermediate sized particle that experiences significant particle clustering. As previously observed, filtering causes a decrease in preferential concentration for small Stokes numbers and an increase in preferential concentration for large Stokes numbers. In Figure 4.25 particle clustering is overpredicted at early times ($\mathrm{St}_{\eta_K} > 1.0$) and is underpredicted at later times ($\mathrm{St}_{\eta_K} < 1.0$) by FDNS and ADM. These effects become more pronounced as the filter size is increased. The stochastic models predict zero preferential concentration for all filter sizes as a result of the randomizing effect. The only exception is that the model of Fukagata *et al.* (2004) predicts a small amount of particle clustering for the smallest filter size.

4.1.4 Model constants test

The final set of *a priori* tests were conducted with the purpose of determining the importance and sensitivity of the stochastic particle SGS model constants C_0 and C_ϵ, which are the Langevin model constant and LES dissipation coefficient, respectively. The parameters of the model constants test were chosen to be similar to the standard

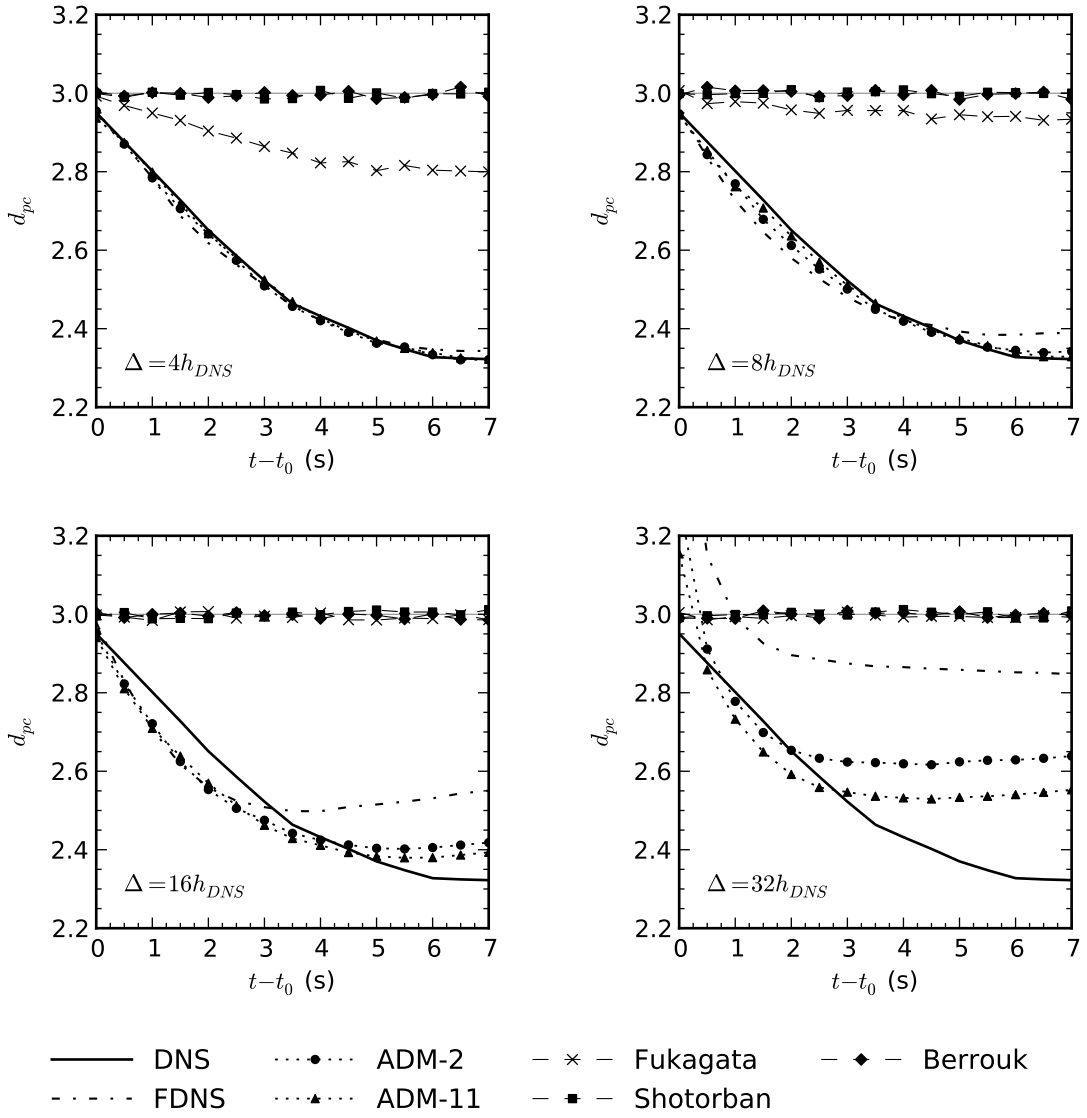

Figure 4.25: Time development of the fractal dimension for particle type P5. *A priori* testing with various filter sizes, standard model constants, and zero gravity.

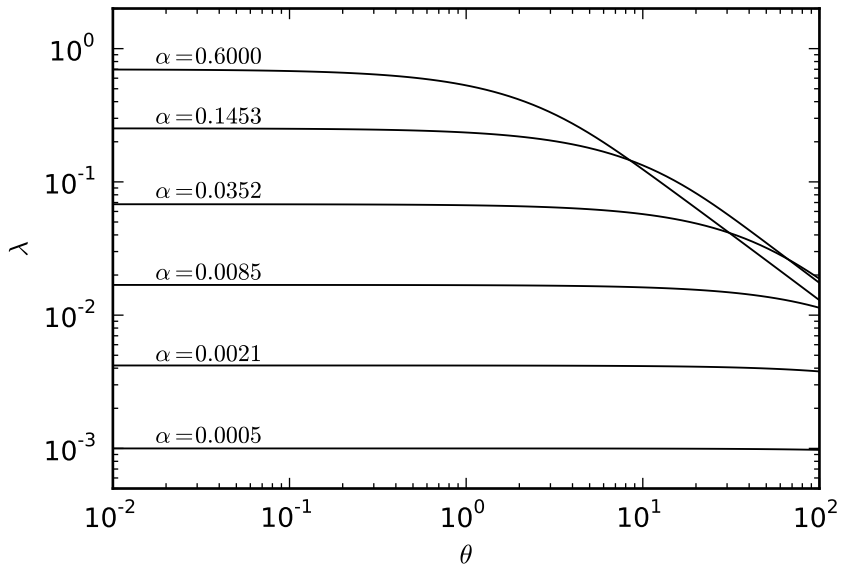

Figure 4.26: Relationship between the parameters λ, α and β in the model of Fukagata *et al.* (2004). Mathematical relationship is given in equation (2.39).

test parameters. For the model constants test, a single filter size of $\Delta = 16h_{DNS}$ was used, all particle types were tested, and simulations were run with and without gravity. The different model constants tested were reviewed in Section 3.4.10 and are listed in Table 3.4.

The model constant tests revealed the results from the model of Fukagata *et al.* (2004) to be independent of model constant values. Different model constants produced nearly identical results with extremely minor differences in all cases. This model behaviour can be explained by analysing the role of the constants in the formulation of the model of Fukagata *et al.* (2004). In this model the constants C_0 and C_ϵ are only used to evaluate the Lagrangian fluid SGS timescale along an inertia particle's path ($T^*_{L,sgs}$). The timescale $T^*_{L,sgs}$ is then used to evaluate the dummy variable θ as shown in equation (2.40), which in turn is used to evaluate the dummy variable λ with the relationship given in (2.39). Finally, the dummy variable λ is used to

evaluate the SGS Brownian force using (2.38). Therefore, the model constant values are only important if λ is dependent on θ. Figure 4.26 is a plot of λ as a function of θ for a range of α values. For the current simulations the maximum parameter values experienced are $\alpha = 0.054$ and $\theta = 22$. These maximum values never occur simultaneously since α and θ share an inverse relationship. Figure 4.26 clearly shows that for the current range of α and θ values the dummy variable λ is independent of θ, which explains why different model constants yield identical results. The dummy variable λ is only dependent on θ when both α and θ are large, which would only occur in the unrealistic condition of a simulation with a large timestep and a small filter size. This demonstrates that for reasonable simulation and particle parameters, the Lagrangian fluid SGS timescale along an inertia particle's path has minimal effect on the model of Fukagata *et al.* (2004).

The influence of the model constants C_0 and C_ϵ is largely the same for the stochastic models of Shotorban and Mashayek (2006) and Berrouk *et al.* (2007) since these models are formulated similarly. The effects of the model constants can be more easily understood by defining the dummy variables ω and γ, and rearranging the equations from the model of Shotorban and Mashayek (2006) to give:

$$\omega = C_\epsilon \left(\frac{1}{2} + \frac{3}{4} C_0 \right) \qquad T^*_{L,sgs} = \left(\frac{1}{\omega} \right) \frac{\Delta}{\sqrt{k_{sgs}}} \tag{4.1}$$

$$\gamma = C_\epsilon C_0 \qquad C_0 \epsilon_{sgs} = \gamma \frac{\left(k_{sgs}\right)^{3/2}}{\Delta} \tag{4.2}$$

The dummy variables ω and γ are functions only of model constants C_0 and C_ϵ. Equations (4.1) and (4.2) show that both of the constants have the same type of behaviour. Increasing either constant causes the SGS fluid Lagrangian timescale

C_0	C_ϵ	ω	γ
1.0	1.4	1.75	1.40
2.1^*	1.0^*	2.08	2.10
2.1	1.4	2.91	2.94
2.1	1.8	3.74	3.78
3.2	1.4	4.06	4.48

Table 4.1: Values of dummy variables ω and γ for the different combinations of model constants C_0 and C_ϵ used in the model constant testing. Superscript * denotes standard constant values, which were the values used in the previous tests.

along a particle's path ($T^*_{L,sgs}$) to decrease, and the random component of the model ($C_0\epsilon_{sgs}$) to increase. The values of the dummy variables ω and γ for the different combinations of model constants tested are given in Table 4.1. In regard to the effects of the model constants, the only differences with the model of Berrouk *et al.* (2007) is extra complexities for particle inertia and the Csanady correction factors, but the trends that result from changing the constant values would be expected to be the same for both models.

The TKE of the particles from the model of Shotorban and Mashayek (2006) in the case of zero gravity are shown in Figure 4.27. The general trend for the seen fluid TKE (not shown) from either model with or without gravity is that k_s is increased as the model constant values are increased. This is due to the random component adding more energy as the variable γ is increased. However, this is not always the case for the TKE of the particles since reducing the timescale $T^*_{L,sgs}$ appears to have a significant effect. As seen in Figure 4.27, the larger model constants better match the DNS k_p trend with respect to Stokes number, whereas the small constants yield flatter k_p results. The TKE results are not very sensitive to the model constant values considering the large range of values tested. Furthermore, a rather large amount of

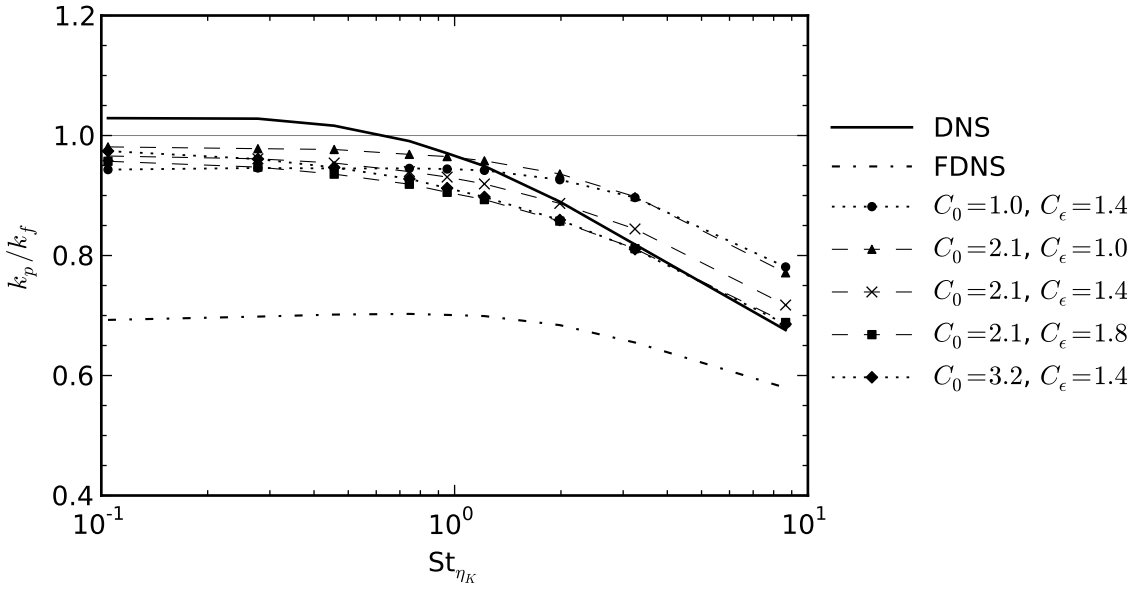

Figure 4.27: Turbulent kinetic energy of the particles at time $t = 4.0\,\mathrm{s}$ from the model of Shotorban and Mashayek (2006). *A priori* testing with filter size $\Delta = 16h_{DNS}$, various model constants, and zero gravity.

energy is filtered out in the current tests, which creates larger discrepancies between the simulations with different constant values. For smaller filter sizes the values of the model constants would be even less significant.

Figure 4.21 in Section 4.1.3 showed the unexpected result that k_s can be less than $\widetilde{k}_{f@p}$ for small filter sizes using the models of Shotorban and Mashayek (2006) or Berrouk *et al.* (2007) when gravity is included. In order to examine if this result could be attributed to values of the model constants, the seen fluid TKE of particle type P5 is plotted in Figure 4.28 for the different combinations of C_ϵ and C_0 tested. The plot shows that the model constants have little influence on the rate at which k_s decreases with time. In particular, changing the value of the Langevin model constant C_0 does not have any effect at all. However, increasing the LES dissipation coefficient C_ϵ slightly decreases the rate at which k_s decreases with time.

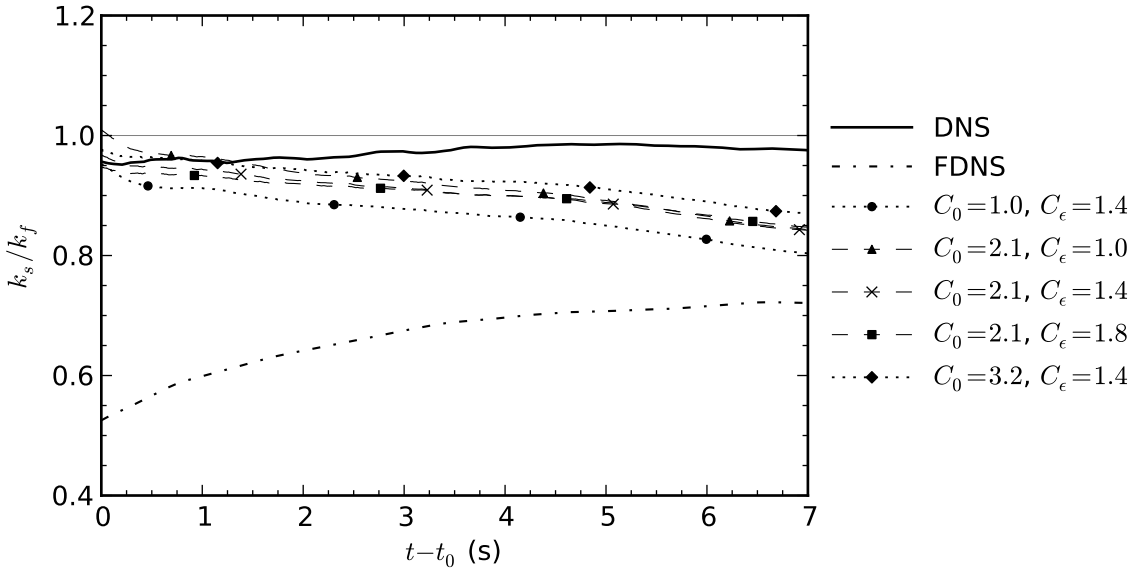

Figure 4.28: Time development of the turbulent kinetic energy of the fluid seen by the particles for particle type P5 from the model of Shotorban and Mashayek (2006). *A priori* testing with filter size $\Delta = 16h_{DNS}$, various model constants, and drift velocity $u_d = 0.1\,\mathrm{m/s}$.

The Lagrangian autocorrelation coefficient functions of the seen fluid velocity from the model of Shotorban and Mashayek (2006) with zero gravity are shown in Figure 4.29. The conclusions regarding the Lagrangian autocorrelation functions and the model constants are the same for both R_{Lu_s} and R_{Lp} (not shown) using either of the Langevin models. From the previous analytical analysis of the model constants for the Langevin models, it is known that increasing the values of constants C_0 and C_ϵ causes the timescale $T^*_{L,sgs}$ to decrease and the random contribution to increase. Both of these effects would be expected to reduce the Lagrangian integral timescales of particle velocity and seen fluid velocity. For the small and intermediate inertia particles the Lagrangian autocorrelation functions are not sensitive to the model constants, and the results are excellent for all constant values tested. However, the

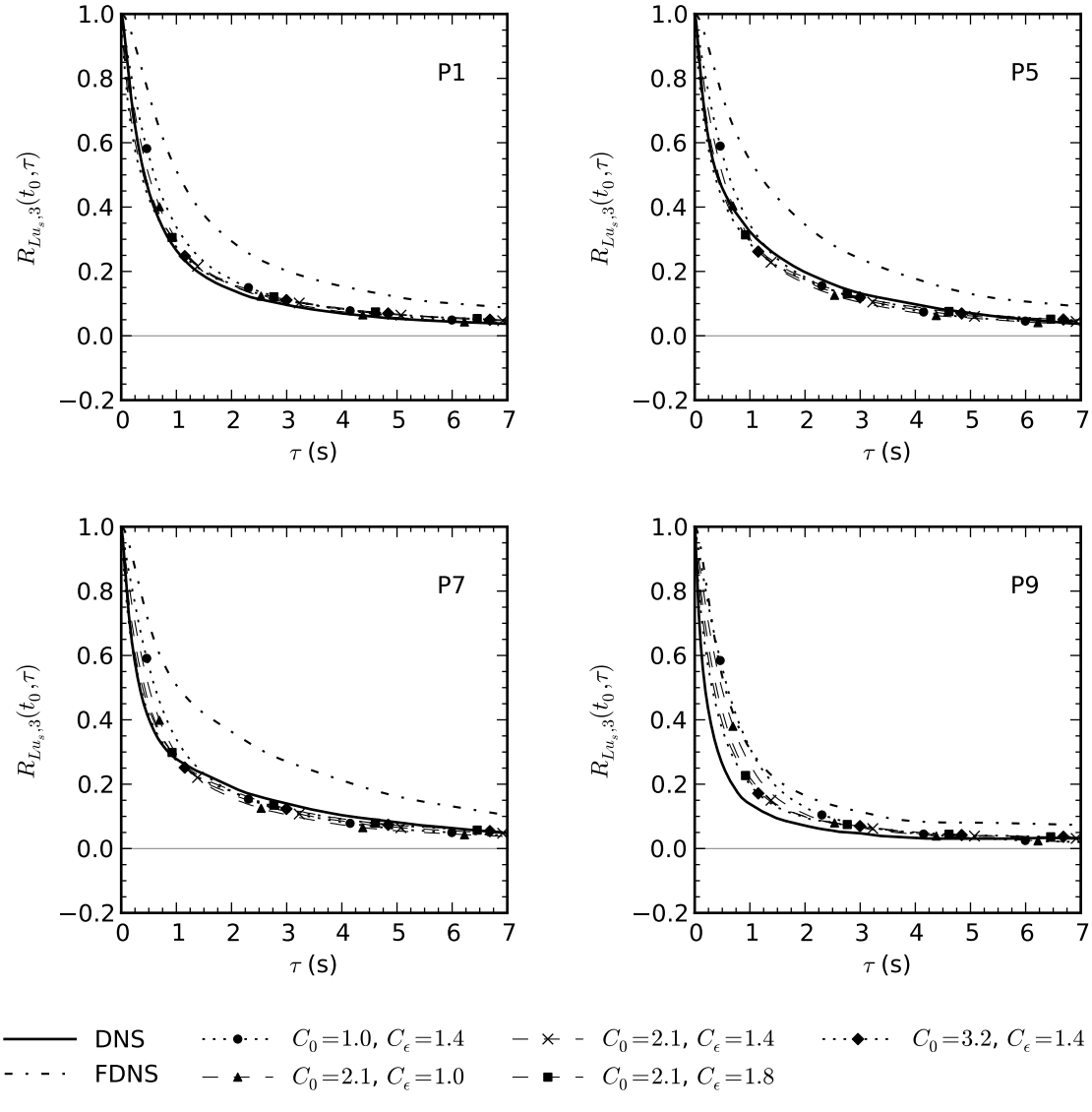

Figure 4.29: Lagrangian autocorrelation coefficient function of seen fluid velocity in direction x_3 along a particle's path, for various particle types with initial time $t = t_0$ using the model of Shotorban and Mashayek (2006). *A priori* testing with filter size $\Delta = 16h_{DNS}$, various model constants, and zero gravity.

larger particles do show some dependence on the constant values as R_{Lu_s} and R_{Lp} are reduced as C_0 and C_ϵ increase. The Lagrangian autocorrelation functions from the simulations that use the largest constants best match the results of the DNS.

The particle dispersion and rate of dispersion results for both of the Langevin models with and without gravity are shown in Figures 4.30 and 4.31. The plots show that for all cases dispersion is reduced as the model constant values are increased. This indicates that particle dispersion for the Langevin models is more affected by the reduction in the SGS fluid Lagrangian timescale along a particle's path than by the increase in the random component. When gravity is included all combinations of constants overpredict dispersion, and therefore the largest constants perform best. For the case of zero gravity the smaller constants perform best for small particles, and the larger constants perform best for large particles. These results indicate that the ideal model constant values are a function of particle properties and the drift velocity. Compared to other particle statistics, the particle dispersion and rate of dispersion results show more sensitivity to the values of the model constants.

Preferential concentration results are not shown since all three of the stochastic particle SGS models predict zero particle clustering for all of the different combinations of model constants tested.

Overall, for most of the particle statistics examined the results are not very sensitive to model constant values considering the large range of values tested, and that the filter size of the current simulations is relatively large. Most of the results show that the largest combination of model constants tested ($C_0 = 3.2$ and $C_\epsilon = 1.4$) best agree with the DNS results. However, it must be noted that although these constants perform best in this work, this should not be considered to be a universal result.

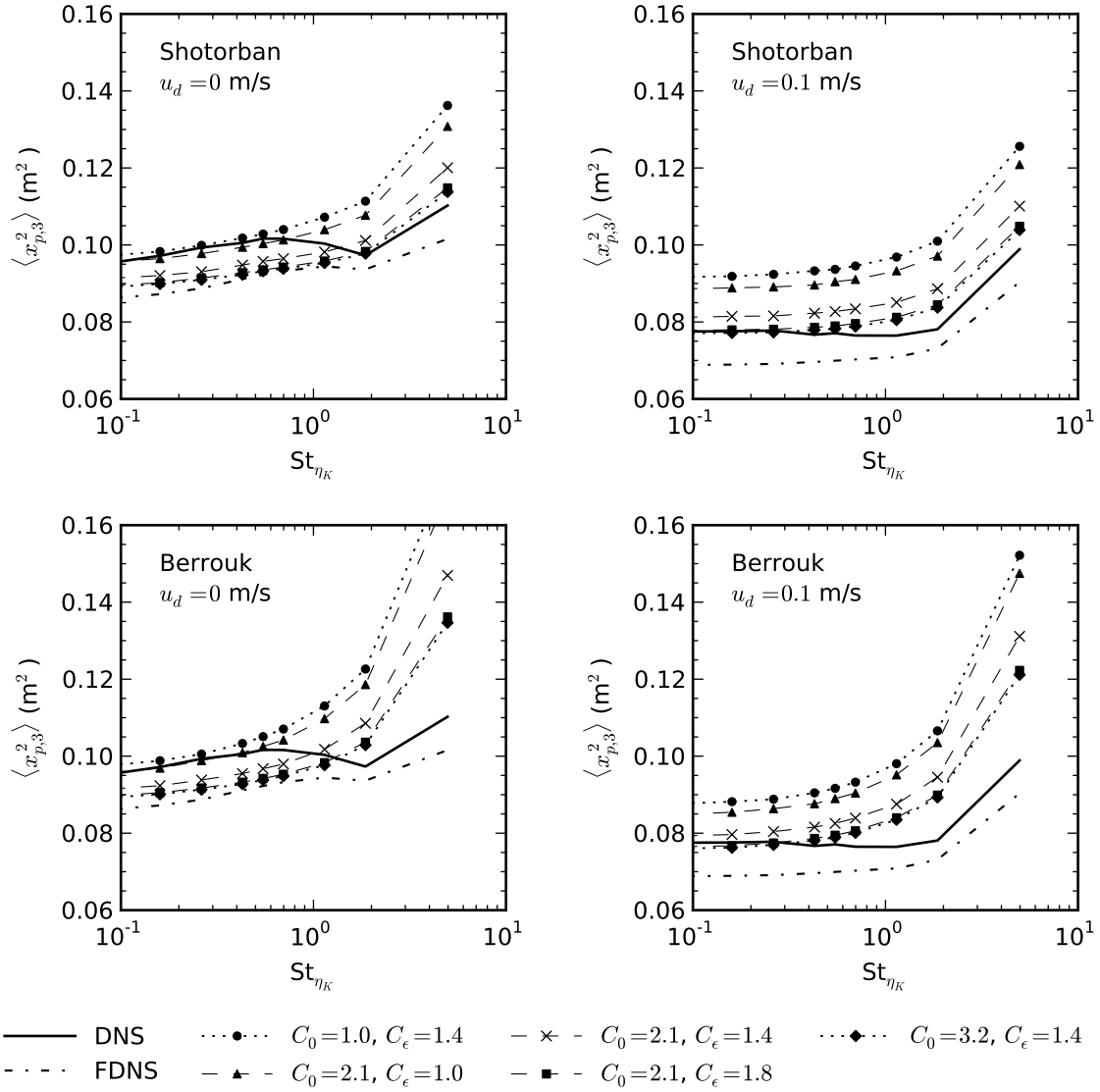

Figure 4.30: Particle mean square dispersion in direction x_3 at $t = 7.0\,\mathrm{s}$ from the models of Shotorban and Mashayek (2006) and Berrouk *et al.* (2007). *A priori* testing with filter size $\Delta = 16h_{DNS}$, various model constants, and including/neglecting gravity.

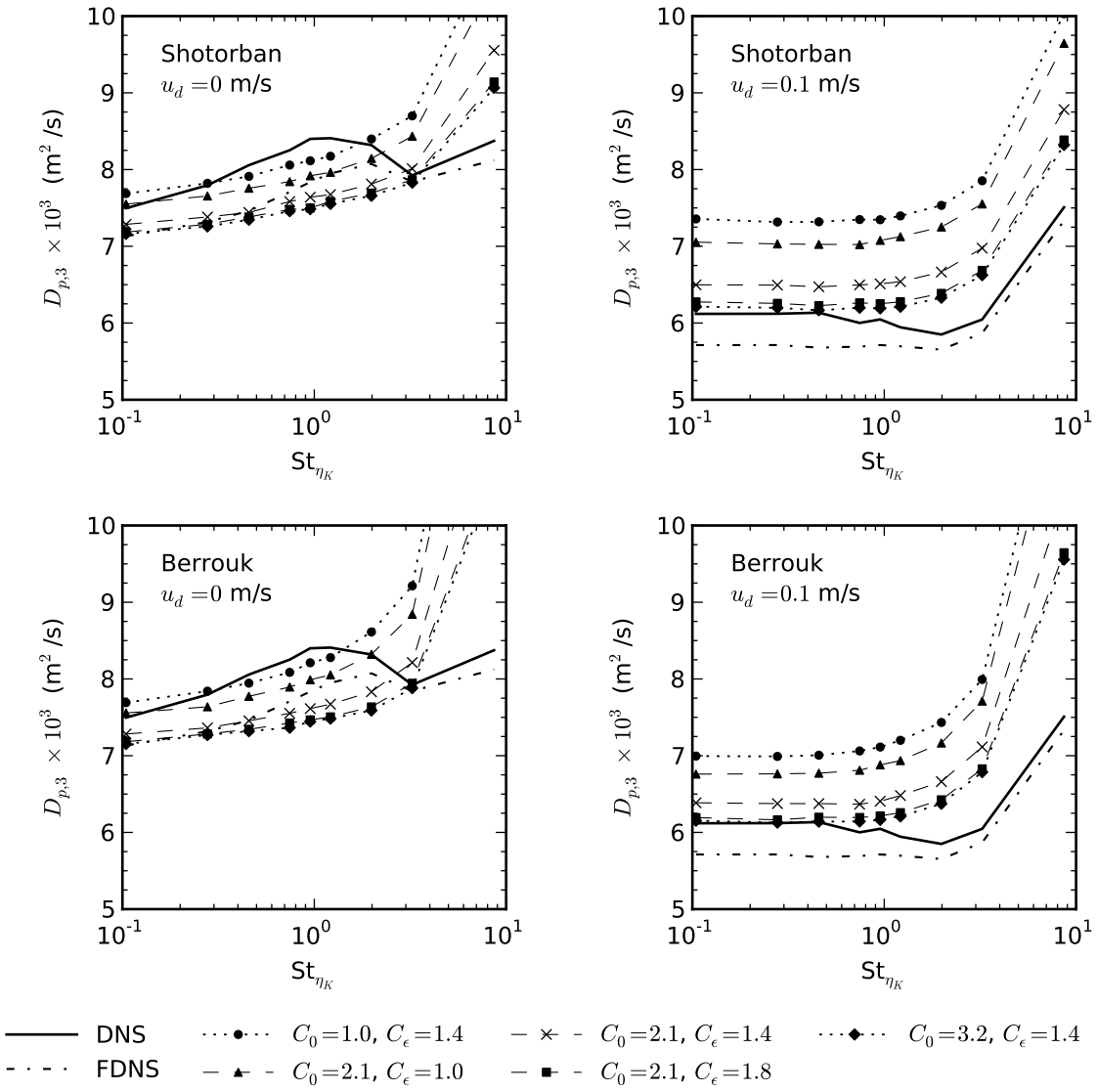

Figure 4.31: Particle turbulent diffusivity in direction x_3 at $t = 4.0\,\mathrm{s}$ from the models of Shotorban and Mashayek (2006) and Berrouk *et al.* (2007). *A priori* testing with filter size $\Delta = 16h_{DNS}$, various model constants, and including/neglecting gravity.

For a given simulation the ideal model constant values will be a function of many simulation parameters.

4.2 *A posteriori*

This section presents the results from the *a posteriori* testing. All nine particle types were tested in zero gravity, with standard model constant values, and a filter size of $\Delta = 8h_{DNS}$. This filter size was selected based on the amount of resolved fluid TKE, as well as considering the fluid velocity field errors between the LES and FDNS simulations. LES simulations with a filter size of $\Delta = 16h_{DNS}$ had very large discrepancies with the FDNS fluid fields.

The majority of the differences between the *a priori* and *a posteriori* particle results can be explained by analysing the LES fluid results, some of which were presented in Section 3.2.4. The conclusions regarding the performance of the particle SGS models in LES from these tests are specific to the current LES fluid field, and they should not be considered to be universal. The particle LES results could change considerably if a different fluid SGS model is used since the particle LES results are dependent on the LES fluid field. For example, compared to the current work the LES velocity fields used by Shotorban and Mashayek (2006) and Gobert and Manhart (2010) had energy spectra that better matched the FDNS, which would be expected to yield superior particle LES results. Instead of drawing specific conclusions about the performance of particle SGS models in LES, the *a posteriori* tests are mainly used to demonstrate that for LES of particle-laden turbulence the particle and fluid SGS models can be equally significant.

As shown in Figure 3.4, the TKE of the LES filtered velocity field is greater

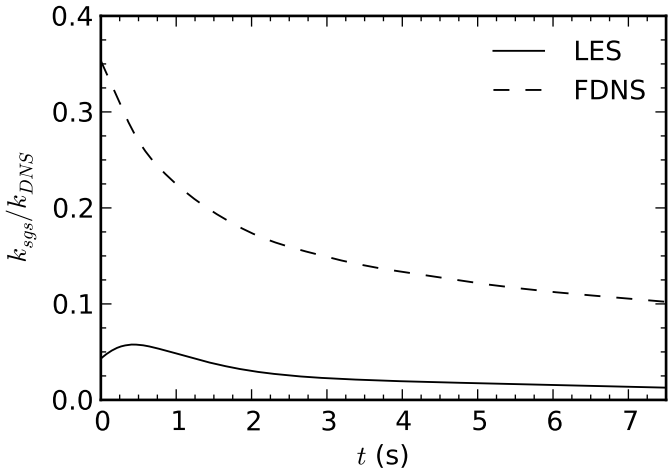

Figure 4.32: SGS turbulent kinetic energy of the LES and FDNS fluid fields normalized by the turbulent kinetic energy of the DNS. The LES and FDNS filter size is $\Delta = 8h_{DNS}$.

than the FDNS. This would be expected to increase the seen fluid and particle TKE for the LES and all particle SGS models. The stochastic particle SGS models are significantly effected by the SGS TKE, which is plotted in Figure 4.32. As explained in Section 3.4.5, the *a posteriori* SGS TKE is calculated with a method that is consistent with the dynamic Smagorinsky model, whereas the *a priori* SGS TKE is calculated directly from the DNS and FDNS velocity fields. Figure 4.32 reveals that the LES significantly underpredicts the SGS TKE compared to the FDNS. This results in very similar particle results from the LES and the model of Fukagata *et al.* (2004) since the reduced k_{sgs} values cause the SGS Brownian force to be small. For the models of Shotorban and Mashayek (2006) and Berrouk *et al.* (2007) the reduced SGS TKE will cause the SGS fluid Lagrangian timescale along a particle's path ($T^*_{L,sgs}$) to increase and the random contribution to decrease, as shown in equations (4.1) and (4.2), respectively. It is important to note that compared to the FDNS, the LES filtered TKE is increased and the SGS TKE is reduced, but the sum of these two

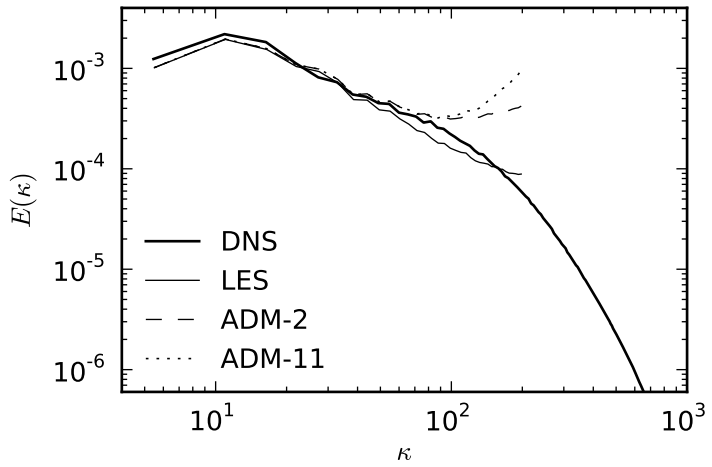

Figure 4.33: Turbulent kinetic energy spectra of the DNS, LES, and ADM velocity fields at time $t_0 = 0.5\,\mathrm{s}$. The LES filter size is $\Delta = 8h_{DNS}$.

quantities is less than the DNS TKE $\left(\widetilde{k}_f + k_{sgs}\right)_{LES} < \left(k_f\right)_{DNS}$ at all times.

Figure 3.5 shows that the LES energy spectrum does not match the FDNS spectrum, and instead resembles a spectrum that would be produced from a sharp spectral filter. This excess energy at scales near the cut-off will affect the LES particle results. It also leads to very incorrect LES ADM energy spectra since ADM adds energy to scales near the cut-off, as shown in Figure 4.33. The *a posteriori* ADM velocity of the smallest resolved scales is far too great. Furthermore, not only is the shape of the ADM spectra incorrect, but the overall amount of energy added is too large such that the ADM TKE is always greater than the DNS $\left(k_f\right)_{ADM} > \left(k_f\right)_{DNS}$.

The *a posteriori* seen fluid and particle TKE results are shown in Figure 4.34. The LES results have more energy but the same trends as the FDNS, which is expected since the LES filtered TKE is greater than the FDNS. The ADM k_s and k_p functions are overpredicted compared to the DNS since the ADM flow field contains too much energy. The only exception is that the TKE of the largest particles is slightly less

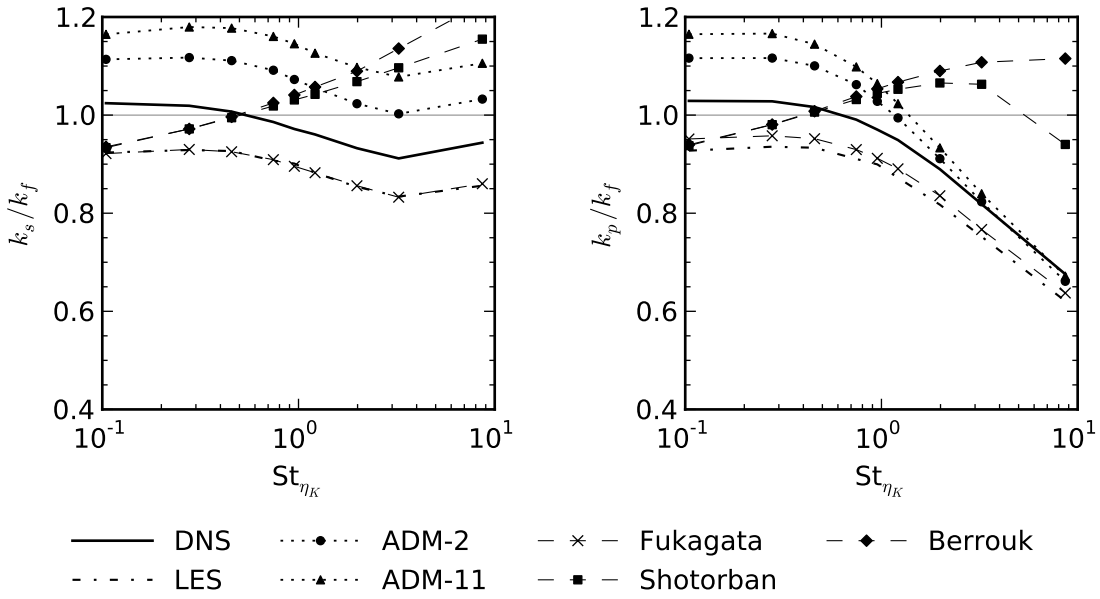

Figure 4.34: Particle and seen fluid turbulent kinetic energy at time $t = 4.0\,\mathrm{s}$. *A posteriori* testing with filter size $\Delta = 8h_{DNS}$, standard model constants, and zero gravity.

than the DNS. The reason for this is that ADM adds most of the excess energy to the smallest resolved scales, but the small scales do not significantly effect the larger particles. The larger particles are mostly effected by the large scales, and Figure 4.33 shows that the discrepancy between ADM and DNS energy spectra is minimal for the large scales. As expected, the TKE of the particles from the model of Fukagata *et al.* (2004) is only slightly greater than the LES due to the small k_{sgs} field. This demonstrates the sensitivity of the model to the SGS TKE field. The TKE from the models of Shotorban and Mashayek (2006) and Berrouk *et al.* (2007) show more dependence on Stokes number compared to the *a priori* testing, and the TKE of the larger particles is further overpredicted in the *a posteriori* simulations. Since the sum of the LES $\widetilde{k}_f$ and k_{sgs} is less than the DNS, the excess seen fluid and particle TKE must be related to the increase in timescale $T^*_{L,sgs}$.

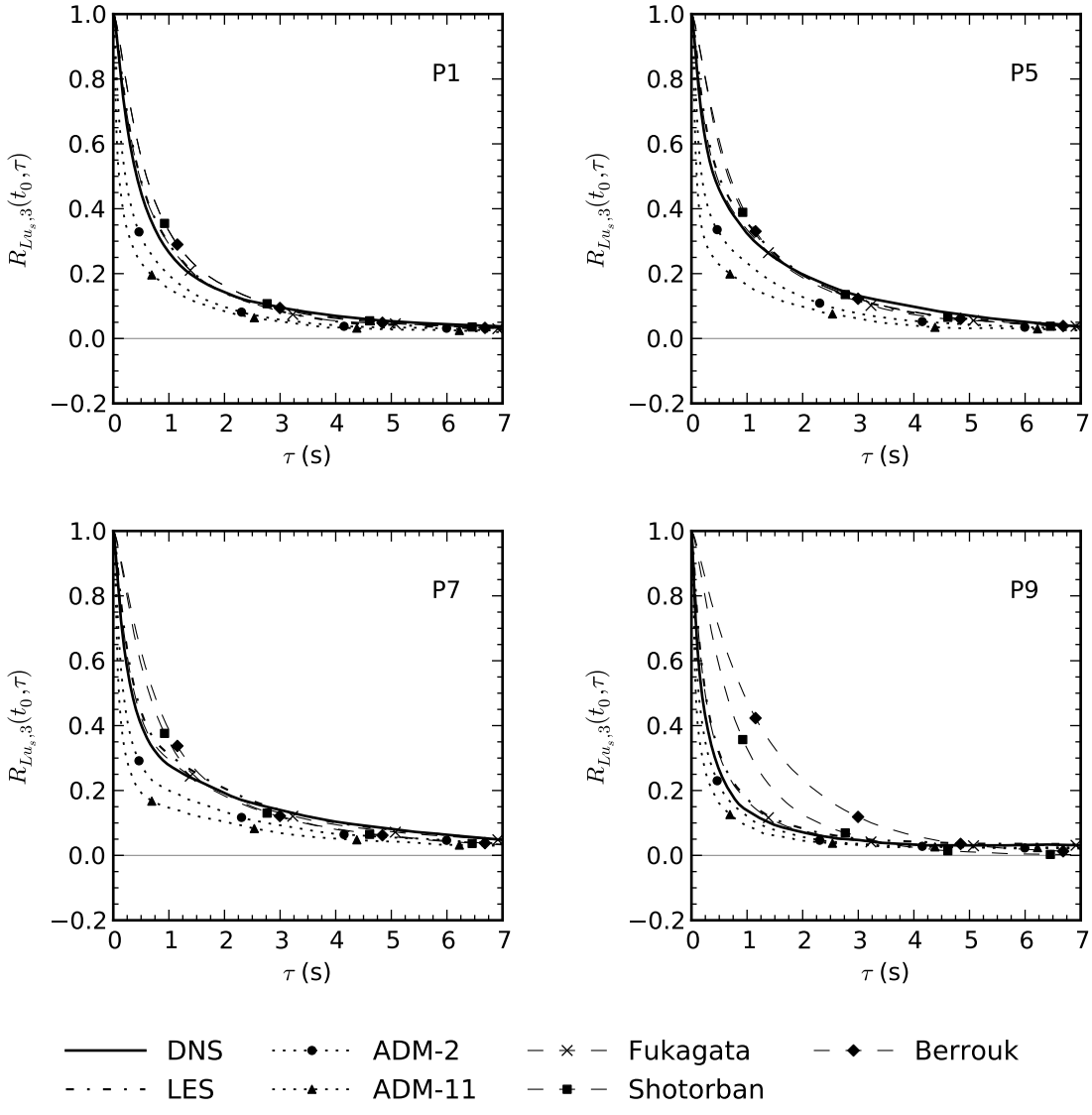

Figure 4.35: Lagrangian autocorrelation coefficient function of seen fluid velocity in direction x_3 along a particle's path, for various particle types with initial time $t = t_0$. *A posteriori* testing with filter size $\Delta = 8h_{DNS}$, standard model constants, and zero gravity.

The Lagrangian autocorrelation coefficient functions of the seen fluid velocity along a particle's path for various particle types are shown in Figure 4.35. The particle velocity Lagrangian autocorrelation coefficient functions are not shown since the differences between the *a posteriori* R_{Lp} and R_{Lu_s} results are minimal. The LES, ADM and model of Fukagata *et al.* (2004) Lagrangian autocorrelation functions are all reduced compared to the *a priori* tests. This is caused by the larger energy of the smallest resolved scales which act to randomize particle motion, and therefore contribute to particle velocities becoming uncorrelated in time. In particular, ADM has very large energy levels for wavenumbers near the cut-off, which results in ADM Lagrangian particle timescales that are much less than those of the DNS. Opposite to the other models, the *a posteriori* R_{Lp} and R_{Lu_s} functions from the models of Shotorban and Mashayek (2006) and Berrouk *et al.* (2007) are slightly increased relative to the *a priori* results. Although the increased energy of the small scales reduces the Lagrangian autocorrelation functions, the reduced SGS TKE increases the timescale $T^*_{L,sgs}$ and decreases the random component of the model. Both of these effects inhibit a particle from changing its velocity, and therefore increase both R_{Lp} and R_{Lu_s}.

The *a posteriori* particle dispersion as a function of Stokes number is plotted in Figure 4.36. The *a posteriori* LES and ADM particle dispersion results are less than the *a priori* results due to the reduced Lagrangian particle timescales. On the other hand, particle dispersion predicted by the models of Shotorban and Mashayek (2006) and Berrouk *et al.* (2007) is increased compared to the *a priori* tests. This is caused by the increased Lagrangian particle timescales for all particles, and the increased particle TKE for the larger particles.

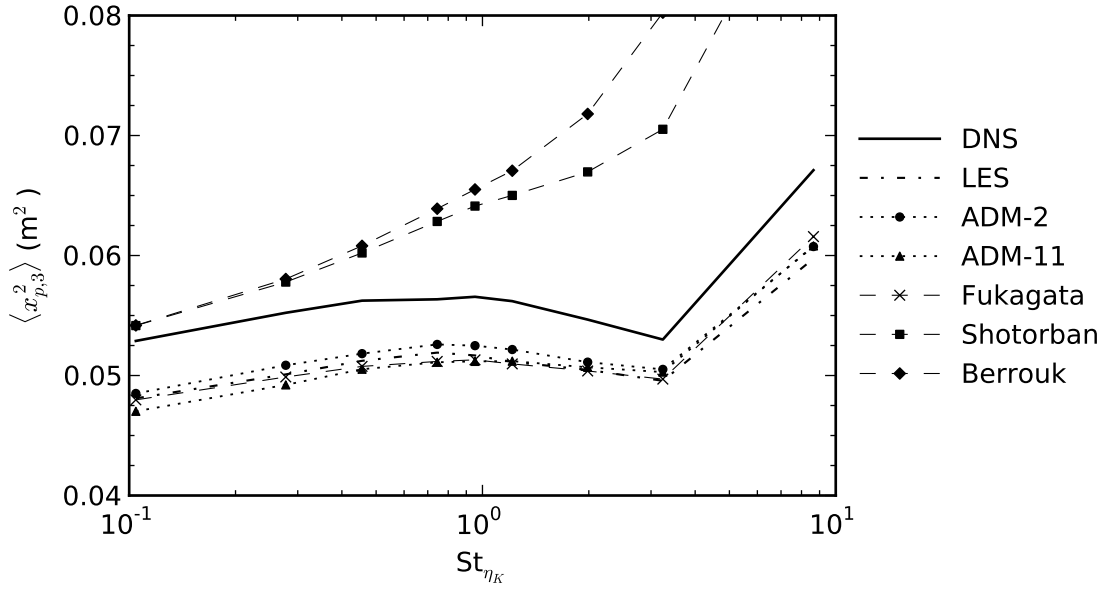

Figure 4.36: Particle mean square dispersion in direction x_3 at time $t = 4.0\,\mathrm{s}$. *A posteriori* testing with filter size $\Delta = 8h_{DNS}$, standard model constants, and zero gravity.

Figure 4.37 presents the *a posteriori* fractal dimension results. The fractal dimension plot reveals that the large particle results are similar for the *a posteriori* and *a priori* tests. Preferential concentration of large inertia particles is most influenced by the largest turbulent scales, and the FDNS and LES energy spectrum plots are very similar at the large scales. However, the FDNS and LES energy spectrum plots have significant discrepancies at scales near the cut-off. In the *a posteriori* tests the excess energy for the smallest resolved scales causes a significant increase in preferential concentration of the small and intermediate inertia particles for LES and ADM. ADM in particular exhibits very large amounts of particle clustering that are much greater than DNS for small and medium sized particles. As in the *a priori* testing, the stochastic models of Shotorban and Mashayek (2006) and Berrouk *et al.* (2007) predict zero particle clustering. However, the *a posteriori* results for the model of

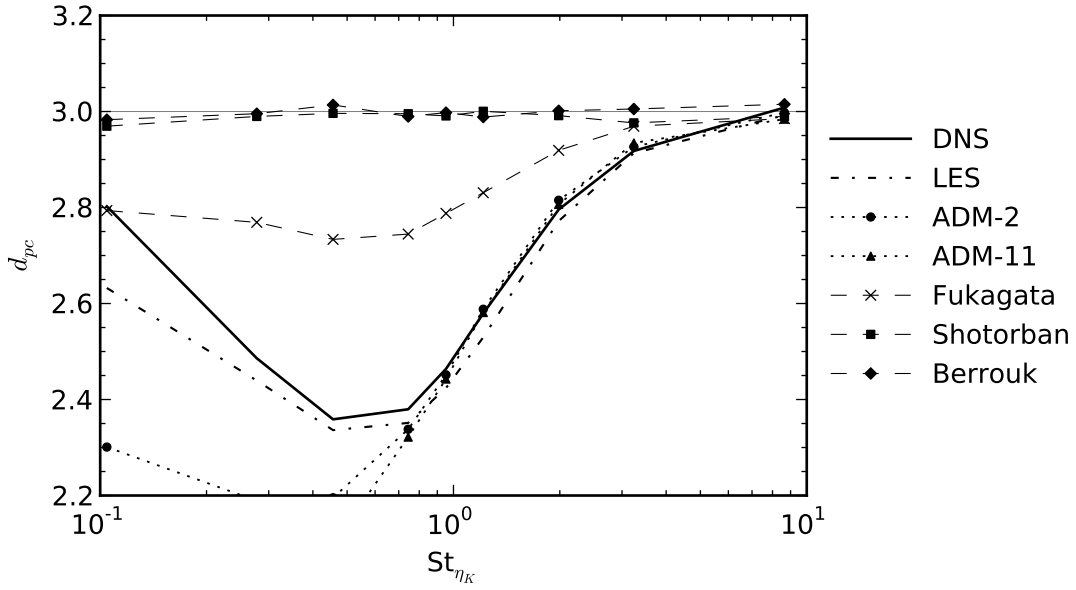

Figure 4.37: Fractal dimension at time $t = 4.0\,\mathrm{s}$. *A posteriori* testing with filter size $\Delta = 8h_{DNS}$, standard model constants, and zero gravity.

Fukagata *et al.* (2004) show some preferential concentration due to the combination of increased energy for scales near the cut-off, and the reduced SGS TKE.

It must be stressed that all of the particle LES resulted presented in this section are specific to the current LES fluid simulation. If a different fluid SGS model was used then the *a posteriori* results compared to the *a priori* results may have been quite different. The important conclusion to take away from these *a posteriori* tests is that the fluid SGS model can have just as significant of influence on the particle results as does the particle SGS model.

Chapter 5

Conclusions and Recommendations

5.1 Summary and conclusions

This research was focused on analyzing models that account for the influence of the subgrid scales on particles in LES of particle-laden turbulence. In Lagrangian particle modeling, particle trajectories are calculated by numerically solving the particle momentum equation. In order to evaluate the particle drag force, a solution to the turbulent flow field is required. Using LES to solve for the flow field in the modeling of particle-laden turbulence has many benefits compared to RANS or DNS. Since the large turbulent scales are resolved, LES with particles has the potential to yield superior particle statistics compared to RANS, including the ability to properly capture the interactions between particles and turbulent structures. Furthermore, the computational cost of LES is much less than that of DNS, such that LES can be used to solve for some flows of practical interest.

Previous researchers have shown that for many circumstances the effects of the SGS motions on particles in LES cannot be neglected. Particle SGS models introduce

additional modeling to account for the effects of SGS turbulent motions on particles. In this work several particle SGS models have been analyzed and tested. The approximate deconvolution method (ADM) is a mathematical technique that enhances scales larger than the LES grid. The stochastic models of Fukagata *et al.* (2004), Shotorban and Mashayek (2006) and Berrouk *et al.* (2007) model the SGS effects by introducing a random component.

The models were assessed using numerical simulations of inertial particles in a periodic box of homogeneous, isotropic turbulence. The turbulence had an initial Taylor scale Reynolds number of $\mathrm{Re}_\lambda = 74$ and decayed to a value of $\mathrm{Re}_\lambda = 39$ by the end of the simulations, which were performed on a 256^3 grid for the DNS. The particle SGS models were evaluated using both *a priori* and *a posteriori* methodologies, and the model results were compared to that of DNS and no model (FDNS or LES). A range of Stokes numbers were tested with and without gravity, and a variety of filer sizes and model constant values were used. The particle statistics used to analyze the models were particle and seen fluid turbulent kinetic energies, Lagrangian autocorrelation functions of particle velocity and seen fluid velocity, particle dispersion, and preferential concentration statistics.

The ADM results from the *a priori* tests were superior to the FDNS results for all particle statistics and Stokes numbers. However, the ADM results were unable to match the DNS. This behaviour of ADM yielding results between FDNS and DNS is because ADM is not capable of recovering all of the fluid SGS turbulent kinetic energy. This was clearly observed in the ADM energy spectra, which added energy to the resolved scales by moving towards a sharp spectral filter spectrum. However,

ADM cannot recreate scales that are smaller than the LES grid. Although the ADM-11 results were slightly superior to ADM-2, the ADM Van Cittert series truncation level did not significantly affect the ADM results.

Overall, the stochastic particle SGS model of Fukagata *et al.* (2004) did not necessarily improve particle results compared to the FDNS. The model of Fukagata *et al.* (2004) generally overpredicted particle turbulent kinetic energy and underpredicted the particle Lagrangian integral timescale, leading to a large range of dispersion results. The *a posteriori* results showed that the model is sensitive to the fluid SGS turbulent kinetic energy field.

The results from the model of Shotorban and Mashayek (2006) had good agreement with the DNS for particles with small relaxation times in the zero gravity *a priori* tests. However, the large inertia particles had too much turbulent kinetic energy and dispersion, likely due to the fluid particle assumptions. In the case of zero gravity, the only difference between the two models that are based on a Langevin equation is that the model of Berrouk *et al.* (2007) contains an additional timescale correction to account for particle inertia. As expected, the results of the small inertia particles were identical for the two models. The large inertia particle results were inferior for the model of Berrouk *et al.* (2007) compared to the model proposed by Shotorban and Mashayek (2006), indicating that the particle inertia correction worsened particle results. It is possible that the particle inertia correction could be improved using a different value of the model constant β.

The FDNS was able to partially predict preferential concentration. As previously observed by Ray and Collins (2011), filtering decreased particle clustering at low Stokes numbers and increased particle clustering at high Stokes numbers. ADM was

able to improve preferential concentration results for all Stokes numbers, but could not equal the results of the DNS. All three of the stochastic models predicted zero particle clustering for almost all cases, and therefore performed much worse than the FDNS. This was caused by the random component of the stochastic models, which smooths particle distributions. This is a highly undesirable result since one of the major motivations for LES with particles is the ability to capture the interactions between particles and turbulent structures, but the random contribution inhibits the ability of the stochastic models to account for these interactions.

A priori tests with gravity were conducted to evaluate the ability of the particle SGS models to capture the crossing trajectory and continuity effects. The DNS results clearly demonstrated the influence of these effects on particle dispersion and on the Lagrangian autocorrelation functions. The FDNS and all of the particle SGS models showed some ability to account for these effects since in LES the large eddies are directly represented. Compared to the model of Shotorban and Mashayek (2006), the model of Berrouk *et al.* (2007) showed good ability to account for the crossing trajectory and continuity effects.

The filter size tests showed that the stochastic models have the capability to recover the correct amount of turbulent kinetic energy for any filter size, whereas ADM cannot recover sufficient turbulent kinetic energy for large filter sizes. All of the particle SGS models, including FDNS, generally performed very well for the smallest filter size, but model errors became larger as less energy was resolved. Particle dispersion decreased with filter size for FDNS, ADM and the model of Fukagata *et al.* (2004), but the opposite trend existed for the models of Shotorban and Mashayek (2006) and Berrouk *et al.* (2007).

Calculation of the Langevin model constant (C_0) and LES dissipation coefficient (C_ϵ) directly from the DNS and FDNS yielded a large range of values, which were dependent on the amount of resolved energy. The standard values for both constants were within the calculated range. The particle results from the model of Fukagata *et al.* (2004) were independent of the model constant values. Analysis revealed that the SGS Lagrangian timescale has minimal effect on the model of Fukagata *et al.* (2004) for reasonable simulation and particle parameters. For the models of Shotorban and Mashayek (2006) and Berrouk *et al.* (2007), the analytical work showed that increasing the value of either constant increases the SGS Lagrangian timescale and decreases the random component. Increasing these constants resulted in reduced particle dispersion for both models. For the specific simulations in this thesis, the largest model constant values tested ($C_0 = 3.2$ and $C_\epsilon = 1.4$) performed best. Overall, the results from the two models were not very sensitive to the constant values.

The *a posteriori* particle results had significant errors resulting from discrepancies between the LES and FDNS fluid fields. The differences between the LES and FDNS velocity fields were primarily due to fluid SGS modeling errors. If a different fluid SGS model was used then the particle results could be quite different. Therefore, conclusions regarding the particle SGS models from the *a posteriori* tests should not be considered to be universal. Instead, the important conclusion to take from the *a posteriori* tests is that in a real LES of particle-laden turbulence, the particle results can be affected significantly by both the particle and fluid SGS models.

5.2 Recommendations for future work

Based on the results and conclusions of this research, the recommendations for future work are as follows. The most important recommendation is for particle SGS models to be developed that are capable of recovering sufficient SGS turbulent kinetic energy, and can properly account for the interactions between particles and turbulent structures. ADM is only able to recover a portion of the SGS energy, and the interactions between particles and turbulent structures cannot be properly accounted for using stochastic models that treat the SGS field as white noise. Particle SGS models that allow particles to see a SGS fluid field with an underlying structure, similar to the model of Khan *et al.* (2010), should be investigated. Development of such models should focus on the physics of the subgrid scales.

The stochastic models tested in this thesis could be improved by investigating different modeling techniques for the parameters k_{sgs}, ϵ_{sgs} and $T^*_{L,sgs}$. Without changing their formulation, the stochastic models may be improved by altering the methods used to evaluate these variables. For example, using a transport equation for k_{sgs} may prove to be superior to the method based on the dynamic Smagorinsky fluid SGS model.

Additional testing of the model proposed by Berrouk *et al.* (2007) should be done using range of β values, with and without gravity. The model showed good ability to account for the crossing trajectory and continuity effects, but suffered a loss of accuracy at high Stokes numbers due to the particle inertia correction. The particle inertia correction may be substantially improved using a different value of β.

The particle SGS models should be tested for a variety of other conditions not considered in this research, such as inhomogeneous and anisotropic turbulent flows with

more complex geometries. Also, particles with lower density ratios such that other particle forces are important, and less dilute flows in which turbulence modulation and particle-particle collisions are important should be examined. Lastly, additional *a posteriori* tests using different fluid SGS models should be conducted.

Finally, it is recommended that any future simulations of isotropic turbulence in a box should be forced to avoid the numerous complications associated with decaying turbulence. Although forcing introduces some artificiality, this should not be an issue if there is a large separation between the large and small scales, and it is scales in the inertial subrange and smaller that are of primary interest.

Appendix A

ADM Theory

The concept of the approximate deconvolution method (ADM) is to obtain the correct velocity field by defiltering the LES fluid field. Filtering is defined as the convolution of a function $f(x)$ with a filter kernel G:

$$\widetilde{f}(x) = \int_{-\infty}^{\infty} G(r) f(x-r) dr \tag{A.1}$$

If the filter kernel G has an inverse filter kernel G^{-1}, then a deconvolution can be performed (Stolz *et al.*, 2001). The deconvolution is defined as:

$$f(x) = \int_{-\infty}^{\infty} G^{-1}(r) \widetilde{f}(x-r) dr = G^{-1} * \widetilde{f}(x) \tag{A.2}$$

The inverse filter kernel is often approximated using a truncated Van Cittert series expansion (Van Cittert, 1931):

$$G^{-1} = \sum_{\alpha=0}^{m} (1-G)^{\alpha} \tag{A.3}$$

where m is the truncation level (a non-truncated Van Cittert series has $m \to \infty$).

In general, if an inverse filter kernel exists then a convolution is fully invertible. However, this requires that $f(x)$ be filtered continuously with respect to x so that the filtered function, $\widetilde{f}(x)$, is continuous. If the filtered function is projected onto a grid, which is the case in LES, then the filtered function is not formally invertible since information is fundamentally lost. This is why ADM is not capable of recovering the correct unfiltered fluid field.

A simple one-dimensional example is used to demonstrate why ADM is unable to recover the correct unfiltered function. The function $y = sin(x)$ was computed on a very fine grid, such that it can be considered to be almost continuous. The function was filtered using a top-hat filter with a width of $\Delta = \pi$, and ADM was performed using a truncated Van Cittert series expansion with $m = 20$ to ensure that the truncation would not affect any results. The filtering and ADM were carried out using a coarse grid and a fine grid. The coarse grid had a grid spacing of $\Delta x = 0.25\pi$, and the fine grid had the same grid spacing as the original function $y = sin(x)$. The results of both are shown in Figure A.1 and Figure A.2, where y^* is the ADM result. Figure A.1 shows that using the coarse grid ADM is unable to correctly reproduce the original function. However, Figure A.2 shows that ADM performed on the fine grid perfectly reproduces the original function (the y and y^* lines are coincident).

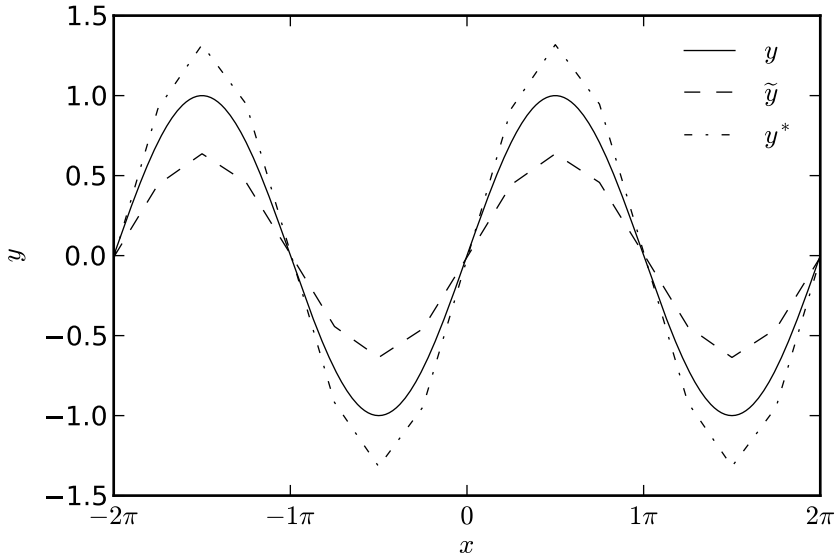

Figure A.1: Filtering and ADM of the function $y = sin(x)$ on a coarse grid. The variable y is the original unfiltered function, $\widetilde{y}$ is the filtered function, and y^* is the approximation of y from ADM.

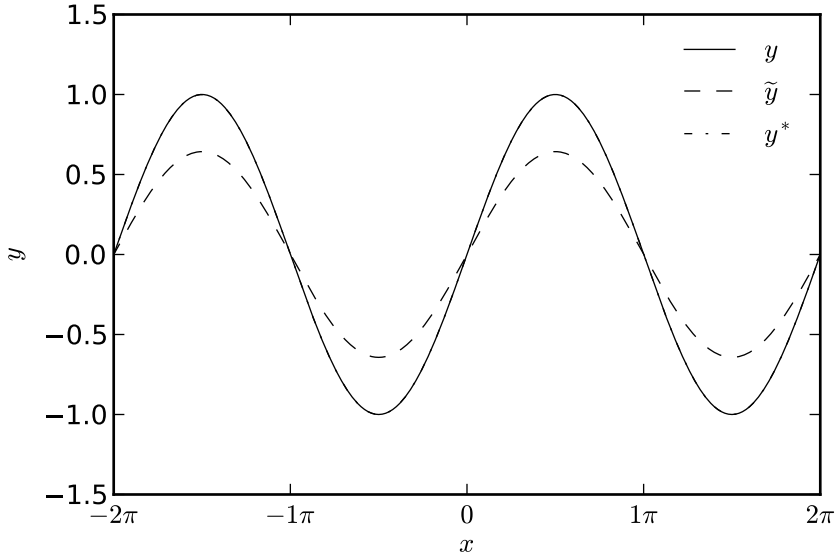

Figure A.2: Filtering and ADM of the function $y = sin(x)$ on a fine grid. The variable y is the original unfiltered function, $\widetilde{y}$ is the filtered function, and y^* is the approximation of y from ADM.

Appendix B

DNS Fluid Results and Validation

The fluid results of the DNS are presented in this appendix. As discussed in Section 3.2.2, the initial velocity field is generated using a spectral method that creates a periodic box of isotropic turbulence. The simulation is then advanced in time until an acceptable turbulent kinetic energy spectrum is obtained. This velocity field is then used as the initial DNS fluid field ($t = 0$), and the simulation is run for $7.5s$.

The evolution of the turbulent kinetic energy spectrum is shown in Figure B.1. For comparison, a line proportional to $\kappa^{-5/3}$ is also plotted, which according to Kolmogorov's five-thirds power law should be the slope of the energy spectrum in the inertial subrange (Pope, 2000). As the turbulence decays the turbulent kinetic energy decreases, the range of turbulent scales is reduced, and the inertial subrange becomes smaller.

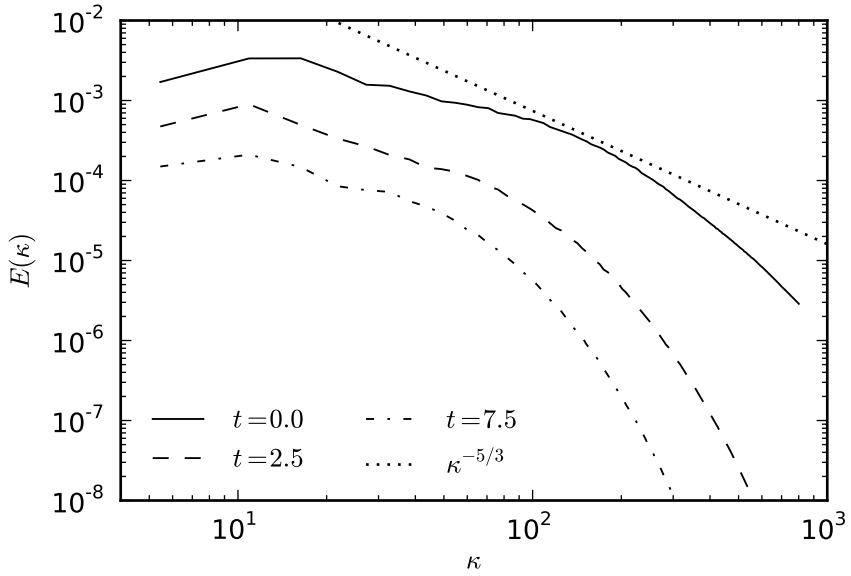

Figure B.1: Turbulent kinetic energy spectrum of the DNS fluid field.

The time development of the turbulent kinetic energy and dissipation rate are shown in Figure B.2. These quantities are calculated directly from the velocity field using:

$$k = \left\langle \frac{1}{2} u'_{f,i} u'_{f,i} \right\rangle \tag{B.1}$$

$$\epsilon = 2\nu \left\langle S_{ij} S_{ij} \right\rangle \tag{B.2}$$

The strain rate is given by:

$$S_{ij} = \frac{1}{2}\left(\frac{\partial u_{f,i}}{\partial x_j} + \frac{\partial u_{f,j}}{\partial x_i} \right) \tag{B.3}$$

The turbulent kinetic energy and rate of decay were compared with analytical relationships for decaying turbulence. The agreement between the analytical and DNS was excellent, as shown in Figure B.2, and the decay exponent was within the range of reported experimental values for grid generated turbulence. The RMS turbulent

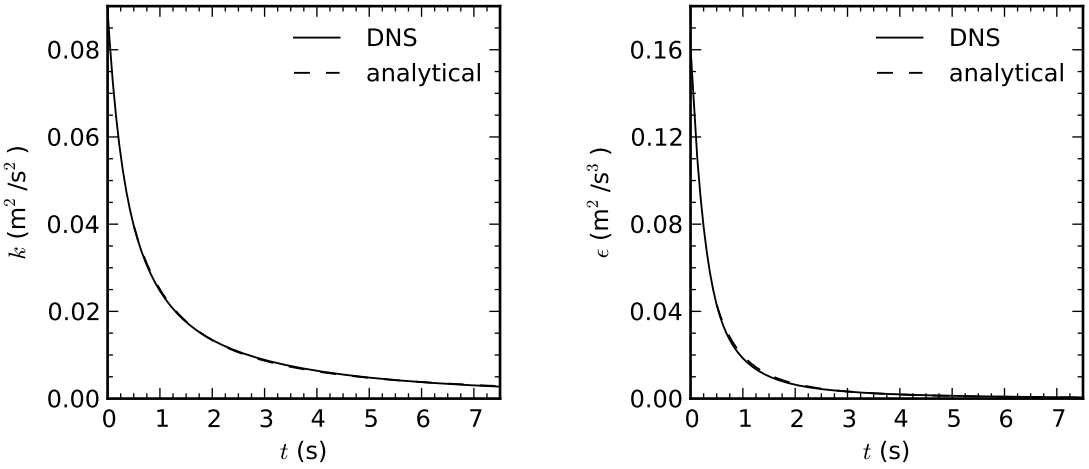

Figure B.2: Time development of the fluid turbulent kinetic energy (left) and dissipation rate (right) of the DNS fluid field. The analytical solutions are also included.

velocity fluctuations in the three principal directions are presented in Figure B.3.

Based on the turbulent kinetic energy and the decay rate, the Taylor microscale and Reynolds number can be calculated.

$$\lambda = \sqrt{\frac{15\nu(u'_{rms})^2}{\epsilon}} \tag{B.4}$$

$$\mathrm{Re}_\lambda = \frac{u'_{rms}\lambda}{\nu} \tag{B.5}$$

The evolution of the Taylor-scale Reynolds number is shown in Figure B.4.

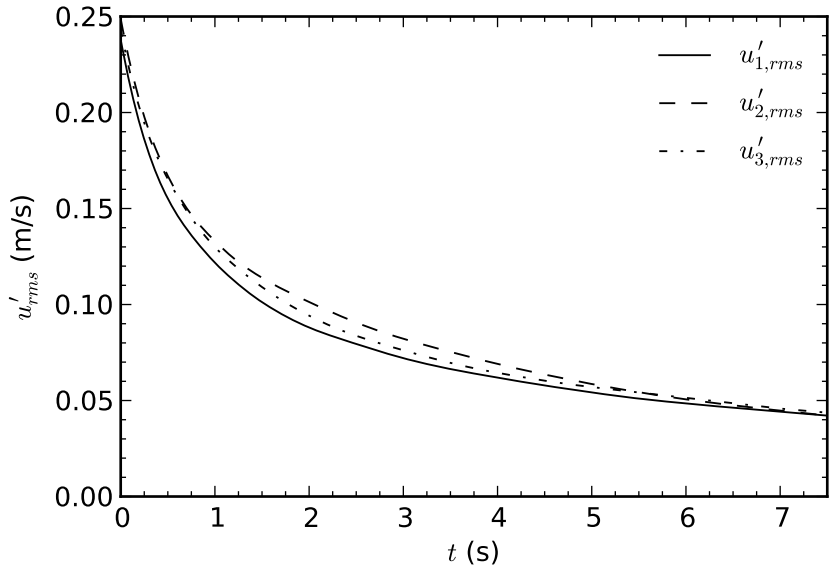

Figure B.3: Time development of the fluid RMS turbulent velocity components of the DNS fluid field.

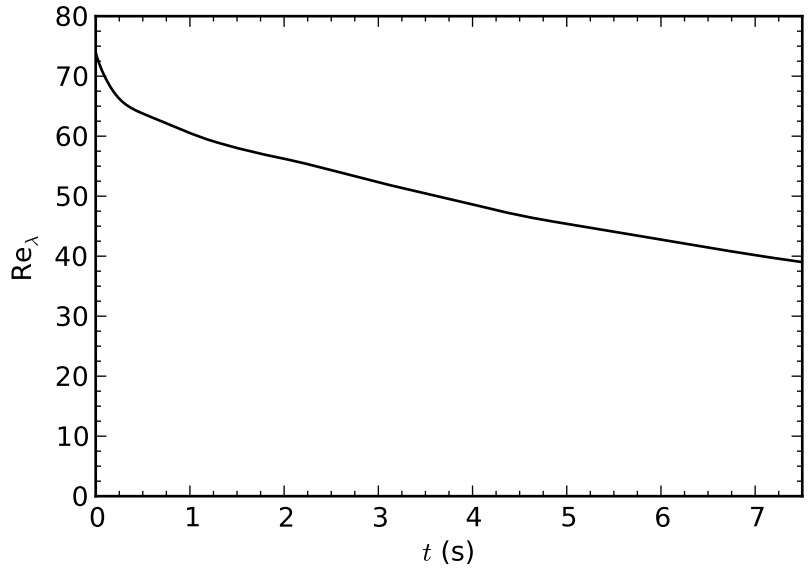

Figure B.4: Time development of the Taylor microscale Reynolds number of the DNS fluid field.

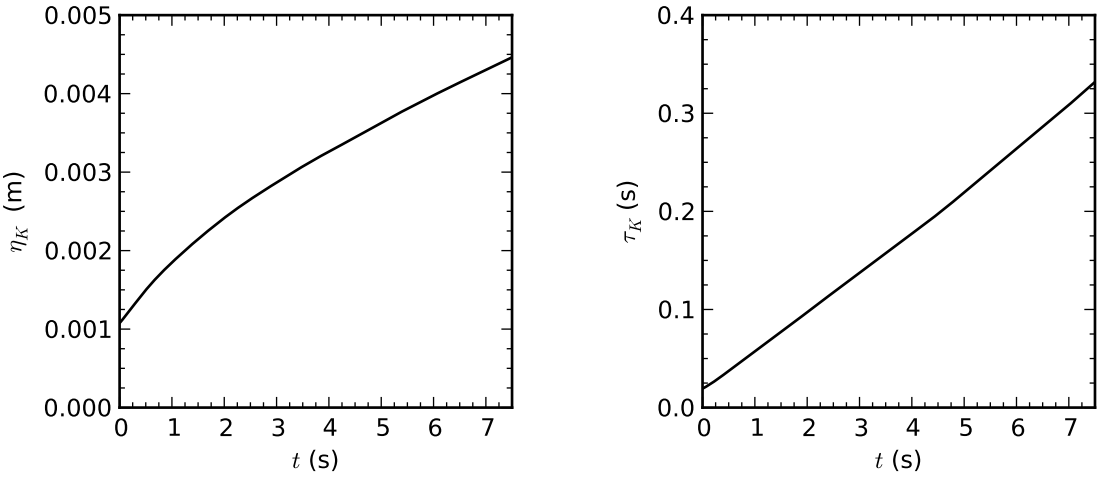

Figure B.5: Time development of the Kolmogorov length and time scales of the DNS fluid field.

The Kolmogorov length and time scales are plotted in Figure B.5. They are calculated from the dissipation rate and kinematic viscosity.

$$\eta_K = \left(\frac{\nu^3}{\epsilon}\right)^{1/4} \qquad \tau_K = \left(\frac{\nu}{\epsilon}\right)^{1/2} \tag{B.6}$$

To properly perform a DNS the smallest turbulent scales must be adequately resolved. The general consensus in the literature is that sufficient spatial resolution is achieved if $\kappa_{max}\eta_K \geq 1.0$ (Yeung and Pope, 1988). As shown in Figure B.6, the initial value of $\kappa_{max}\eta_K$ was 0.87, and $\kappa_{max}\eta_K = 1.0$ occurred at $t = 0.1995\,\mathrm{s}$. It is acceptable that $\kappa_{max}\eta_K < 1.0$ at very early times since particle statistics are not considered until $t = 0.5\,\mathrm{s}$, and it is desired that the Reynolds number be maximized during the particle simulations.

The temporal resolution was determined to be sufficient by performing timestep independence tests for early simulation times. The timestep independence test results are shown in Figure B.7. The results are presented using the dissipation rate since

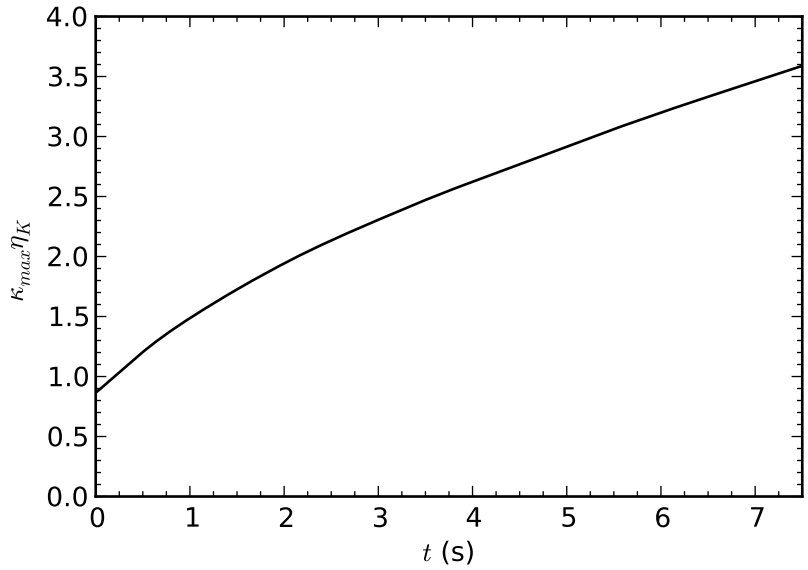

Figure B.6: Time development of the DNS spatial resolution.

compared to other fluid statistics, ϵ was found to be sensitive to the value of Δt. Figure B.7 shows that the $\Delta t = 0.000250\,\mathrm{s}$ and $\Delta t = 0.000125\,\mathrm{s}$ results are identical.

Figure B.8 presents the Eulerian integral length and timescales, which are calculated as:

$$L_{ii} = \int_0^\infty \frac{\left\langle u_{f,i}(\vec{x} + \vec{e_i} \cdot r) u_{f,i}(\vec{x}) \right\rangle}{\left\langle u_{f,i}^2 \right\rangle} dr \tag{B.7}$$

$$L_{E,f} = (L_{11} + L_{22} + L_{33})/3 \tag{B.8}$$

$$T_{E,f} = \frac{L_{E,f}}{u'_{rms}} \tag{B.9}$$

where $\vec{e_i}$ is a unit vector in the direction i. The Eulerian integral length scale ($L_{E,f}$) is taken to be the average of the three longitudinal integral length scales (L_{ii}). For DNS of turbulence in a box it must be ensured that the computational box is large enough to properly represent the energy containing eddies. There is a lack of consensus in the literature as to how large the domain should be, but Pope (2000) recommends

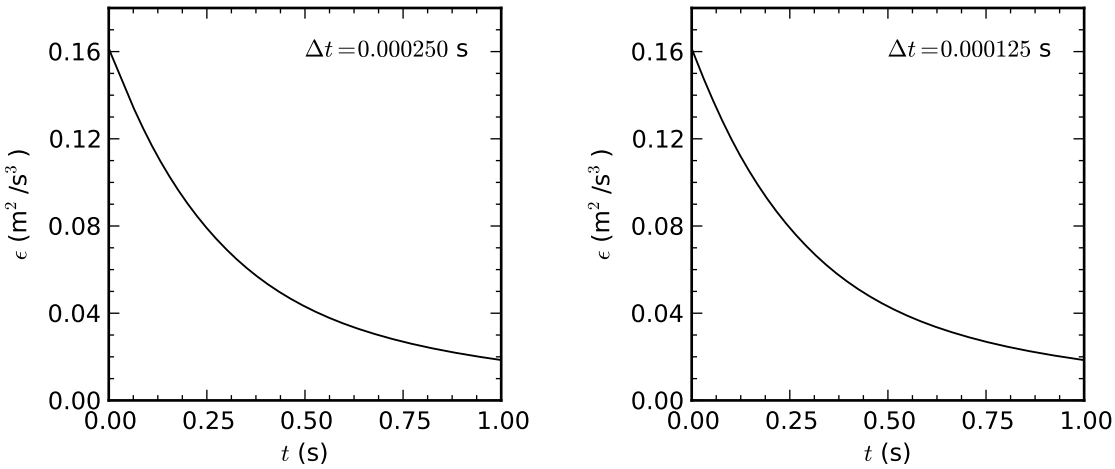

Figure B.7: DNS timestep independence test.

$L_0/L_{E,f} \geq 8$. For decaying turbulence the larger scales grow in time, and therefore it can be difficult to maintain $L_0/L_{E,f} \geq 8$ at long times. In the current DNS $L_0/L_{E,f} = 11.49 \rightarrow 6.58$.

The skewness of the streamwise velocity derivative (S_u) is used to determine if the turbulence is fully developed.

$$S_u = \frac{\left[-\frac{1}{3} \sum_{i=1}^{3} \left\langle \left(\frac{\partial u_{f,i}}{\partial x_i} \right)^3 \right\rangle \right]}{\left[\frac{1}{3} \sum_{i=1}^{3} \left\langle \left(\frac{\partial u_{f,i}}{\partial x_i} \right)^2 \right\rangle \right]^{3/2}} \tag{B.10}$$

Tavoularis *et al.* (1978) compiled the results of many studies and found that S_u is dependent on Reynolds number. For the range of Reynolds numbers in this DNS the skewness of the streamwise velocity derivative should be between 0.33 and 0.52. As shown in Figure B.9, during the simulation S_u has a relatively constant value of 0.50, indicating that the turbulence is fully developed. This also ensures that the solution

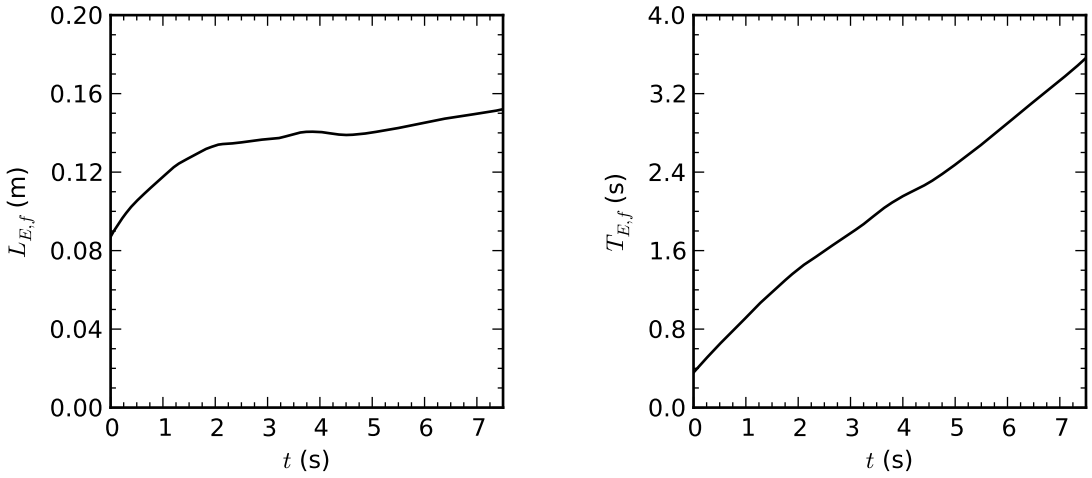

Figure B.8: Time development of the fluid Eulerian integral length and time scales of the DNS fluid field.

to the Navier-Stokes equations is appropriate, and does not contain any artificial characteristics due to the original generated velocity field.

For the present work it is desired that the turbulence be isotropic. This is measured using the anisotropic tensor, which is plotted in Figure B.10.

$$B_{ij} = \frac{u_{f,i}u_{f,j}}{u_{f,k}u_{f,k}} - \frac{1}{3}\delta_{ij} \tag{B.11}$$

In a perfectly isotropic flow field, all elements of the anisotropic tensor would be zero. Figure B.10 shows that all components of the anisotropic tensor are less than 5% throughout the entire DNS. Some anisotropy can also be observed in Figure B.3, which shows that the turbulent velocity fluctuations in three principal directions are not identical. These deviations from isotropy are acceptable since they are sufficiently small, but they should be considered when analysing the particle results.

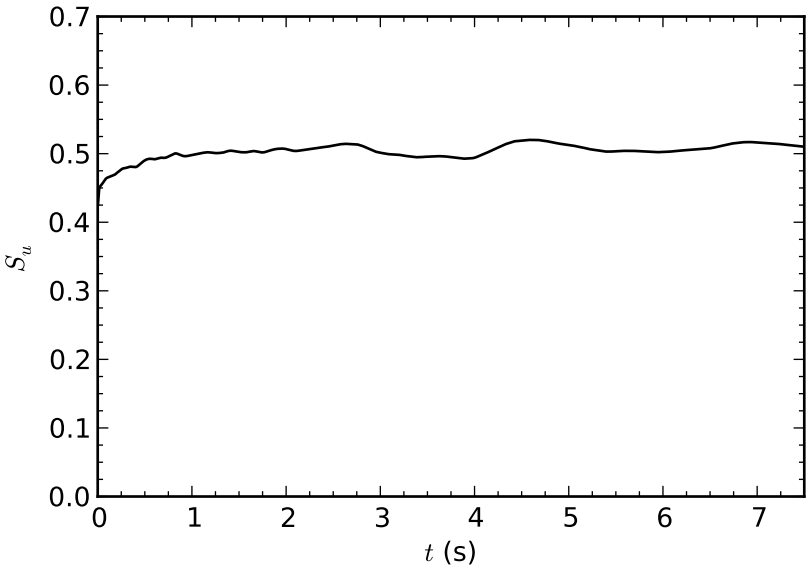

Figure B.9: Time development of the skewness of the fluid velocity derivative in the streamwise direction of the DNS fluid field.

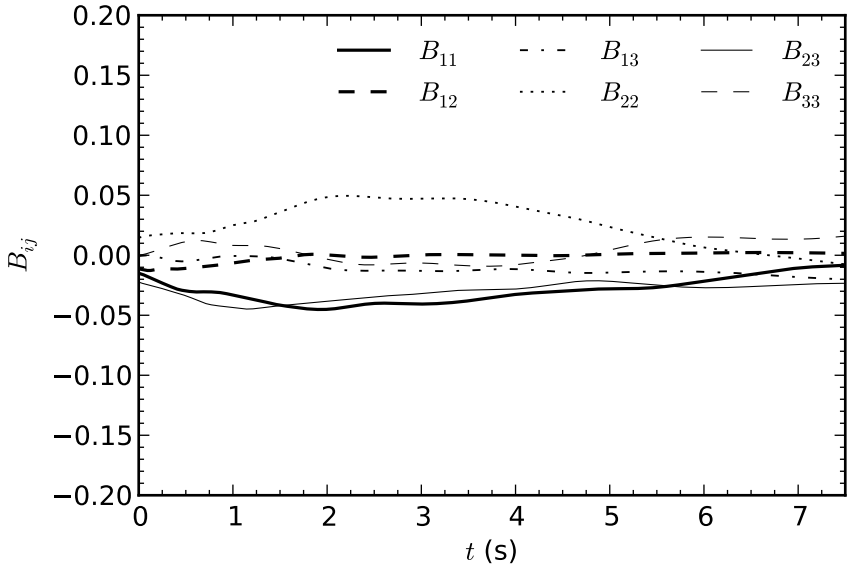

Figure B.10: Time development of the anisotropic tensor components of the DNS fluid field.

Appendix C

Particle Independence Tests

The number of particles and particle timestep independence tests are presented in this appendix using the particle diffusivity results. Many different particle statistics were examined, but the particle dispersion rates showed the most sensitivity to Δt and N_p.

The independence tests for the number of particles were done using the DNS and FDNS ($\Delta = 16h_{DNS}$) flow fields with and without gravity. Figure C.1 shows that the $N_p = 262,144$ and $N_p = 512,000$ DNS results are identical, as are the FDNS results. Gravity did not influence the number of particles required for independence. However, filtering was found to decrease the number of particles required for independence.

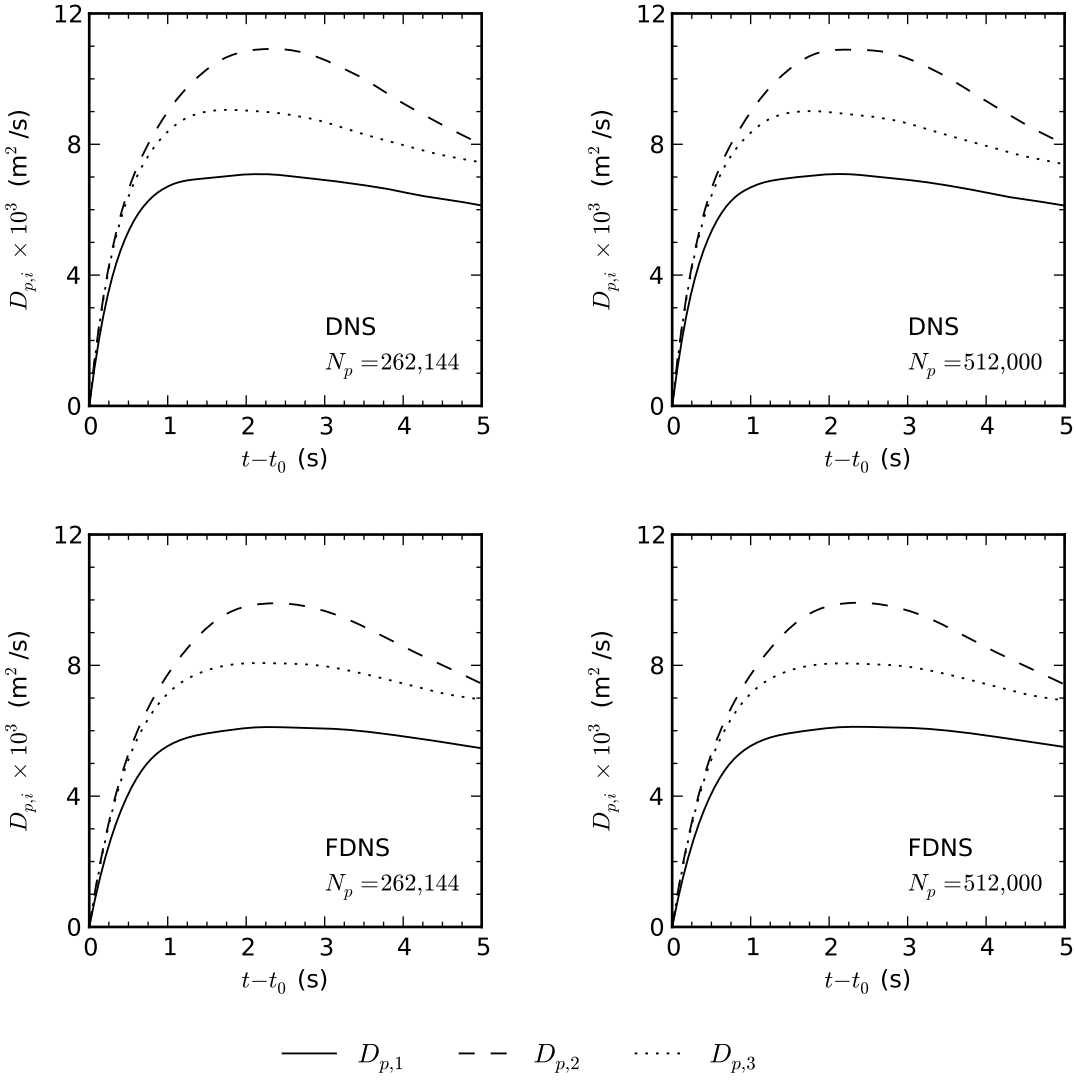

Figure C.1: Particle number independence tests for particle type P5 in the DNS and FDNS flow fields with zero gravity. The FDNS flow field has a filter size of $\Delta = 16h_{DNS}$.

The particle timestep independence tests were conducted with slightly different particle parameters than those listed in Table 3.2, but a large range of Stokes numbers were considered. The particle timestep independence test results are plotted in Figure C.2, which shows that the $\Delta t = 0.00025\,\mathrm{s}$ and $\Delta t = 0.00100\,\mathrm{s}$ results are identical. Including gravity did not effect the value of the particle timestep required for independence.

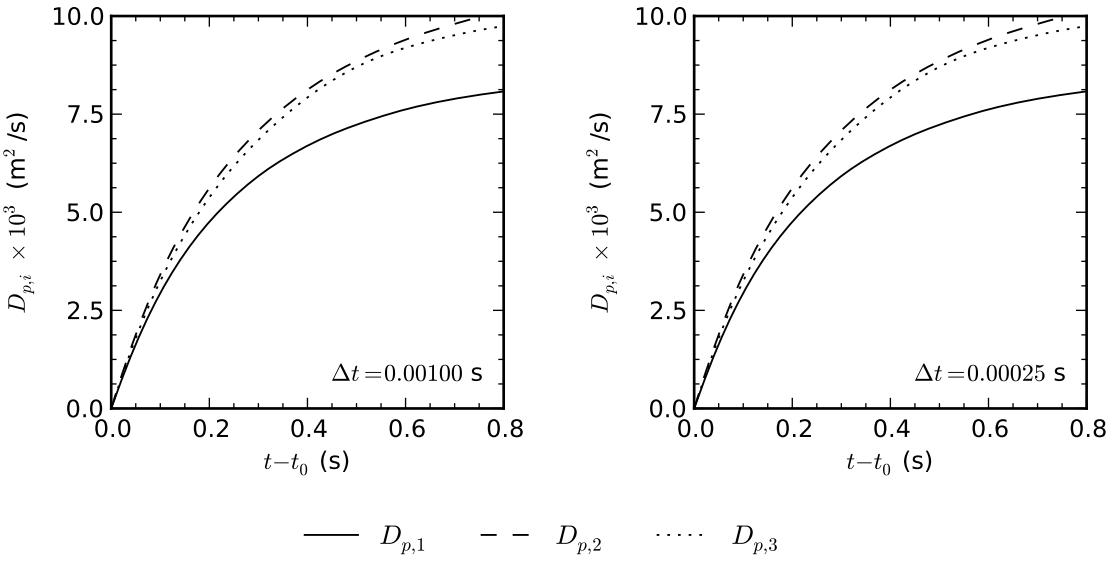

Figure C.2: Particle timestep independence tests for the DNS with zero gravity. These results are for particles with Stokes number $\mathrm{St}_{\eta_K} = 1.44$ at time $t = t_0$.

Bibliography

Amiri, A. E. and Hannani, S. K. (2006). Large-eddy simulation of heavy-particle transport in turbulent channel flow. *Num. Heat Trans. B*, **50**, 285–313.

Anand, M. and Pope, S. (1985). Diffusion behind a line source in grid turbulence. *Turbulent Shear Flows*, **4**, 1–16.

Armenio, V. and Fiorotto, V. (2001). The importance of forces acting on particles in turbulent flows. *Phys. Fluids*, **13**, 2437–2440.

Armenio, V., Piomelli, U., and Fiorotto, V. (1999). Effect of the subgrid scales on particle motion. *Phys. Fluids*, **11**, 3030–3042.

Baba-Ahmadi, M. and Tabor, G. (2008). Inlet conditions for large eddy simulation of gas-turbine swirl injectors. *AIAA J.*, **46**, 1782–1790.

Berrouk, A. and Laurence, D. (2008). Stochastic modelling of aerosol deposition for les of 90 degree bend turbulent flow. *Intl J. Heat Fluid Flow*, **29**, 1010–1028.

Berrouk, A., Laurence, D., Riley, J., and Stock, D. (2007). Stochastic modelling of inertial particle dispersion by subgrid motion for LES of high Reynolds number pipe flow. *J. Turbulence*, **8**(50), 1–20.

Berrouk, A., Stock, D., Laurence, D., and Riley, J. (2008). Heavy particle dispersion from a point source in turbulent pipe flow. *Intl J. Multiphase Flow*, **34**, 916–923.

Bini, M. and Jones, W. (2007). Particle acceleration in turbulent flows: A class of nonlinear stochastic models for intermittency. *Phys. Fluids*, **19**, 035104–035104–9.

Box, G. and Muller, M. (1958). A note on the generation of random normal deviates. *Ann. Math. Stat.*, **29**, 610–611.

Clift, R., Grace, J., and Weber, M. (1978). *Bubbles, Drops and Particles*. Academic Press.

Csanady, G. (1963). Turbulent diffusion of heavy particles in the atmosphere. *J. Atmos. Sci.*, **20**, 201–208.

Deardorff, J. (1973). The use of subgrid transport equations in a three-dimensional model of atmospheric turbulence. *J. Fluids Engineering*, **95**, 429–438.

Eaton, J. and Fessler, J. (1994). Preferential concentration of particles by turbulence. *Intl J. Multiphase Flow*, **20**, 169–209.

Elghobashi, S. and Truesdell, G. (1992). Direct simulation of particle dispersion in a decaying isotropic turbulence. *J. Fluid Mech.*, **242**, 655–700.

Fede, P. and Simonin, O. (2006). Numerical study of the subgrid fluid turbulence effects on the statistics of heavy colliding particles. *Phys. Fluids*, **18**, 045103–045103–17.

Fede, P., Simonin, O., Villedieu, P., and Squires, K. (2006). Stochastic modeling of the turbulent subgrid fluid velocity along inertial particle trajectories. *Proceedings of the Summer Program, Center for Turbulence Research*, pages 247–258.

Fukagata, K., Zahrai, S., and Bark, F. (2004). Dynamics of Brownian particles in a turbulent channel flow. *Heat Mass Transfer*, **40**, 715–726.

Fung, J., Hunt, J., Malik, N., and Perkins, R. (2006). Kinematic simulation of homogeneous turbulence by unsteady random Fourier modes. *J. Fluid Mech.*, **236**, 281–318.

Germano, M., Piomelli, U., Moin, P., and Cabot, W. (1991). A dynamic subgrid-scale eddy viscosity model. *Phys. Fluids A*, **3**, 1760–1765.

Geurts, B. (2004). *Elements of direct and large-eddy simulation*. Edwards.

Gicquel, L., Givi, P., Jaberi, F., and Pope, S. (2002). Velocity filtered density function for large eddy simulation of turbulent flows. *Phys. Fluids*, **14**, 1196–1213.

Gobert, C. (2010). Analytical assessment of models for large eddy simulation of particle laden flow. *J. Turbulence*, **11**(23), 1–24.

Gobert, C. and Manhart, M. (2010). A priori and a posteriori analysis of models for large-eddy simulation of particle-laden flow. *Phys. Flu-Dyn.*, **1004**(5598), 1–18.

Gobert, C. and Manhart, M. (2011). Subgrid modelling for particle-LES by Spectrally Optimised Interpolation (SOI). *J. Comp. Phys.*, **230**, 7796–7820.

Heinz, S. (2003). On Fokker-Planck equations for turbulent reacting flows. Part 2. Filter density function for large eddy simulation. *Flow Turbul. Combust.*, **70**, 153–181.

Issa, R. (1986). Solution of the implicitly discretised fluid flow equations by operator-splitting. *J. Comp. Phys.*, **62**, 40–65.

Jin, G., He, G., Wang, L., and Zhang, J. (2010). Subgrid scale fluid velocity timescales seen by inertial particles in large-eddy simulation of particle-laden turbulence. *Intl J. Multiphase Flow*, **36**, 432–437.

Khan, M., Luo, X., Nicolleau, F., Tucker, P., and Iacono, G. (2010). Effects of LES sub-grid flow structure on particle deposition in a plane channel with a ribbed wall. *Intl J. Numer. Meth. Biomed. Engng.*, **26**, 999–1015.

Kloeden, P. and Platen, E. (1992). *Numerical Solution of Stochastic Differential Equations*. Springer.

Kuerten, J. (2006). Subgrid modeling in particle-laden channel flow. *Phys. Fluids*, **18**, 025108–025108–13.

Kuerten, J. and Vreman, A. (2005). Can turbophoresis be predicted by large-eddy simulation. *Phys. Fluids*, **17**, 011701–011701–4.

Lilly, D. (1992). A proposed modification of the Germano subgrid-scale closure method. *Phys. Fluids A*, **4**, 633–635.

Macpherson, G., Nordin, N., and Weller, H. (2009). Particle tracking in unstructured, arbitrary polyhedral meshes for use in CFD and molecular dynamics. *Commun. Numer. Meth. Engng.*, **26**, 263–273.

Maxey, M. and Riley, J. (1983). Equation of motion for a small rigid sphere in a nonuniform flow. *Phys. Fluids*, **26**, 883–889.

Meneveau, C. and O'Neil, J. (1994). Scaling laws of the dissipation rate of turbulent subgrid-scale kinetic energy. *Phys. Rev. E*, **49**, 2866–2874.

Minier, J. and Peirano, E. (2001). The PDF approach to turbulent polydispersed two-phase flows. *Phys. Reports*, **352**, 1–214.

Moin, P., Squires, K., Cabot, W., and Lee, S. (1991). A dynamic subgrid-scale model for compressible turbulence and scalar transport. *Phys. Fluids A*, **3**, 2746–2757.

Nilsson, H. (2007). Some experiences on the accuracy and parallel performance of OpenFOAM for CFD in water turbines. In *Applied Parallel Computing. State of the Art in Scientific Computing*, volume 4699 of *Lecture Notes in Computer Science*, pages 168–176. Springer Berlin Heidelberg.

OpenFOAM Foundation (2011). *OpenFOAM User Guide*, 2.1.1 edition.

Pope, S. (1994). Lagrangian PDF methods for turbulent flows. *Annu. Rev. Fluid Mech.*, **26**, 23–63.

Pope, S. (2000). *Turbulent Flows*. Cambridge University Press.

Pozorski, J. and Apte, S. (2009). Filtered particle tracking in isotropic turbulence and stochastic modeling of subgrid-scale dispersion. *Intl J. Multiphase Flow*, **35**, 118–128.

Ray, B. and Collins, L. (2011). Preferential concentration and relative velocity statistics of inertial particles in Navier-Stokes turbulence with and without filtering. *J. Fluid Mech.*, **680**, 488–510.

Reeks, M. (1991). On a kinetic equation for the transport of particles in turbulent flows. *Phys. Fluids A*, **3**, 446–456.

Renze, P., Heinen, K., and Schonherr, M. (2011). Experimental and numerical investigation of pressure swirl atomizers. *Chem. Eng. Technol.*, **34**, 1191–1198.

Riley, J. and Patterson, G. (1974). Diffusion experiments with numerically integrated isotropic turbulence. *Phys. Fluids*, **17**, 292–297.

Selma, B., Bannari, R., and Proulx, P. (2010). A full integration of a dispersion and interface closures in the standard k-ϵ model of turbulence. *Chem. Eng. Sci.*, **65**, 5417–5428.

Shirolkar, J., Coimbra, C., and McQuay, M. (1996). Fundamental aspects of modeling turbulent particle dispersion in dilute flows. *Prog. Energy Combust. Sci.*, **22**, 363–399.

Shotorban, B. and Mashayek, F. (2005). Modeling subgrid-scale effects on particles by approximate deconvolution. *Phys. Fluids*, **17**, 081701–081701–4.

Shotorban, B. and Mashayek, F. (2006). A stochastic model for particle motion in large-eddy simulation. *J. Turbulence*, **7**(18), 1–13.

Shotorban, B., Zhang, K., and Mashayek, F. (2007). Improvement of particle concentration prediction in large-eddy simulation by defiltering. *Intl J. Heat Mass Trans.*, **50**, 3728–3739.

Silva, L., Damian, R., and Lage, P. (2008). Implementation and analysis of numerical solution of the population balance equation in CFD packages. *Computers Chem. Eng.*, **32**, 2933–2945.

Simonin, O., Deutsch, E., and Minier, J. (1993). Eulerian prediction of fluid/particle correlated motion in turbulent two-phase flows. *App. Sci. Res.*, **51**, 275–283.

Smagorinsky, J. (1963). General circulation experiments with the primitive equations: I. The basic experiment. *Mon. Wea. Rev.*, **91**, 99–164.

Stolz, S., Adams, N., and Kleiser, L. (2001). An approximate deconvolution model for large-eddy simulation with application to incompressible wall-bounded flows. *Phys. Fluids*, **13**, 997–1015.

Strutt, H., Tullis, S., and Lightstone, M. (2011). Numerical methods for particle-laden DNS of homogeneous isotropic turbulence. *Computers Fluids*, **40**, 210–220.

Tabor, G. and Baba-Ahmadi, M. (2010). Inlet conditions for large eddy simulation: A review. *Computers Fluids*, **39**, 553–567.

Tavoularis, S., Bennett, J., and Corrsin, S. (1978). Velocity-derivative skewness in small reynolds number, nearly isotropic turbulence. *J. Fluid Mech.*, **88**, 63–69.

Taylor, G. (1921). Diffusion by continuous movements. *Proc. London Math. Soc.*, **20**, 196–211.

Van Cittert, P. (1931). Zum Einflu der Spaltbreite auf die Intensitaetsverteilung in Spektrallinien. II. *Z. Phys*, **69**.

Vinkovic, I., Aguirre, C., and Simoens, S. (2006). Large-eddy simulation and Lagrangian stochastic modeling of passive scalar dispersion in a turbulent boundary layer. *J. Turbulence*, **7**(30), 1–14.

Wang, L. and Stock, D. (1993). Dispersion of heavy particles by turbulent motion. *J. Atmos. Sci.*, **50**(13), 1897–1913.

Wang, Q. and Squires, K. (1996). Large eddy simulation of particle-laden turbulent channel flow. *Phys. Fluids*, **8**, 1207–1223.

Wang, Y., Chatterjee, P., and Ris, J. (2011). Large eddy simulation of fire plumes. *Proc. Comb. Instit.*, **33**, 2473–2480.

Warhaft, Z. (1984). The interference of thermal fields from line sources in grid turbulence. *J. Fluid Mech.*, **144**, 363–387.

Weil, J., Sullivan, P., and Moeng, C. (2004). The use of large-eddy simulations in Lagrangian particle dispersion models. *J. Atmos. Sci.*, **61**, 2877–2887.

Wells, M. and Stock, D. (1983). The effects of crossing trajectories on the dispersion of particles in a turbulent flow. *J. Fluid Mech.*, **136**, 31–62.

Yeh, F. and Lei, U. (1991a). On the motion of small particles in a homogeneous isotropic turbulent flow. *Phys. Fluids A*, **3**, 2571–2586.

Yeh, F. and Lei, U. (1991b). On the motion of small particles in a homogeneous turbulent shear flow. *Phys. Fluids A*, **3**, 2758–2776.

Yeung, P. and Pope, S. (1988). An algorithm for tracking fluid particles in numerical simulations of homogeneous turbulence. *J. Comp. Phys.*, **79**, 373–416.